Strategies for Hybrid Integration and Packaging at Millimeter-Wave and THz Frequencies

Dong, Yunfeng

Publication date:
2019

Document Version
Publisher's PDF, also known as Version of record

Technical University of Denmark

Yunfeng Dong

Strategies for Hybrid Integration and Packaging at Millimeter-Wave and THz Frequencies

PhD Thesis, May 2018

DTU Electrical Engineering
Department of Electrical Engineering

YUNFENG DONG

Strategies for Hybrid Integration and Packaging at Millimeter-Wave and THz Frequencies

PhD Thesis, May 2018

Supervisors:

Tom Keinicke Johansen, Associate Professor at the Electromagnetic Systems Group, DTU Electrical Engineering.

Vitaliy Zhurbenko, Associate Professor at the Electromagnetic Systems Group, DTU Electrical Engineering.

DTU - Technical University of Denmark, Kgs. Lyngby - 2018

Strategies for Hybrid Integration and Packaging at Millimeter-Wave and THz Frequencies

This thesis was prepared by:
Yunfeng Dong

Supervisors:
Tom Keinicke Johansen, Associate Professor at the Electromagnetic Systems Group, DTU Electrical Engineering.
Vitaliy Zhurbenko, Associate Professor at the Electromagnetic Systems Group, DTU Electrical Engineering.

Electromagnetic Systems Group (EMS)
Department of Electrical Engineering (DTU Elektro)
Technical University of Denmark
Ørsteds Plads, Building 348
2800 Kgs. Lyngby
Denmark
Email: elektro@elektro.dtu.dk

Project period:	Dec 2014- May 2018
Education:	PhD
Field:	Electrical Engineering
Class:	Public
Remarks:	This thesis is submitted as partial fulfillment of the requirements for the PhD degree at the Technical University of Denmark.

for
mom & dad

Table of Contents

List of Publications

1. **Y. Dong**, A. F. Olvera, A. Morales, M. M. Aller, S. Preu, V. Zhurbenko, P. J. Hanberg, C. Okonkwo, I. T. Monroy, and T. K. Johansen. System integration and packaging of a terahertz photodetector at W-band. Submitted to *IEEE Transactions on Components, Packaging and Manufacturing Technology*.

2. M. Mbeutcha, T. K. Johansen, **Y. Dong**, B. Cimoli, and V. Krozer. Replicability of a millimeter-wave microstrip bandpass filter using parallel coupled lines. In *2018 IEEE MTT-S Latin America Microwave Conference (LAMC)*, pages 1–3, Dec 2018.

3. **Y. Dong**, V. Zhurbenko, P. J. Hanberg, and T. K. Johansen. A D-band rectangular waveguide-to-coplanar waveguide transition using wire bonding probe. *Journal of Infrared, Millimeter, and Terahertz Waves*, pages 1–17, Nov 2018.

4. **Y. Dong**, T. K. Johansen, V. Zhurbenko, and P. J. Hanberg. A rectangular waveguide-to-coplanar waveguide transition at D-band using wideband patch antenna. In *2018 48th European Microwave Conference (EuMC)*, pages 1–4, Sept 2018.

5. **Y. Dong**, T. K. Johansen, and V. Zhurbenko. Ultra-wideband coplanar waveguide to asymmetric coplanar stripline transition from DC to 165 GHz. *International Journal of Microwave and Wireless Technologies*, 10(8):870–876, June 2018.

6. A. Annoni, V. Nocella, A. Dentin, **Y. Dong**, and T. K. Johansen. RF 3D assembly for high density photonic circuits. In *2018 20th Italian National Conference on Photonic Technologies (FOTONICA)*, pages 1–3, Mar 2018.

7. **Y. Dong**, T. K. Johansen, V. Zhurbenko, and P. J. Hanberg. Coplanar transitions based on aluminum nitride interposer substrate for terabit transceivers. In *2017 47th European Microwave Conference (EuMC)*, pages 620–623, Oct 2017.

8. **Y. Dong**, T. K. Johansen, and V. Zhurbenko. On-chip patch antenna on InP substrate for short-range wireless communication at 140 GHz. In *2017 SBMO/IEEE MTT-S International Microwave and Optoelectronics Conference (IMOC)*, pages 1–5, Aug 2017.

9. **Y. Dong**, T. K. Johansen, V. Zhurbenko, and P. J. Hanberg. Rectangular waveguide-to-coplanar waveguide transitions at U-band using E-plane probe and wire bonding. In *2016 46th European Microwave Conference (EuMC)*, pages 5–8, Oct 2016.

10. **Y. Dong**, T. K. Johansen, V. Zhurbenko, A. Beretta, A. Vannucci, and G. Locatelli. A 3D hybrid integration methodology for terabit transceivers. In *2015 SBMO/IEEE MTT-S International Microwave and Optoelectronics Conference (IMOC)*, pages 1–5, Nov 2015.

11. V. Zhurbenko and **Y. Dong**. Improved field homogeneity for transmission line MRI coils using series capacitors. In *2015 SBMO/IEEE MTT-S International Microwave and Optoelectronics Conference (IMOC)*, pages 1–5, Nov 2015.

12. **Y. Dong**, T. K. Johansen, V. Zhurbenko, and Ö. Acar. Design procedure for compact folded waveguide filters. In *2015 1st URSI Atlantic Radio Science Conference (URSI AT-RASC)*, pages 1–1, May 2015.

13. V. Zhurbenko, Ö. Acar, and **Y. Dong**. Varactor-tuned substrate integrated evanescent filter. In *2015 1st URSI Atlantic Radio Science Conference (URSI AT-RASC)*, pages 1–1, May 2015.

Abstract

In this thesis, the strategies for hybrid integration and packaging at millimeter-wave and terahertz (THz) frequencies are investigated for different applications. The three-dimensional (3D) hybrid integration scheme of a terabit transmitter is introduced. For packaging microwave integrated circuits (MICs) as well as monolithic microwave integrated circuits (MMICs) at millimeter-wave and THz frequencies, rectangular waveguide-to-coplanar waveguide (CPW) transitions are realized by using E-plane probe, wire bonding probe, and wideband patch antenna. The system integration and packaging of a THz photodetector is addressed.

As the fundamental research work, planar transmission lines involved in the 3D hybrid integration of the terabit transmitter including CPW, coupled coplanar waveguide (CCPW), coplanar stripline (CPS), and coupled line based on aluminum nitride (AlN) substrate are introduced individually. The transmission line structures, properties, and simulation methods are explained while parasitic effects are also discussed. CPW-to-CPS and CCPW-to-coupled line transitions are developed for guiding single-ended signals and differential signal pairs, respectively. Besides, for suppressing parasitic modes, the coplanar transitions use either wire bonding bridges together with an absorber layer or hollow plated vias going through the AlN substrate. The designed planar transmission lines as well as coplanar transitions are optimized for supporting data transmissions starting from direct current (DC) and at the same time providing large bandwidths. By combining different planar transmission lines as well as coplanar transitions, the interposer for guiding four single-ended signals from the drivers (DRVs) to the Mach-Zehnder modulator (MZM) is formed and the integration scheme of the terabit transmitter is demonstrated.

Though rectangular waveguides are widely used as the standard interface for connecting or cascading different components and systems at millimeter-wave and THz frequencies, the MICs and MMICs at such high frequencies still rely on planar transmission lines. Thus, different methods and structures are invented for realizing the transitions between rectangular waveguides and planar transmission lines in particular rectangular waveguide-to-CPW transitions. The development of the packaging strategies is mainly based on the technical innovations of both transition methods and packaging architectures. One of the difficulties for designing rectangular waveguide-to-CPW transitions is to provide a wideband matching with a low insertion loss. In addition, the compatibility for packaging the components and chips as well as the fabrication possibility should also be taken

into account. As novel methods, the transitions based on quartz substrate using wire bonding probe and wideband patch antenna are proposed. They are compared with the transitions using E-plane probe. The 3D printing and copper plating processes are evaluated for fabricating the packaging structures at millimeter-wave and THz frequencies.

A THz photodetector is implemented by integrating a photoconductor with a feeding network, a bias-tee, and a rectangular waveguide-to-CPW transition. As an electro-optic device used for converting signals from optical domain to electrical domain, the photodetector can be applied on both the transmitter and the receiver sides in THz communication systems. The principal components are designed individually while the chip-level connections and the packaging structures are also described. The assembly structure is demonstrated and the packaging strategy is addressed.

Preface

This thesis is the final outcome of the PhD project titled "Strategies for Hybrid Integration and Packaging at Millimeter-Wave and THz Frequencies". It is submitted to fulfill the requirements for achieving the PhD degree at the Technical University of Denmark (DTU). The project was financially supported by DTU and it was carried out at the Electromagnetic Systems Group (EMS) from December 2014 to May 2018. The project was guided by Assoc. Prof. Tom K. Johansen as the principal supervisor and Assoc. Prof. Vitaliy Zhurbenko as the co-supervisor. From October 2017 to November 2017, the external research stay was accomplished at the Terahertz Systems Technology Group, Technische Universität (TU) Darmstadt, Darmstadt, Germany.

Yunfeng Dong, May 2018
Kgs. Lyngby, Denmark

Acknowledgments

First and foremost, I would like to express my greatest gratitude to my supervisors, Assoc. Prof. Tom K. Johansen and Assoc. Prof. Vitaliy Zhurbenko who supported me constantly throughout the PhD project. Back to the time I was a Master student at the Electromagnetic Systems Group (EMS), Technical University of Denmark (DTU), they were my teachers for the course "Microwave Engineering" and "RF Communication Circuits", respectively. That is how we met each other and they became my supervisors afterwards for the Master's thesis. During the past years towards my PhD degree, they were always there providing guidances, sharing ideas, explaining questions, and giving suggestions. After knowing each other for many years, they are not only my supervisors during research works but also friends for life. I really appreciate their respect, patience, kindness, understanding, encouragement, and accompany during the hard times. Besides, I would like to thank Dr. Peter Jesper Hanberg at DTU Danchip (National Center for Micro- and Nanofabrication in Denmark) for his assistance, suggestions, and research works in the clean room. Special acknowledgment is given to Assoc. Prof. Sascha Preu at the Terahertz Systems Technology Group, Technische Universität Darmstadt, for hosting the external research stay for me.

I would also like to thank all my colleagues as well as friends, in particular to Angel Blanco Granja, Bruno Cimoli, Guofang Wang, Jing Ren, Juan Sebastián Rodríguez Páez, Mario Méndez Aller, Michael Forum Palvig, Michele Squartecchia, Nikolaj Peter Brunvoll Kammersgaard, Oleksandr Rybalko, Öncel Acar, Paula Irine Popa, Piotr Marek Kamiński, Rasmus Schandorph Michaelsen, Virginio Midili, Wenzhao Li, Xiaoyang Zhang, Yiyao Wang, for the time we spent, the funny and serious discussions we had, the extraordinary and ridiculous things we did, the happiness and sorrows we shared.

Finally, I need to thank my family, especially my mom and dad who are proud of me and love me the most. They brought me up and taught me right from wrong. During the time my mom was sick, though she was suffering both physically and mentally, she was trying to cheer me up, calm me down, and express her strong and optimism for life.

CHAPTER 1

Introduction

With the ever increasing demand worldwide for high-speed communication, remote sensing, biomedical science, instrumentation systems, defense and security applications, the bit-rates for data transmission are accelerating and the next migration to 1 Tbit/s should take place in the near future. Under this circumstance, microwave integrated circuits (MICs) as well as monolithic microwave integrated circuits (MMICs) are designed to operate at higher and higher frequencies which reach the frequency range of millimeter-wave and terahertz (THz) frequencies. According to [1], THz frequencies refer to the frequency range between 100 GHz and 10 THz in which the wavelength varies from 3 mm to 30 μm. At such high frequencies, due to highly integrated and complex structures on the circuits, some minor or negligible effects and problems at lower frequencies become significant at system-on-package (SOP) level and they are challenging the existing technologies and strategies for system integration and packaging. Since the components containing both electrical and optical circuits are called electro-optic devices, the corresponding process is defined as hybrid integration and packaging. The objective of this research work is to develop innovative strategies that are suitable for hybrid integration and packaging at millimeter-wave and THz frequencies. The developments include hybrid integration for broadband data transmissions, approaches for packaging MICs and MMICs into systems, and wideband antennas. The future high-speed data transmission systems operating at millimeter-wave and THz frequencies will benefit from the developed innovative strategies for hybrid integration and packaging.

1.1 Current Trends and Challenges

Fig. 1.1 shows the envisaged three-dimensional (3D) hybrid integration scheme of a terabit transmitter which is supposed to be used at datacenter gateways of the optical Ethernet. By combining electric and optic circuits, utilizing higher-order quadrature amplitude modulation (QAM), and applying 64 Gbaud operation rate, the transmitter can handle terabit throughput. The electrical signals coming out of the drivers (DRVs) are coupled with the optical signals in the Mach-Zehnder modulator (MZM). The interposer as well as the chip-level connections among the DRVs, interposer, and MZM are being challenged since the electrical signals require a large bandwidth ranging from direct current (DC). Under this circumstance, for hybrid integration at millimeter-wave and

THz frequencies, it becomes critical to design planar transmission lines, coplanar transitions, and chip-level connections supporting large bandwidths.

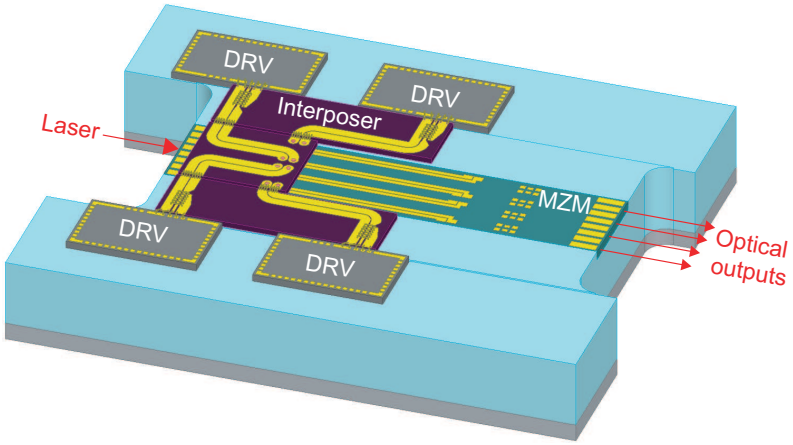

Figure 1.1: 3D hybrid integration scheme of a terabit transmitter.

Though planar transmission lines such as microstrip lines (MSLs) [2]–[8], coplanar striplines (CPSs) [9]–[16], and coplanar waveguides (CPWs) [17]–[30] are widely used for designing MICs and MMICs at millimeter-wave and THz frequencies, they are normally specialized within their operating frequency bands. Since the dimensions of the transmission lines are related to the operating frequencies, it becomes difficult to overcome the variations of characteristic impedance and provide a good matching in a wide frequency range. However, as the fundamental research work, the planar transmission lines used for designing the interposer between the DRVs and the MZM have to provide a large bandwidth which can support data transmissions starting from DC. MSLs have a simple geometry where the signal trace is featured on a thin, conductor-backed dielectric substrate. A quasi-TEM mode is supported and the electric fields mainly exist between the signal trace and the bottom ground plane. For specific substrate properties, the characteristic impedance of a MSL is determined by the width of the signal trace which means the transmission line cannot be tapered otherwise it will lead to an impedance mismatch and thus a small bandwidth. CPSs and CPWs are in configurations of ground-signal (GS) and ground-signal-ground (GSG), respective, where the electric fields exist in the gaps between the signal and ground traces. Compared with MSLs, CPSs and CPWs have lower dispersions and at the same time their characteristic impedances are less sensitive to the substrate properties which makes it possible to adjust the dimensions of the transmission lines without affecting the characteristic impedance [31]. This special property also makes CPSs and CPWs versatile for designing circuits based on different substrates and integrating them into a system. Besides, there are many derived structures based on CPWs. For example, when two ground traces locate on another layer different from the signal trace, it forms the so-called elevated coplanar waveguide (ECPW) or when a ground plane is added on the backside of the substrate it becomes a conductor-backed coplanar waveguide (CB-CPW) where the electric fields exist not only in the gaps but also between the signal trace and the bottom ground plane.

In addition, for hybrid integrations, the circuits for realizing different features are normally based on different substrates and driving schemes. For example, as is shown in Fig. 1.1, the driving

schemes for the DRV and MZM are GSG and GS, respectively. As a result, coplanar transitions [32]–[36] as well as chip-level connections [37]–[44] between different planar transmission lines or circuits become critical since their bandwidths normally determine the performance of the whole system especially at millimeter-wave and THz frequencies. For designing wideband transitions and connections, not only the characteristic impedances but also the propagation modes need to be matched [45]. At the same time, for the designed coplanar transitions and chip-level connections, the parasitic effects must be suppressed and the radiations need to be kept as low as possible in order to support wideband and low-loss transmissions. Besides, by applying 3D hybrid integrations, the circuits can be integrated both horizontally and vertically [46]. In this case, the occupation area is further reduced while it requires more advanced technologies and results in more complex structures. It also becomes harder to predict and restrict parasitic modes in the integrated structures.

Apart from planar transmission lines, rectangular waveguides have been continuously used for a wide range of applications guiding electromagnetic waves. This is due to its low-loss property, high power-handling capability, and simple structure. Besides, rectangular waveguides have a fixed cross-section within each frequency band. As a result, it has become the standard interface for connecting or cascading different components and systems especially at high frequencies. Since MICs and MMICs at millimeter-wave and THz frequencies mainly rely on planar structures, for system integration and packaging, the transitions between rectangular waveguides and planar transmission lines are under intensive study, in particular rectangular waveguide-to-CPW transitions.

Fig. 1.2 illustrates the packaging structures of an indium phosphide (InP) double heterojunction bipolar transistor (DHBT) amplifier at 300 GHz [47] and an InP high electron mobility transistor (HEMT) amplifier at 480 GHz [18]. By using either E-plane probe or dipole probe transitions, the electromagnetic waves are guided from the rectangular waveguide to the MMIC. The challenging requirements for such transitions are wideband matching with low insertion loss and at the same time versatile for packaging the existing components and chips.

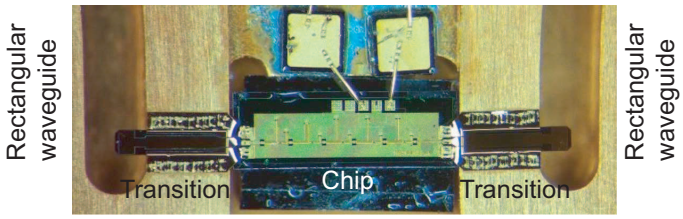

(a) E-plane probe used for packaging an InP DHBT amplifier at 300 GHz.

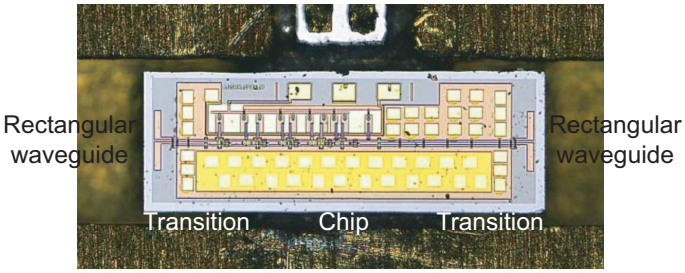

(b) Dipole probe used for packaging an InP HEMT amplifier at 480 GHz.

Figure 1.2: Packaging structures of MMICs at millimeter-wave and THz frequencies.

Different methods and structures can be found in the literature for realizing transitions between rectangular waveguides and planar transmission lines. By tapering the height and width of the rectangular waveguide in several stages, the characteristic impedance is matched to the planar transmission line step by step [48], [49]. With micromachining technologies, a short-circuited probe can be fabricated connecting the conductor wall of the tapered rectangular waveguide to the planar transmission line [50]. Besides, by inserting an wideband antenna at the end of the rectangular waveguide in the direction of maximum radiation, the electromagnetic waves can be guided from the rectangular waveguide to the feeding network and then the following circuits [18], [51]–[53]. The antenna is patterned on the substrate and normally determines the bandwidth of the transition. The challenge for designing wideband antennas is to achieve a high gain and at the same time a large bandwidth within a limited occupation area on the chip. In some cases, for increasing the gain of the antenna, stacked dielectric resonators and hemispherical silicon lens are placed on the top which help to generate rectangular waveguide modes and focus electromagnetic waves in the direction of maximum radiation [54], [55]. Though antenna arrays with feeding networks can also be used, it normally occupies a large footprint on the chip which might become unaffordable for compact designs [56], [57]. Besides, the designed wideband antenna or feeding network should be compatible for being connected to the planar transmission lines on the chip, otherwise coplanar transitions have to be implemented between the circuit and the antenna which also introduce extra discontinuities and losses.

Compared with other methods and structures, E-plane probe exhibits noticeable performance for rectangular waveguide-to-CPW and -MSL transitions especially at millimeter-wave and THz frequencies [47], [58]–[68]. The probe is inserted into a rectangular waveguide through an aperture cut in the center of the broadwall parallel to the longitudinal axis. Its location is about a quarter wavelength away from the end of the rectangular waveguide forming an impedance transformer converting the termination from short to open. Since the inserted probe is in parallel with the electric fields inside the rectangular waveguide, it is called E-plane probe transition. E-plane probe can have different shapes and a large bandwidth can be achieved within the whole waveguide frequency band when it is designed carefully.

At millimeter-wave and THz frequencies, not only circuits but also packaging structures become small in size. For example, the width and height of a standard WR-6.5 rectangular waveguide at D-band ranging from 110 GHz to 170 GHz are 1651 μm and 825.5 μm, respectively. Unnoticeable gaps or misalignments in the packaging structures due to fabrication tolerances may result in unexpected losses, parasitic modes, or frequency shifts. With the development of accurate fabrications, in addition to milling, other technologies such as low-temperature co-fired ceramic (LTCC), laser beam machining (LBM), 3D printing, PolyStrata, metal deposition and sputtering are also used for fabrication processes [69]–[72].

1.2 Thesis Outline

The main part of the thesis is divided into five chapters.

In Chapter 1, the background, motivation, and purpose of this thesis work are introduced.

In Chapter 2, the 3D hybrid integration and packaging of a terabit transmitter are presented. The designs of planar transmission lines as well as coplanar transitions are shown at the beginning which are used for guiding single-ended signals. Either wire bonding bridges together with an absorber layer or hollow plated vias going through the substrate are used for suppressing parasitic modes and enlarging the bandwidth. The full-wave electromagnetic (EM) simulations of the proposed transmission lines and coplanar transitions are based on ANSYS Electronics Desktop which is previously known as High Frequency Structural Simulator (HFSS). The transition prototypes are fabricated and measured in a back-to-back configuration. The measurement results are compared with the simulation results. After that the interposer is designed by combining the proposed planar transmission lines and coplanar transitions. The assembly of the terabit transmitter is demonstrated at the end and the co-simulation of the integrated system is carried out by using Advanced Design System (ADS) from KEYSIGHT.

In Chapter 3, the designs of rectangular waveguide-to-CPW transitions based on different structures are described. Being widely used structure for transitions between rectangular waveguides and planar transmission lines, E-plane probes are designed at different frequency bands and work as references based on the existing technology. As a novel structure for realizing transitions between rectangular waveguides and planar transmission lines, wire bonding probes are illustrated. The fabrication and measurement results of the proposed transitions at different frequency bands are shown and compared with the simulation results. Besides, the transition using wideband patch antenna are demonstrated while the proposed patch antenna can also be used for wireless chip-to-chip communications. The performances among transitions based on different structures are discussed at the end.

In Chapter 4, the system integration and packaging of a THz photodetector at W-band ranging from 75 GHz to 110 GHz are addressed. As the principle components involved in the system integration, the feeding network, bias-tee, and rectangular waveguide-to-CPW transition using E-plane probe are designed individually. The assembly structure of the fully-packaged photodetector is demonstrated including the designed components, accessories, and packaging structures. The measurement results validate the proposed strategy for system integration and packaging.

In Chapter 5, the conclusions of thesis work are drawn.

CHAPTER 2

Hybrid Integration and Packaging of PANTHER Terabit Transmitter

With the ever increasing demand worldwide for high-speed communication, the blooming data traffic and comprehensive multimedia services dramatically increase the workload of the existing data transmission systems. The currently used edge switches and datacenter gateways based on 100 Gbit/s dual-polarization quadrature phase-shift keying (DP-QPSK) are being challenged and approaching their design limits. As an alternative, the optical Ethernet has been considered to be an ideal candidate for the next-generation high-speed data transmission system. Besides, the migration from 100 Gbit/s to 400 Gbit/s and further on to 1 Tbit/s optical line card products based on higher-order quadrature amplitude modulation (QAM) should take place in the near future [73]. PANTHER is an European project whose name comes from the abbreviation of "PAssive and electro-optic (EO) polymer photonics and indium phosphide (InP) electronics iNtegration for multi-flow Terabit transceivers at edge software-defined networking (SDN) switcHes and datacentER gateways". By combining photonic and electronic components and coming up with novel 3D hybrid integration schemes for high-speed modulation and optical functionality on-chip, the project aims to develop transceivers that have the ability to handle terabit throughput. By using dual-polarization (DP) 64-QAM and 64 Gbaud operation rate, the overall capacity of the PANTHER transceivers can go up to 1.536 Tbit/s.

Fig. 2.1 shows the envisaged PANTHER terabit transmitter based on three-dimensional (3D) hybrid integration scheme. For system integration, the drivers (DRVs) based on InP double heterojunction bipolar transistor (InP-DHBT) technology work as digital-to-analog converters which support both single-ended signal and differential signal pair. The signals coming out of the DRVs are connected to the interposer by using wire bonding connections. The interposer is based on an aluminum nitride (AlN) substrate where the signals are guided from the DRVs to the Mach-Zehnder modulator (MZM). Vias going through the substrate act as the vertical connections between the interposer and the MZM. The MZM is based on InP substrate and the electrical signals are coupled to optical signals. In addition, an aluminum carrier is implemented under the DRVs and MZM as the heat sink layer since each DRV generates approximately 3 watt of heat. As a part of the preliminary research, a methodology of 3D hybrid integration scheme for PANTHER terabit

transceiver was reported by the author in [46]. Substrate materials such as silicon dioxide (quartz, SiO_2), aluminum oxide (alumina, Al_2O_3), and AlN have proven their possibility for designing wideband planar transmission lines due to their low dissipation factor (tanδ). By taking into account the bandwidth of the via connections, fabrication and integration feasibility, a thin AlN substrate is finally selected to be used for the interposer design.

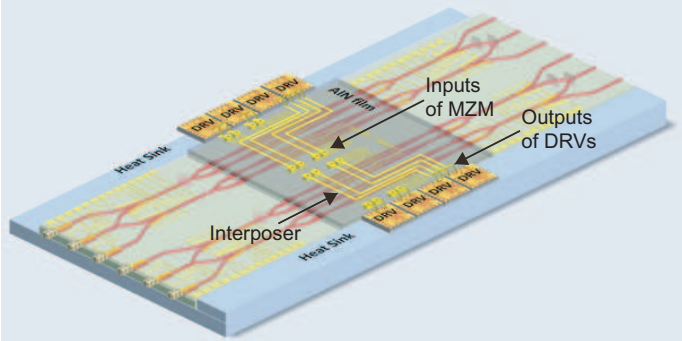

Figure 2.1: The envisaged PANTHER terabit transmitter based on 3D hybrid integration scheme of photonic and electronic components (from [74]).

Transitions are necessary when different types of transmission lines need to be connected. The bandwidth is one of the key requirements that needs to be taken in to account when designing a transition. When the transition works around a carrier frequency, the bandwidth normally refers to the width of the passband located symmetrically on both sides of the carrier frequency which is similar to a band-pass filter. In this case, the transition in principle can be realized by coupling electromagnetic waves from one part to another and a physical connection is not necessary. However, for transitions supporting data transmissions starting from direct current (DC), the signal trace must be connected physically which has a similar performance as a low-pass filter with a high cutoff frequency. Besides, the structure of the transition is also determined by the layer stacks, integration methods, and fabrication technologies. Since planar transmission lines such as coplanar waveguide (CPW) and coplanar stripline (CPS) are widely used for designing microwave integrated circuits (MICs) and monolithic microwave integrated circuits (MMICs), the transitions between them are under intensive study [12], [32]–[36], [75]–[77]. In [32], a coplanar transition between CPW and CPS based on silicon substrate is reported. The proposed CPW-to-CPS transition is used for feeding a multiband dipole antenna and wire bonding bridges are used to restrict parasitic modes. As a result, a bandwidth of 55 GHz is achieved. According to [76], by using reformed air-bridge the demonstrated CPW-to-CPS transition based on gallium arsenide (GaAs) substrate exhibits a bandwidth up to 110 GHz.

When the characteristic impedances of the planar transmission lines are matched, inserting a transition with a short distance in general does not cause serious impedance mismatch. However, one of the difficulties for designing such transitions is to achieve a wideband matching of the propagation modes. This is due to the fact that the propagation modes of the planar transmission lines could be quite different. Thus the electromagnetic waves have to be converted smoothly from one propagation mode to another at the transition in order to achieve a large bandwidth. For

CPW-to-CPS transitions, efforts are put to guide the electric fields being concentrated in one of the gaps between the signal and ground traces instead of radiating from the transition since one of the ground traces has to be terminated.

This chapter aims to investigate wideband CPW-to-CPS transitions supporting data transmissions starting from DC which can be used as a part of the interposer for PANTHER terabit transmitter. For this purpose, the basic structures and simulation methods of CPW as well as CPS based on AlN substrate are presented at the beginning of this chapter. In order to suppress parasitic modes, absorber layer between the substrate and the bottom ground plane, wire bonding bridges on top of the transmission lines, and vias going through the substrate are introduced and their performances are compared. After that, two CPW-to-CPS transitions are proposed using either wire bonding bridges together with absorber layer or hollow plated vias going through the substrate. Besides, the CPW-to-CPS transitions are designed in a back-to-back configuration with the purpose of easier measurement and they are suitable for guiding single-ended signals. Two transition prototypes based on different methods are fabricated and measured. The measurement results are compared with the simulation results and the performances of different prototypes are discussed. The planar transmission lines and coplanar transitions for differential signal pair are also included in Appendix A. At the end of this chapter, the system integration and packaging of a terabit transmitter is described where each component integrated in the system is introduced briefly and the interposer design as well as the chip-level connections are shown in detail. The designed interposer is simulated and the co-simulation of the system is carried out by including the measurement results of the MZM.

2.1 Planar Transmission Lines and Coplanar Transitions

2.1.1 Coplanar Waveguide

Since the outputs of the DRVs involved in the system integration have a configuration of ground-signal-ground (GSG), CPWs are designed as a part of the interposer and employed at the beginning of the paths. The conductors locate on the top of the substrate forming an uniplanar structure. The center signal trace is separated by two narrow gaps from the ground traces on both sides which structure simplifies the fabrication process and allows inexpensive characterization using on-wafer techniques. The electric waves exist mainly in the gaps between the signal and ground traces supporting quasi-TEM transmissions. Lossless TEM transmission lines are dispersionless which does not lead to any signal distortion while for quasi-TEM transmission lines, the effective dielectric constant (ϵ_{eff}) is affected by the operating frequency [78]. Thus the group velocity varies in terms of frequency and results in signal distortions. This is true even if the substrate material is non-dispersive whose dielectric constant (ϵ_r), in reality, also varies due to different operating frequencies. According to [31], compared with microstrip line (MSL), CPW has a lower frequency dispersion which makes it a perfect candidate for transmitting wideband signals. Thus CPW has been widely used in MICs and MMICs at millimeter-wave and terahertz (THz) frequencies. Besides, its characteristic impedance is independent from the substrate properties to some extent

and is mainly determined by the ratio of $W/(W + 2G)$, in which W and G represent the width of the signal trace and the width of the gaps, respectively. That is to say, the dimension of a CPW can be adjusted without affecting the characteristic impedance or it is also possible to keep the width of the signal trace constant when a CPW goes through different substrates. This specialty makes CPW a competitive and versatile planar transmission line used for system integration and packaging. Fig. 2.2 illustrates the basic structure of the designed CPW and the corresponding excitation scheme together with the port field in the simulations.

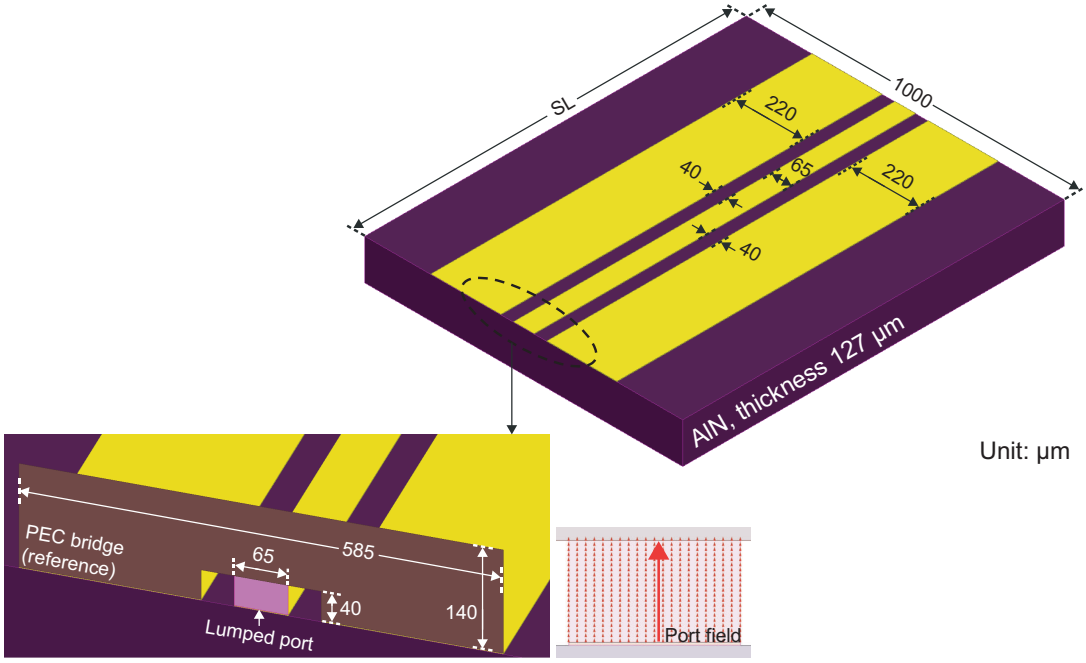

Figure 2.2: CPW based on AlN substrate and the port excitation scheme used for simulations.

As is shown in Fig. 2.2, the width of the signal trace is 65 μm and the width of the ground traces is 220 μm with a gap of 40 μm. The CPW is designed to have a characteristic impedance of 50 Ω and to support data transmissions from DC to 170 GHz which is based on an AlN substrate with a thickness of 127 μm (0.005"). The AlN substrate has a width of 1000 μm while SL represents the length of the substrate which can be adjusted for different simulations. Though the ground traces play a minor role in affecting the characteristic impedance of a CPW, it has to be wide enough in order to support the propagation mode since the electric waves mainly exist in the gaps. The material of the conductors is gold with an electrical conductivity of 4.257e7 S/m and the skin depth is calculated to be 0.18 μm at 170 GHz. In order to guarantee reasonable performances at low frequencies, the thickness of the conductor layer is designed to be 1.2 μm. The AlN substrate from Applied Thin-Film Product (ATP) is used for the designs whose ϵ_r and tanδ measured at 1 MHz are 8.6 and 0.001, respectively. In addition, the substrate consists of 98% AlN and 2% impurities.

In the simulation, lumped ports and vertical perfect electric conductor (PEC) bridges are used as the excitation scheme where the PEC bridge connects to the ground traces and it is selected to be the reference. The lumped port is assigned to the sheet between the signal trace and the PEC

bridge. The width and height of the lumped port are 65 μm and 40 μm, respectively. By default, perfect H boundary conditions are assigned to the edges of the lumped port which do not touch any conductor. As is shown in Fig. 2.2, the port field is uniform and parallel to the perfect H edges. Due to the requirement of the simulator, lumped ports must be placed inside the simulation space and with the purpose of preventing any reflection caused by the surroundings, an air cavity with radiation boundary conditions is added around the substrate. Besides, according to [79] and [80], when the lumped port is treated as a straight rectangular conductor with a thickness (t) of zero, the parasitic sheet inductance (L_p) can be estimated by

$$L_p|_{t=0}\,[pH] = 200 \cdot h \cdot \{ln(2 \cdot u) + \frac{0.2235}{u} + 0.5\} = 8.6\,[pH] \tag{2.1}$$

or

$$\begin{aligned} L_p|_{t=0}\,[pH] = 200 \cdot h \cdot \{&ln(u + \sqrt{u^2+1}) + \\ &u \cdot ln(\frac{1}{u} + \sqrt{(\frac{1}{u})^2+1}) + \frac{1}{3} \cdot (u^2 + \frac{1}{u} - \frac{(u^2+1)^{3/2}}{u})\} \\ = 9.2\,[pH] \end{aligned} \tag{2.2}$$

where $u = h/w$, h and w in millimeter represent the height and width of the lumped port, respectively. The parasitic sheet inductance is subtracted from the simulation results afterwards by post processing and the calibrated S-parameters are provided by the simulator. Eq. 2.1 is used by HFSS while it is replaced by Eq. 2.2 in ANSYS. The difference between the calculated parasitic sheet inductances is negligible since it is less than 1 pH for the lumped port shown Fig. 2.2. For simulations requiring higher accuracy, the parasitic inductance introduced by the PEC bridge may also be taken into account and calibrated out using the technique described in [81]. In addition, the excitation scheme using lumped ports with vertical PEC bridges is also more similar to on-wafer measurements where the probes touch the conductors from the top. Fig. 2.3 shows the simulated S-parameters as well as the characteristic impedance (Z_0) of the designed CPW based on AlN substrate with different lengths. The blue solid lines are the simulation results when the length is 1.2 mm while the red solid lines represents the simulation results for 5 mm. In both cases, the CPW exhibits a bandwidth of 170 GHz, in which the return loss is better than 10 dB and the insertion loss is less than 1.3 dB. As expected, the simulated characteristic impedance of the CPW has a low frequency dispersion which varies around 6 Ω from DC to 170 GHz. Though a higher insertion loss is achieved by the CPW with a length of 5 mm, no visible notch or resonance can be observed so that the radiations from the CPW as well as the parasitic modes are negligible.

A more common and realistic situation is shown in Fig. 2.4 where there is a bottom ground plane under the substrate forming the so-called conductor-backed coplanar waveguide (CB-CPW). Since the AlN substrate is thin, the electric waves exists not only in the gaps between the signal and ground traces but also between the signal trace and the bottom ground plane which might lead to a propagation of mixed modes.

Fig. 2.5 shows several possible propagating modes that can exist on a CB-CPW structure while they might come up individually or mix with each other in the real case. The CPW mode as the fundamental and dominant mode on a CB-CPW is slightly different from how it distributes on

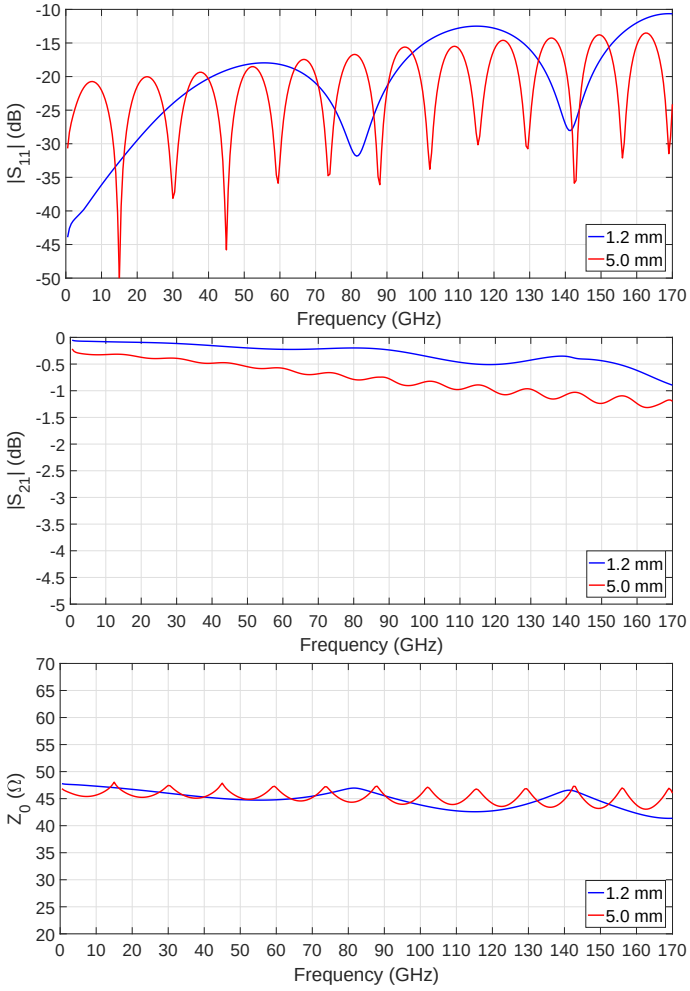

Figure 2.3: Simulation results of the CPW based on AlN substrate with different SL values.

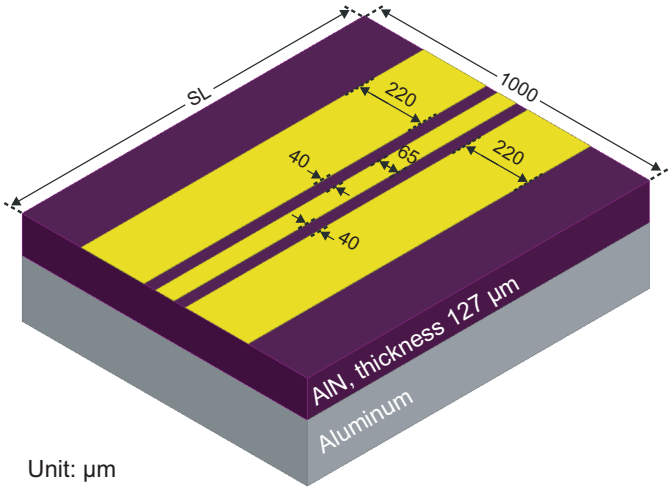

Figure 2.4: CB-CPW based on AlN substrate.

a conventional CPW due to the bottom ground plane. Especially for CB-CPWs based on thin substrates, a strong electric field exists between the signal trace and the bottom ground plane. When the electric field is distributed homogeneously between the top conductors and the bottom ground plane along the CB-CPW structure, the signal trace together with the ground traces might work as a wide MSL which leads to a microstrip-like mode. In this case, the characteristic impedance migrates from 50 Ω and it causes mismatch effects. Besides, for higher-order microstrip-like modes, the energy might be radiated into free space and result in high losses since the top conductors behave like patch antennas. If the substrate and bottom ground plane are much wider than the top conductors, the image-guide-like mode can also be supported by the structure in which situation the electric field is reflected back into free space by the bottom ground plane. As a result, when designing a CB-CPW, the structure is normally optimized for supporting solely CPW mode so that the mismatch and parasitic effects can be suppressed.

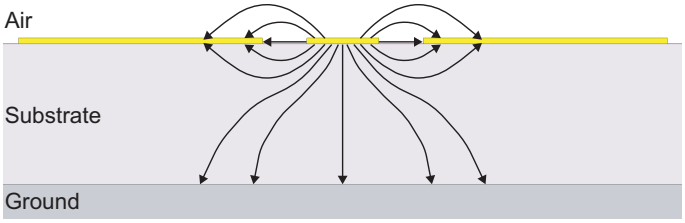

(a) CPW mode.

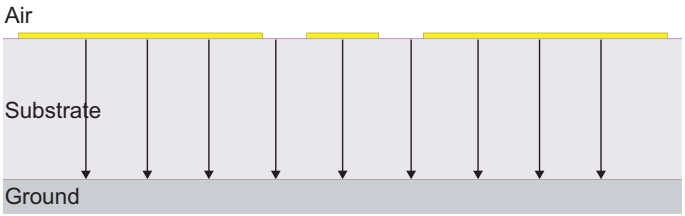

(b) Microstrip-like mode.

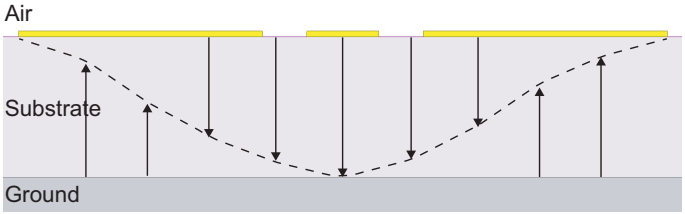

(c) First higher-order microstrip-like mode.

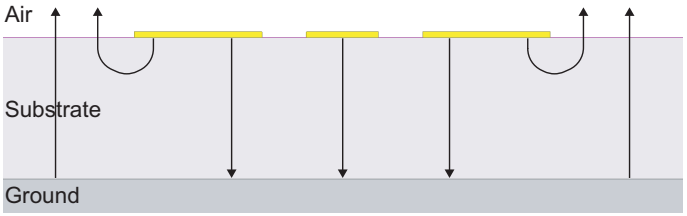

(d) Image-guide-like mode.

Figure 2.5: Propagating modes on a CB-CPW.

Fig. 2.6 shows the simulation results of the CB-CPW based on AlN substrate with different lengths. When the length is 1.2 mm, a bandwidth of 170 GHz is achieved, in which the insertion loss is less than 0.9 dB and the return loss is better than 14.5 dB. However, due to parasitic effects, the simulated S-parameters exhibit notches at 124 GHz, 147 GHz, and 170 GHz, respectively. By increasing the length to 5 mm, it is obvious that the notches appear at lower frequencies which limits the bandwidth and degrades the performance of the designed CB-CPW.

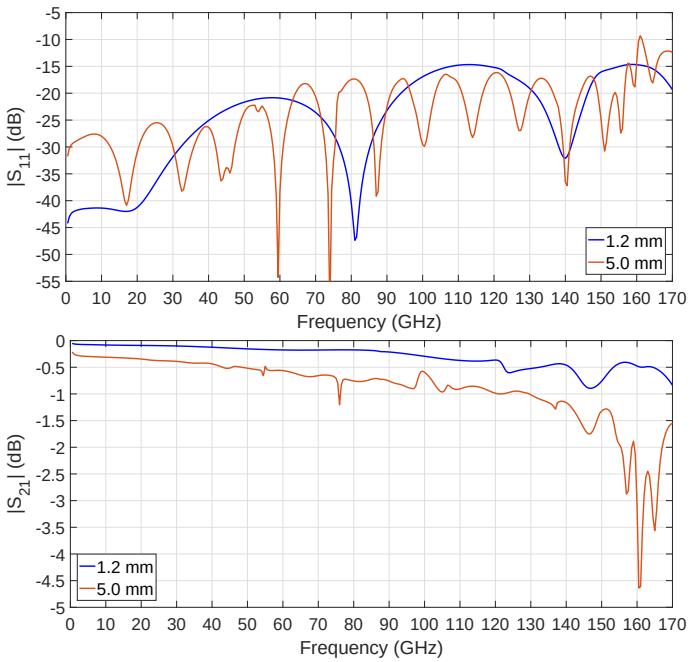

Figure 2.6: Simulation results of the CB-CPW based on AlN substrate with different SL values.

The electric field distributions of the conventional CPW as well as the CB-CPW with a length of 5 mm at different frequencies are compared in Fig. 2.7. According to the S-parameters shown in Fig. 2.6, the notches appear at 76 GHz and 161 GHz when the length is 5 mm. In addition, the electric field distributions at 70 GHz, 150 GHz, and 170 GHz are also presented as references. At 76 GHz, the designed CB-CPW exhibits a microstrip-like mode where the signal trace together with the ground traces act as a MSL while at 161 GHz, it generates a higher-order microstrip-like mode and cause a serious resonance. For the conventional CPW which does not have the bottom ground plane, the propagation mode is dominated by the CPW mode and no evident resonance can be observed at the corresponding frequencies.

Several methods can be used to restrict parasitic modes on CB-CPW structures and one of them is to reduce the electric field intensity between the CPW and the bottom ground plane. This can be realized by increasing the thickness of the substrate or adding an absorber layer underneath, thus the bottom ground plane is moved away from the CPW on the top. Fig. 2.8 shows the structure when an absorber layer is added. In the simulation, polyoxymethylene (POM) with a thickness of 3.5 mm is used as the absorber layer which can also be replaced by other materials such as aluminum oxide (alumina, Al_2O_3). The ϵ_r and tanδ of the POM absorber layer are 3.8 and 0.06, respectively. The blue dashed lines in Fig. 2.12 are the simulation results of the CPW with a POM

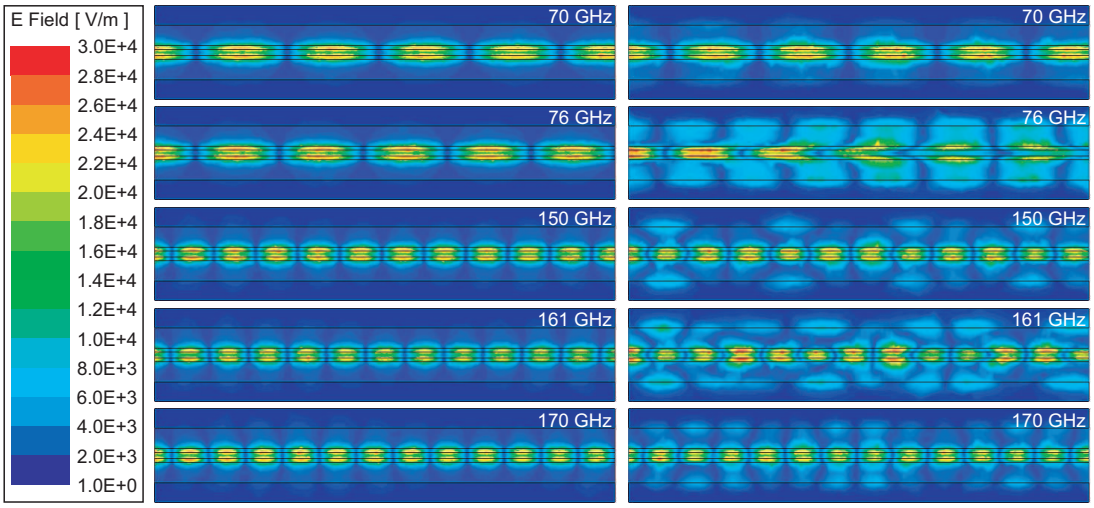

Figure 2.7: Electric field distributions of CPW (left column) and CB-CPW (right column) with a length of 5 mm at different frequencies.

absorber layer underneath. The return loss is better than 14 dB with an associated insertion loss of 1.5 dB up to 170 GHz. Since the parasitic modes are successfully restricted by the absorber layer, it shows a smooth transmission without visible notch.

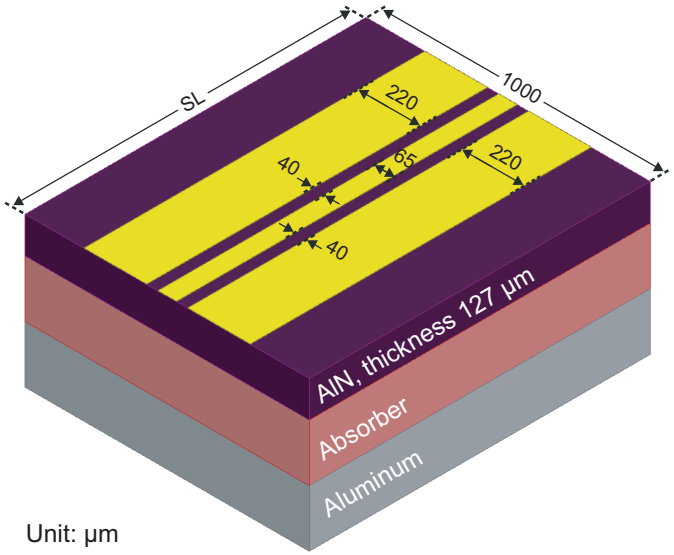

Figure 2.8: CPW with an absorber layer.

When thin substrates have to be used for designing the circuit and at the same time the bottom ground plane cannot be avoided, the extra structures shown in Fig. 2.9 such as wire bonding bridges or hollow plated vias can be used to restrict parasitic modes. By connecting the two ground traces of the CPW with wire bonding bridges, the ground traces are forced to have the same potential and the electric fields exist not only in the gaps but also between the signal trace and the wire bonding bridges. Since the distance from the signal trace to the bottom ground plane is small for

a thin substrate, the wire bonding bridges have to be low enough so that the electrical fields are more likely to be concentrated between the signal trace and the wire bonding bridges instead of the bottom ground plane. Otherwise, the effect in restricting the parasitic modes is limited. In this case, since the absorber layer under the thin substrate does not affect the wire bonding bridges on the top, it can be used as a supplementary method which further increases the distance from the signal trace to the bottom ground plane. As an alternative, hollow plated vias going through the thin substrate can also be used for restricting the parasitic modes. By connecting the ground traces on the top to the bottom ground plane, instead of floating, the ground traces are forced to have the same potential as the ground plane. Besides, the vias change the structure of the thin substrate and reduce the size of the continuous space. As is shown in Fig. 2.9, due to the fabrication process another conductor layer is normally added on the backside of the thin substrate and the electric fields exist in the cavity formed by the vias together with the conductors. In this way, the electric fields are restricted in a specific space in the thin substrate which prevents the potential of generating higher-order microstrip-like modes. Since the distance between the vias plays an important role in restricting the parasitic modes, the vias are placed as close to the gaps as possible and the ground traces in general are designed as narrow as possible.

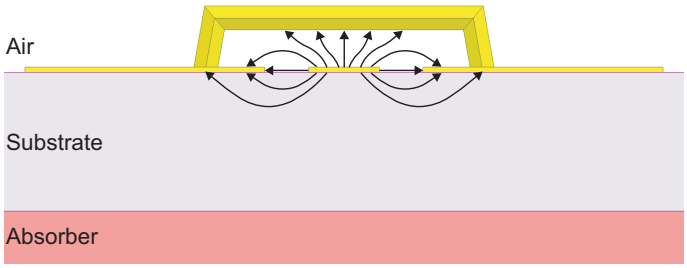

(a) CPW with an absorber layer and wire bonding bridges.

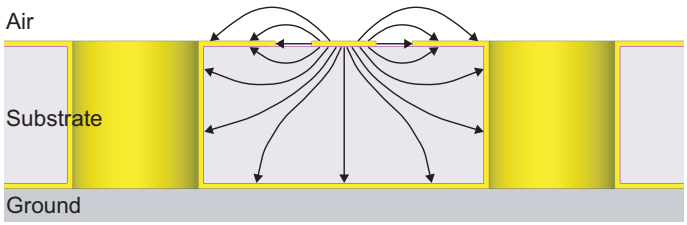

(b) CPW with hollow plated vias.

Figure 2.9: Electric field distributions of the CPW based on thin substrate with different structures.

As is shown in Fig. 2.10, wire bonding bridges are added on the top all the way along the CPW. The wire bonding bridges have a diameter of 25 μm and the material is gold. The height of the wire bonding bridges is 50 μm and they are located 100 μm away from each other, which is a compromise by taking into account performances and fabrication possibilities. The red dashed lines in Fig. 2.12 are the simulation results of the CPW with wire bonding bridges on the top. Compared with the simulation results in Fig. 2.6 when there is no wire bonding bridge and the length of the CPW is 5 mm, parasitic modes are restricted to some extend but not enough. Due to the thin AlN

substrate, adding wire bonding bridges on the top can only provide a limited improvement. As a result, the transmission performance starts degrading fast after 156 GHz and visible notches appear at 76.5 GHz, 97.5 GHz, 162 GHz, and 166.5 GHz, respectively.

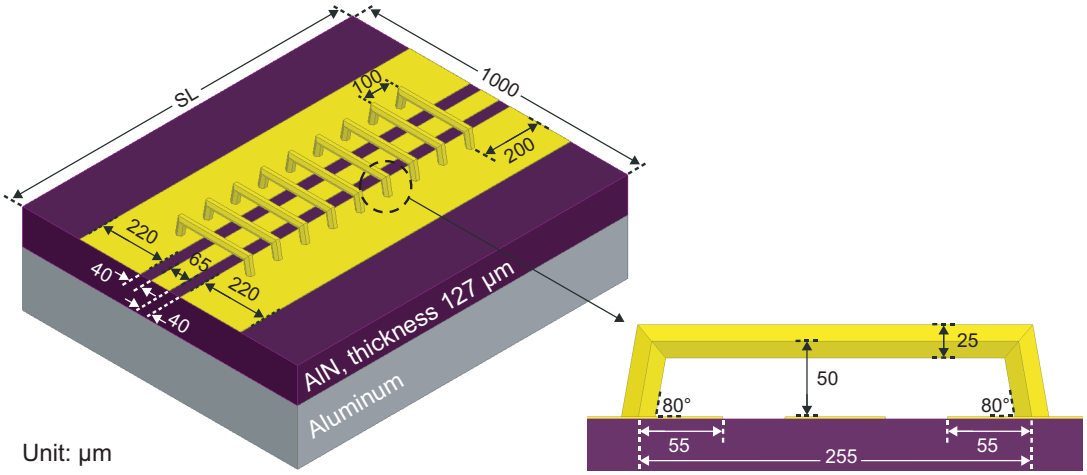

Figure 2.10: CPW with wire bonding bridges.

Fig. 2.11 shows the structure of the CPW when both the absorber layer and wire bonding bridges are implemented. The simulation results are represented by the green solid lines in Fig. 2.12. In comparison with the simulation results of the CPW using absorber layer solely (blue dashed lines), adding extra wire bonding bridges on the top achieves an improvement around 3 dB for the return loss while the insertion loss remains less than 1.55 dB up to 170 GHz.

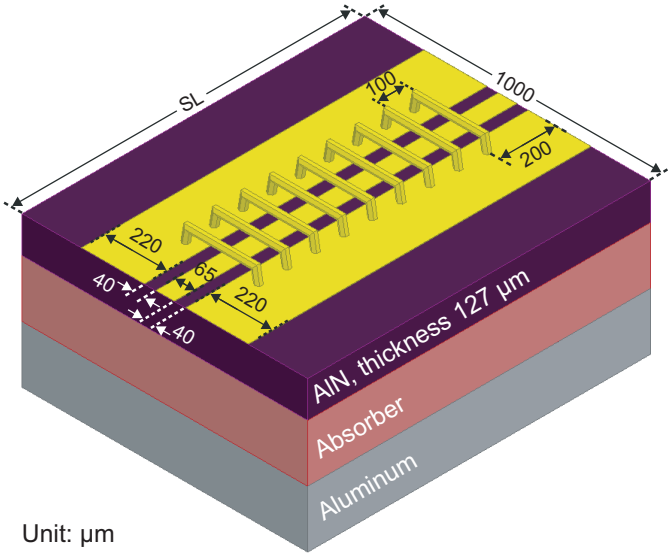

Figure 2.11: CPW with an absorber layer and wire bonding bridges.

Fig. 2.13 shows the electric field distributions at the resonant frequencies of the CPW with wire bonding bridges solely when the length is 5 mm in comparison with the CPW with both absorber layer and wire bonding bridges. Since the wire bonding bridges on the top cannot restrict the

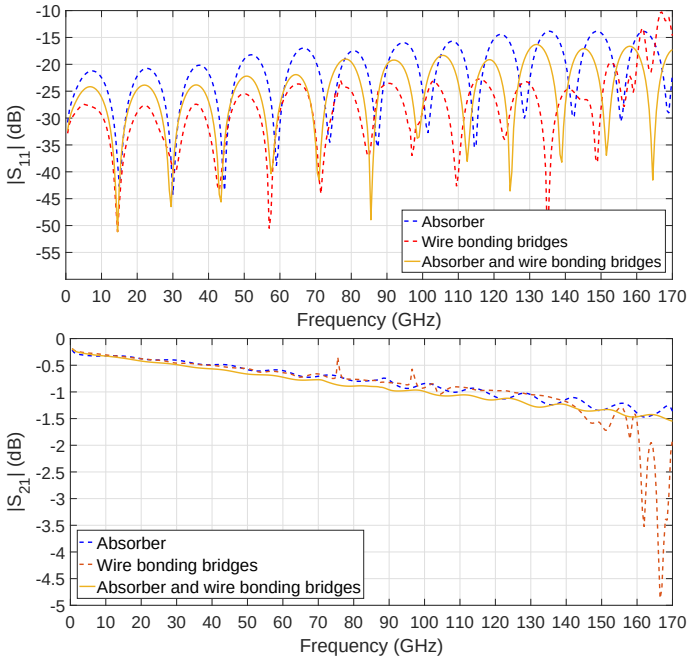

Figure 2.12: Simulation results of the CPW with a length of 5 mm based on different methods for suppressing parasitic modes.

parasitic modes completely, the CPW with wire bonding bridges exhibits weak microstrip-like modes at 76.5 GHz and 96.5 GHz while strong higher-order microstrip-like modes at 162 GHz and 166.5 GHz. These parasitic modes result in either discontinuities or losses on the S-parameters which leads to the degradation of transmission performance. When both absorber layer and wire bonding bridges are implemented, the CPW mode becomes the dominant propagation mode of the transmission line up to 170 GHz so that no resonance can be observed from the electric field distributions at the corresponding frequencies.

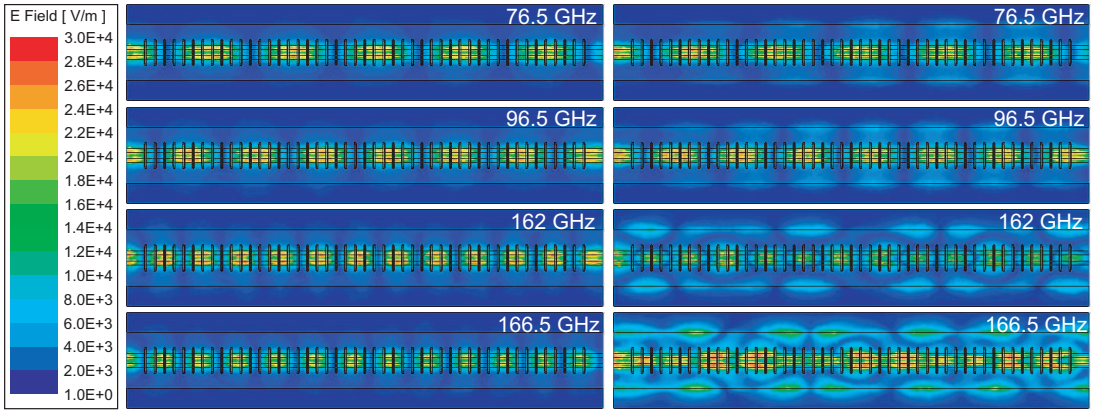

Figure 2.13: Electric field distributions at different frequencies of the CPW with both absorber layer and wire bonding bridges (left column) and the CPW with wire bonding bridges solely (right column) when the length is 5 mm.

The designed CPW with hollow plated vias is shown in Fig. 2.14. The vias are formed by drilling through-holes on the AlN substrate and covering the inner cross-sections with a thin layer of conductor. Since the electric waves cannot go through the conductor layer, the vias are filled with air while conductive glue or other materials can also be used. Due to fabrication limitations, the diameter of the vias cannot be smaller than the thickness of the substrate and the edge of the vias should be at least 63.5 μm away from the edge of the conductor on both sides. As a result, the diameter of the vias is 127 μm and the center-to-center distance between two vias is 254 μm which should be at least twice as the diameter. Besides, another conductor layer is added on the backside of the AlN substrate for supporting the hollow plated vias and it has a thickness of 1.2 μm. The width of the substrate is increased to 1.4 mm and the dimensions of the traces are optimized. The width of the signal trace is 60 μm and the width of the ground trace is 254 μm with a gap width of 34 μm.

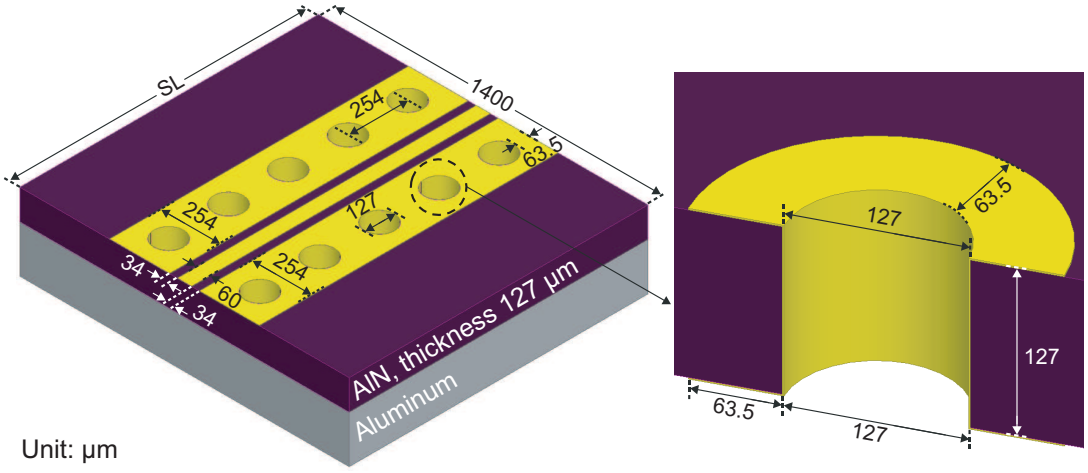

Figure 2.14: CPW with hollow plated vias.

The red solid lines in Fig. 2.15 show the simulation results of the CPW with hollow plated vias while the blue dashed lines are the simulation results when the POM absorber layer and wire bonding bridges are used. In both situations, the length of the CPW is around 5 mm. The simulated insertion loss is less than 1 dB up to 116 GHz and it increases to 3.4 dB at 168 GHz while the return loss is better than 15 dB up to 170 GHz. In comparison, lower insertion loss and better return loss have been achieved by the CPW with hollow plated vias from DC to 133 GHz while the CPW with the POM absorber layer and wire bonding bridges behaves more stable from 133 GHz to 170 GHz.

Fig. 2.16 shows the electric field distributions at different frequencies of the CPW with hollow plated vias when the length is around 5 mm in comparison with the CPW with both absorber layer and wire bonding bridges. By investigating the electric field distributions of the CPW with hollow plated vias at 160.5 GHz and 168 GHz, it can be concluded that the losses above 133 GHz on the S-parameters are mainly caused by the leakage of electric fields from the gaps between the vias. If the minimum distance between the vias and the edge of the ground traces can be further reduced by using more advanced fabrication technologies, it should be possible to improve the transmission performance especially at high frequencies.

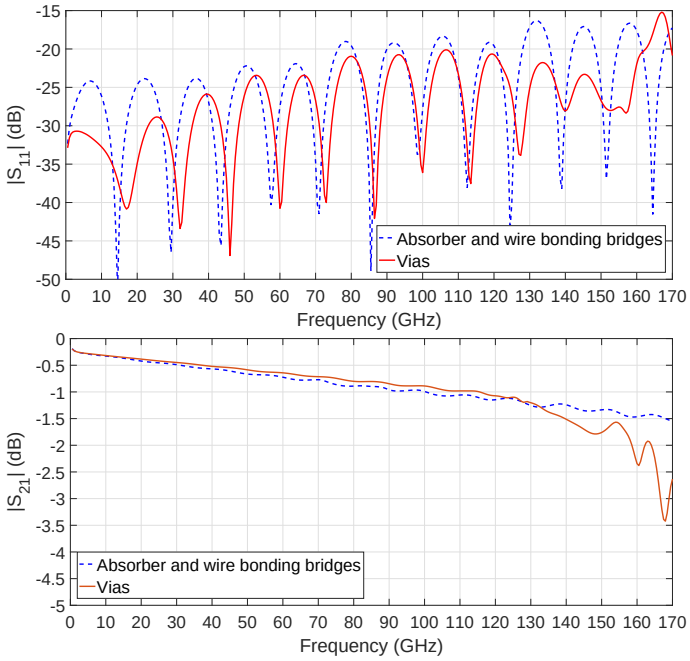

Figure 2.15: Simulation results of the CPW with hollow plated vias (red solid lines) and the CPW with an absorber layer and wire bonding bridges (blue dashed lines).

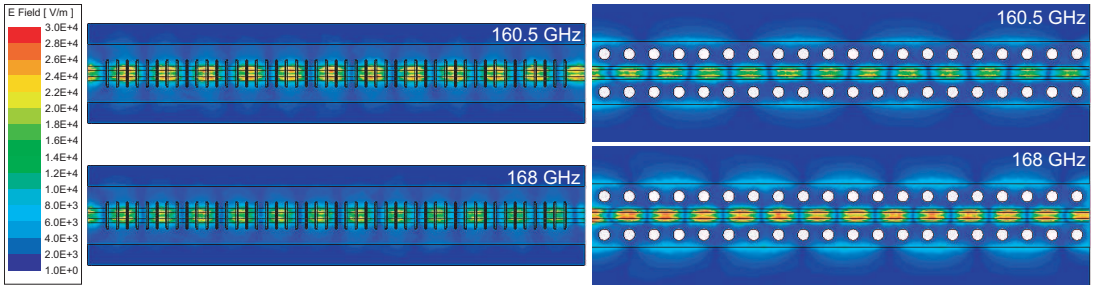

Figure 2.16: Electric field distributions at different frequencies of the CPW with both absorber layer and wire bonding bridges (left column) and the CPW with hollow plated vias (right column) when the length is around 5 mm.

2.1.2 Coplanar Stripline

Though the signals are connected to the interposer and guided by the CPWs at the beginning, CPSs with a configuration of ground-signal (GS) are employed at the end of the paths on the interposer in order to feed the transmitted signals to the MZM. Based on an uniplanar structure, the ground trace is placed next to the signal trace on the top of the substrate. For a conventional CPS, the signal and ground traces have the same width and the electric waves mainly exist in the gap between them. As a result, the characteristic impedance is independent from the substrate properties to some extent and it is mainly related to the width of the signal trace and the width of the gap in the middle. Though the ground trace plays a minor role in affecting the characteristic impedance, it has to be wide enough in order to support the propagation mode. In some cases, the width of the ground

trace is different from the width of the signal trace which then forms the so-called asymmetric coplanar stripline (ACPS). Fig. 2.17 shows the basic structure of a CPS based on AlN substrate with a bottom ground plane. The CPS is originally designed to have a characteristic impedance of 50 Ω based on the same AlN substrate with radiation boundary conditions and the bottom ground plane under the substrate is added in the simulation afterwards for a more realistic situation. The width of the signal and ground traces is 220 μm and there is a 20 μm gap in the middle. The AlN substrate has a thickness of 127 μm and its width is 1000 μm. Besides, the excitation scheme and the port field for simulating CPSs in ANSYS are also illustrated in Fig. 2.17.

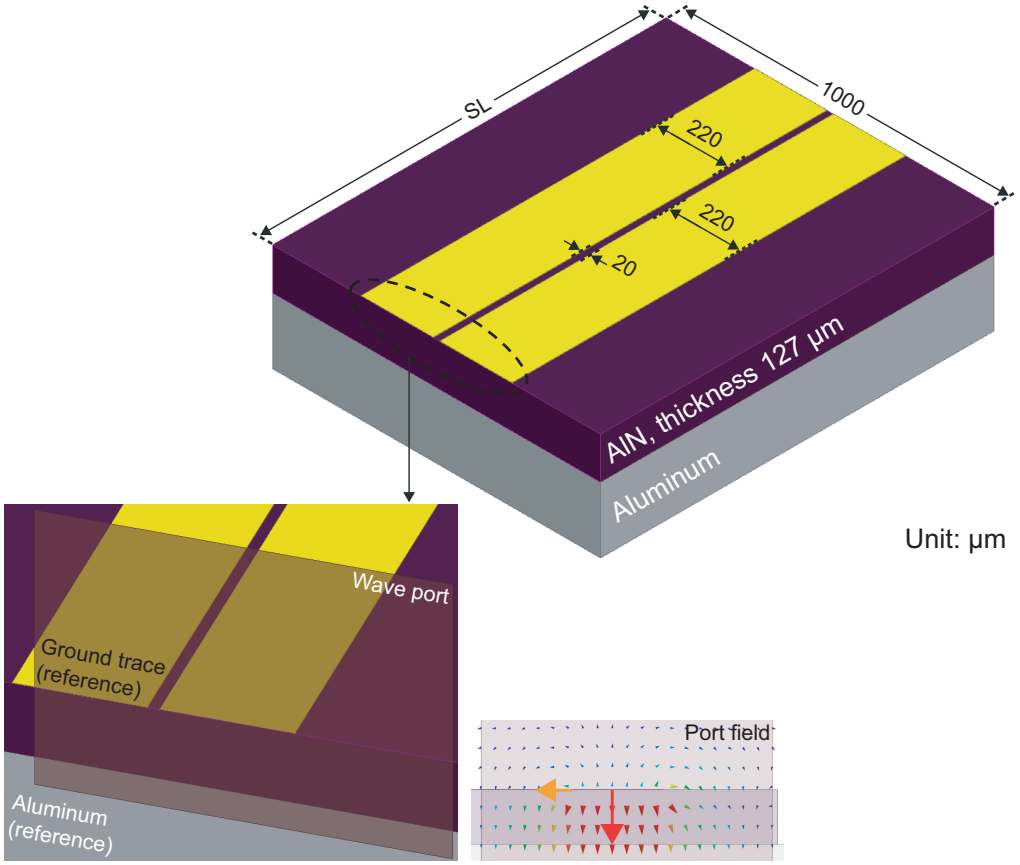

Figure 2.17: CPS based on AlN substrate with a bottom ground plane and the port excitation scheme used for simulations.

In the simulation, wave ports are used as the excitation scheme which work as semi-infinite waveguides guiding the electromagnetic waves from infinity to the port surfaces. An air cavity located on the top of the substrate with radiation boundary conditions is also included for accuracy improvement. According to the requirement of the simulator, wave ports should be assigned to the sheet either on the edge of the simulation space or inside the simulation space connected to a PEC object. In order to generate the port field correctly, the ground trace as well as the bottom ground plane are touched by the edges of the wave port and they are selected to be the references. Besides, the wave port needs to be large enough so that the electric waves would not couple to the edges instead of the ground trace and bottom ground plane. As is shown in Fig. 2.17, due to the

thin AlN substrate, the electric fields exist not only in the gap but also between the signal trace and the bottom ground plane. Fig. 2.18 shows the simulation results of the CPS with a bottom ground plane. The blue solid lines are the simulated S-parameters when the length is 1.2 mm while the red solid lines are the simulation results for 5 mm. In both cases, the performances are affected by the notches which appear at much lower frequencies when the length increases.

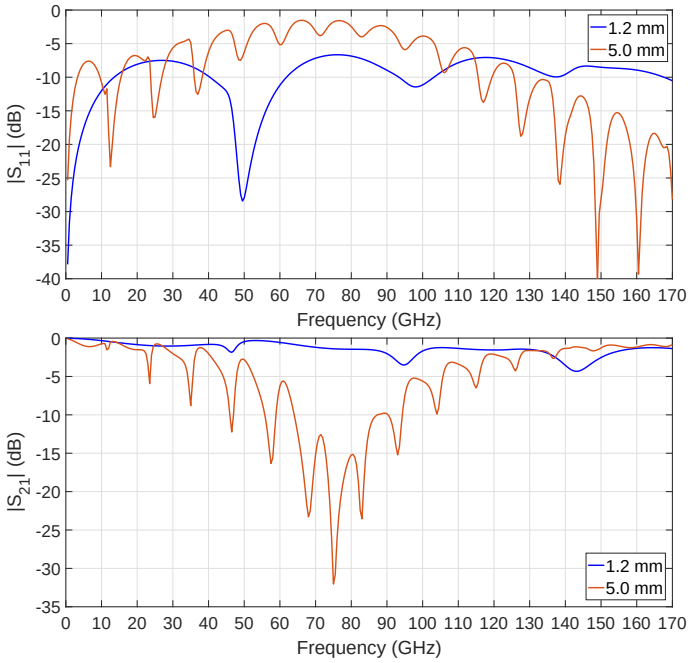

Figure 2.18: Simulation results of the CPS with a bottom ground plane based on different SL values.

Fig. 2.19 shows the electric field distributions of the CPS with a length of 5 mm at 23.5 GHz, 57.5 GHz, and 75 GHz which are among the resonant frequencies. At these frequencies, the designed CPS exhibits higher-order microstrip-like modes in which situation the energy radiates into free space and leakages from the edges of the signal and ground traces. These parasitic modes cause the notches as well as losses on the S-parameters which leads to the degradation of transmission performance.

Since there is only one ground trace on the top, the wire bonding bridges are not applicable for the CPS. As is shown in Fig. 2.20, either an absorber layer underneath or hollow plated vias going through the AlN substrate are implemented to restrict parasitic modes. The thickness of the absorber layer is 3.5 mm and the material is POM which is same as those used for the CPW. By inserting the POM absorber layer underneath, the bottom ground plane is moved away from the top conductors which helps restricting the parasitic modes. However, when hollow plated vias are added, another conductor layer has to be added on the backside of the AlN substrate and the width of the ground trace increases to 254 μm due to fabrication limitations. The vias are the same as it illustrated in Fig. 2.14 and due to the implementation of vias on the ground trace the electric field distribution is also changed. As a result, for achieving a characteristic impedance of 50 Ω, the width of the signal trace is optimized to be 130 μm with a 50 μm gap which forms an ACPS

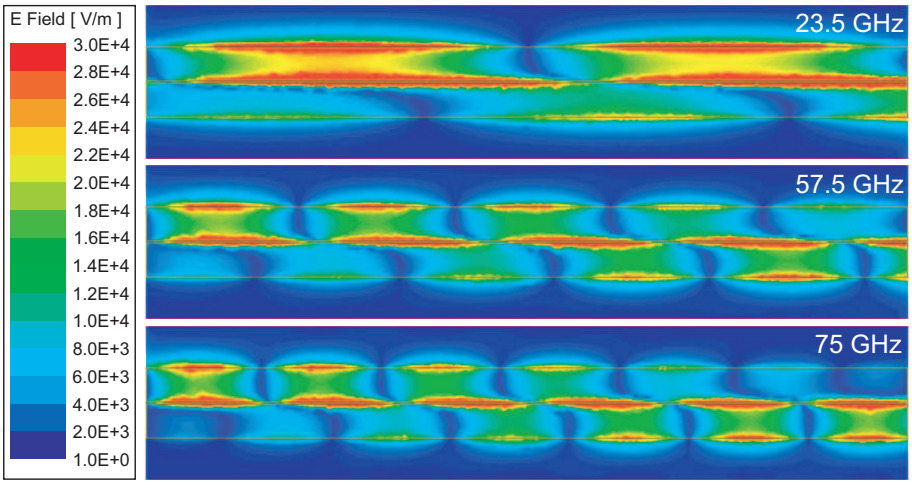

Figure 2.19: Electric field distributions of the CPS with a length of 5 mm at different frequencies.

instead of a conventional CPS.

The blue solid lines in Fig. 2.21 show the simulation results of the CPS with the POM absorber layer while the red solid lines are the simulation results when hollow plated vias are added. In both situations, the length of the transmission line is around 5 mm. For the CPS with the POM absorber layer, a bandwidth of 50 GHz is achieved. From DC to 50 GHz, the simulated insertion loss is less than 3 dB and the return loss is better than 14.3 dB. In comparison, the ACPS with hollow plated vias achieves a bandwidth of 170 GHz, in which the insertion loss is less than 1 dB and the return loss is better than 16.3 dB.

The designed ACPS with hollow plated vias shows a much larger bandwidth compared with the CPS with the POM absorber layer. This can be explained by looking at the electric field distributions at different frequencies in Fig. 2.22. For the CPS with the POM absorber layer, especially above 50 GHz, the leakage of electric fields becomes serious while the ACPS with hollow plated vias exhibits a stable propagation mode up to 170 GHz. Though the parasitic modes are suppressed by the absorber layer, the high level of energy leakage still results in a high insertion loss which corresponds to a small bandwidth.

2.1.3 Coplanar Waveguide-to-Coplanar Stripline Transitions

When both the CPWs and CPSs are employed on the interposer, the coplanar transitions between them become a necessary part of the interposer and play a critical role in affecting the bandwidth of the paths. The designs of the CPW and CPS based on the thin AlN substrate have been introduced in Section 2.1.1 and Section 2.1.2, respectively. Besides, the performances of suppressing parasitic modes by using different methods have been discussed. For driving single-ended signals, a CPW-to-CPS transition using wire bonding bridges together with an absorber layer and a CPW-to-ACPS transition using hollow plated vias going through the substrate are designed, fabricated, and measured.

Fig. 2.23 shows the proposed CPW-to-CPS transition in a back-to-back configuration using wire bonding bridges together with an absorber layer. The AlN substrate is 2286 μm in length

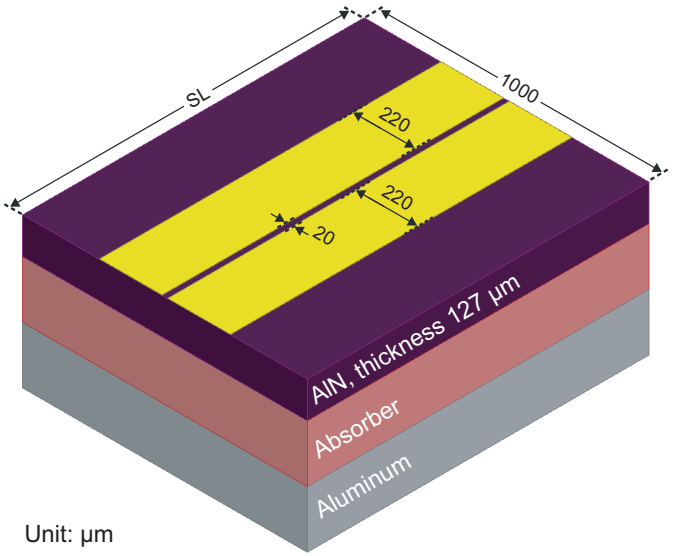

(a) CPS with an absorber layer.

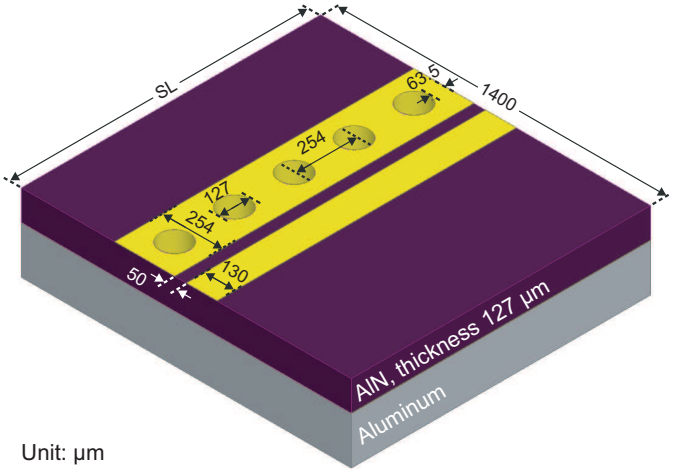

(b) ACPS with hollow plated vias.

Figure 2.20: CPS based on AlN substrate with different methods for suppressing parasitic modes.

and 1000 μm in width with a thickness of 127 μm. In order to suppress parasitic modes, the POM absorber layer with a thickness of 3.5 mm and the wire bonding bridges along the transition are implemented. The diameter, height, and length of the wire bonding bridges are 25 μm, 50 μm, and 255 μm, respectively. The distance between two wire bonding bridges is 100 μm. The back-to-back structure consists of two CPWs with a length of 330 μm, a CPS with a length of 426 μm in the middle, and two transitions with a length of 600 μm. The details of the proposed transition structure are also demonstrated in Fig. 2.23. The CPW is in a configuration of GSG where the width of the signal trace is 65 μm and the width of the ground traces is 220 μm with a gap of 40 μm. The CPS is in a configuration of GS where both the signal and ground traces have a width of 220 μm and they are separated by a 20 μm gap in the middle. When the CPW is connected to the CPS, one of the ground traces continues while the other one has to be terminated and the signal trace needs

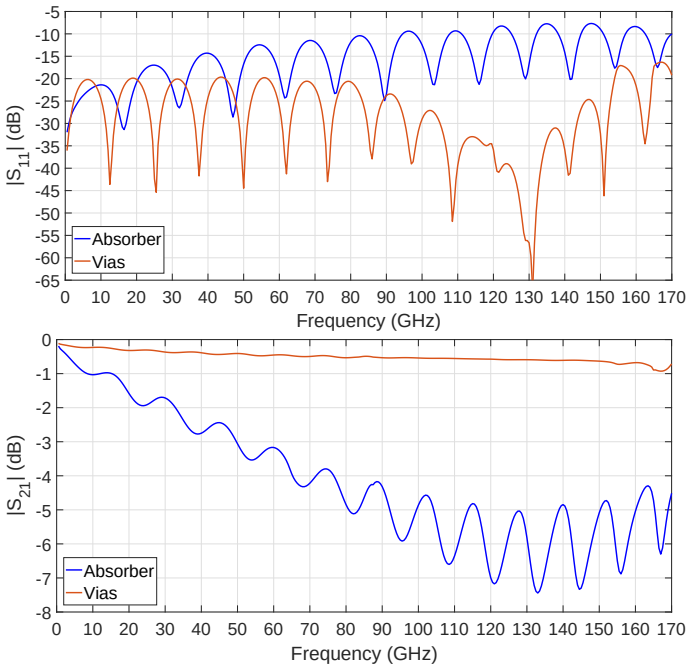

Figure 2.21: Simulation results the CPS with the POM absorber layer (blue solid lines) and the ACPS with hollow plated vias (red solid lines).

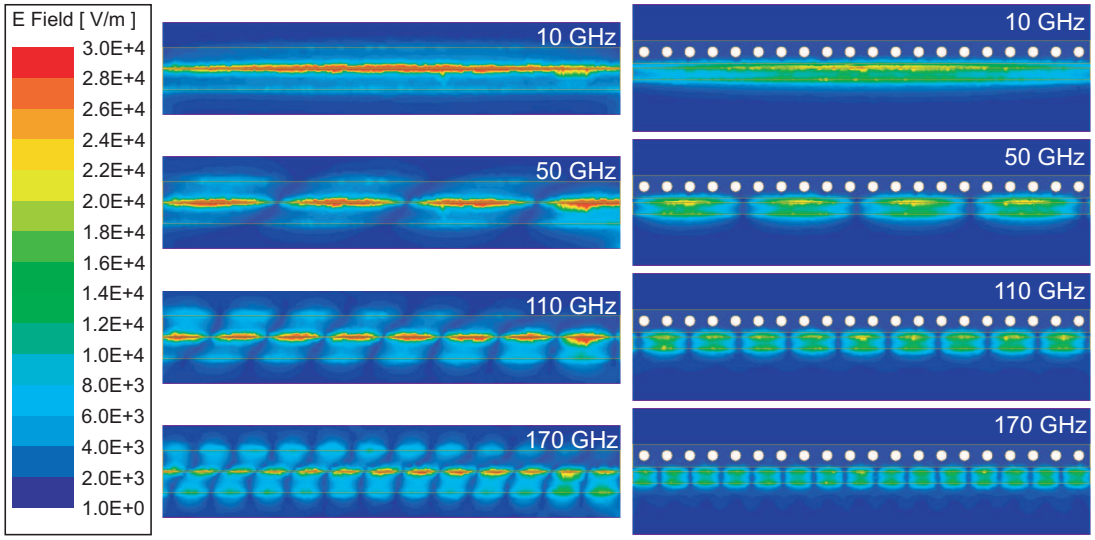

Figure 2.22: Electric field distributions at different frequencies of the CPS with the POM absorber layer (left column) and the ACPS with hollow plated vias (right column) when the length is around 5 mm.

to be tapered out in order to compensate the width difference. At the beginning of the proposed transition structure, one of the ground traces is tapered in from 220 μm to 110 μm within a distance of 400 μm and terminated afterwards. Since the width of the gap reduces from 40 μm to 20 μm, the signal trace is tapered out on both edges and the length of the tapered structure is 200 μm.

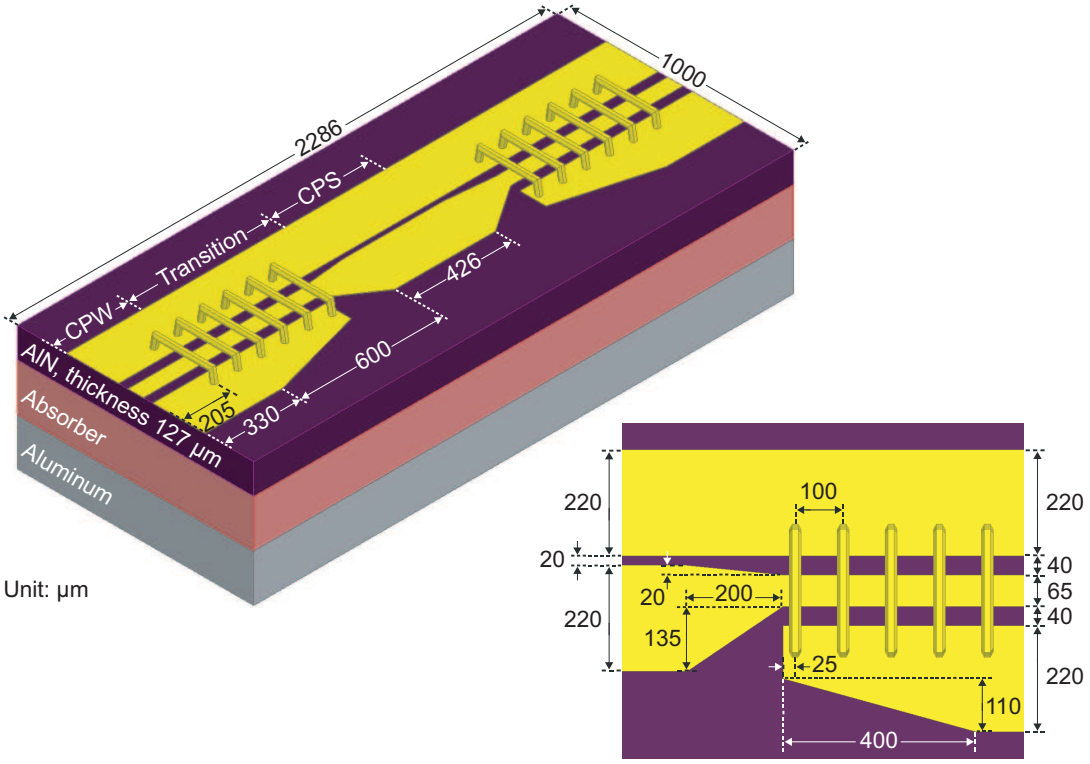

Figure 2.23: CPW-to-CPS transition in a back-to-back configuration using wire bonding bridges together with an absorber layer.

The simulated S-parameters of the CPW-to-CPS transitions in a back-to-back configuration are shown in Fig. 2.24. The red solid lines represent the simulation results of the proposed transition when both the POM absorber layer and wire bonding bridges are implemented. In this case, the proposed transition achieves a bandwidth of 85 GHz where the insertion loss is less than 3 dB and the return loss is better than 10 dB. The blue dashed lines are the simulation results of the proposed transition using the POM absorber layer solely. Though the absorber layer is added between the AlN substrate and the bottom ground plane, a serious notch still appears at 34.5 GHz which degrades the transmission performance and results in a bandwidth of 11 GHz.

Based on the preliminary investigations of CPW and CPS structures, the parasitic modes caused by the bottom ground plane have been successfully suppressed by the POM absorber layer. Thus the notch at 34.5 GHz is likely to be caused by the transition structure instead of the parasitic modes on the transmission lines. Fig. 2.25 shows the electric field distributions of the proposed CPW-to-CPS transition using wire bonding bridges together with an absorber layer in comparison with the situation when the absorber layer is implemented alone. At 10 GHz and 80 GHz, the electric field distributions in both cases are similar to each other and adding wire bonding bridges

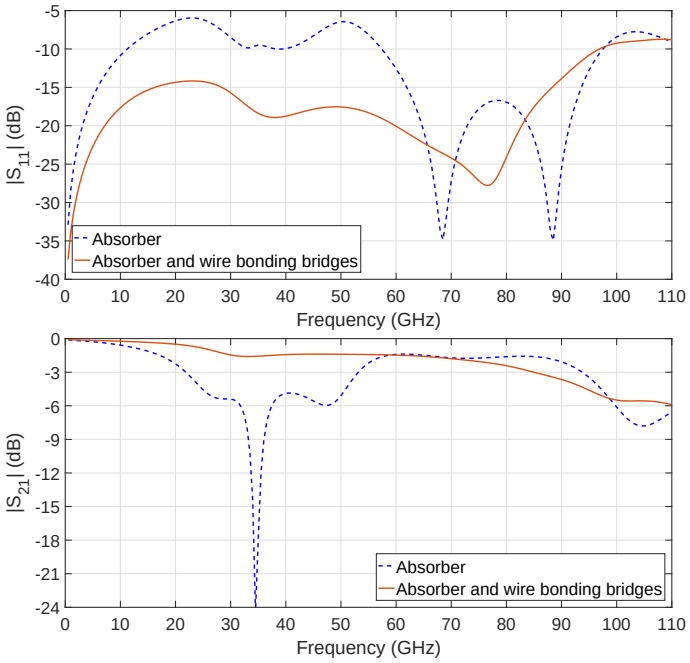

Figure 2.24: Simulation results of the CPW-to-CPS transition using an absorber layer solely (blue dashed lines) and the CPW-to-CPS transition using wire bonding bridges together with an absorber layer (red solid lines).

on the top does not make much difference. At 34.5 GHz, strong radiations can be observed from the terminations of the ground traces when wire bonding bridges are removed and it is the reason that causes the serious notch on the S-parameters.

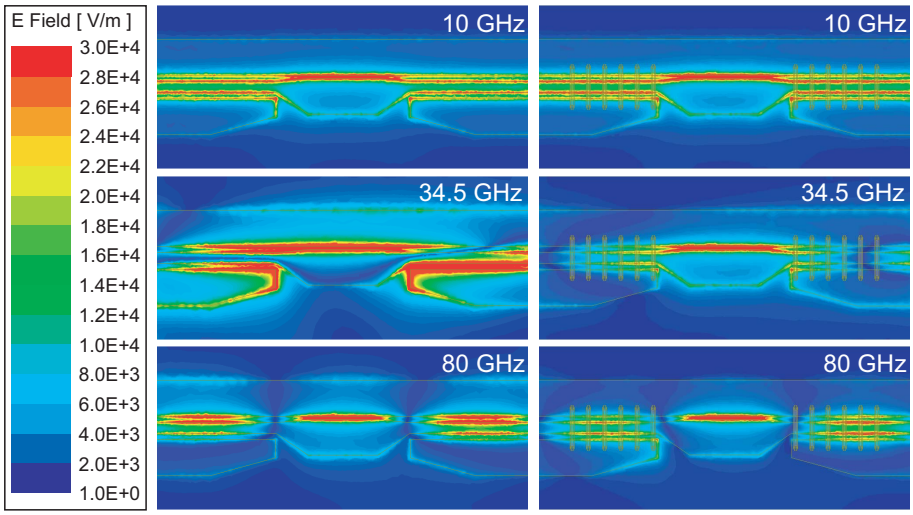

Figure 2.25: Electric field distributions at different frequencies of the CPW-to-CPS transition using an absorber layer solely (left column) and the CPW-to-CPS transition using wire bonding bridges together with an absorber layer (right column).

In order to illustrate the transmission and conversion of the propagation mode at the transition

structure, the electric field distributions at different cross-sections of the proposed CPW-to-CPS transition using both absorber layer and wire bonding bridges at 80 GHz are shown in Fig. 2.26. The cross-sections corresponds to the locations marked with the same letters. At the beginning of the transition structure, the electric fields mainly exist in the gaps between the signal and ground traces which corresponds to a CPW mode. Part of the electric fields are also coupled from the signal trace to the wire bonding bridges on the top. When one of the ground trace is tapered in and terminated gradually, the electric fields move from one gap to another. The strong electric fields between the signal trace and the wire bonding bridges indicates it helps the migration and suppresses the radiation. After that the signal trace starts tapering out while the propagation mode is converted to a CPS mode.

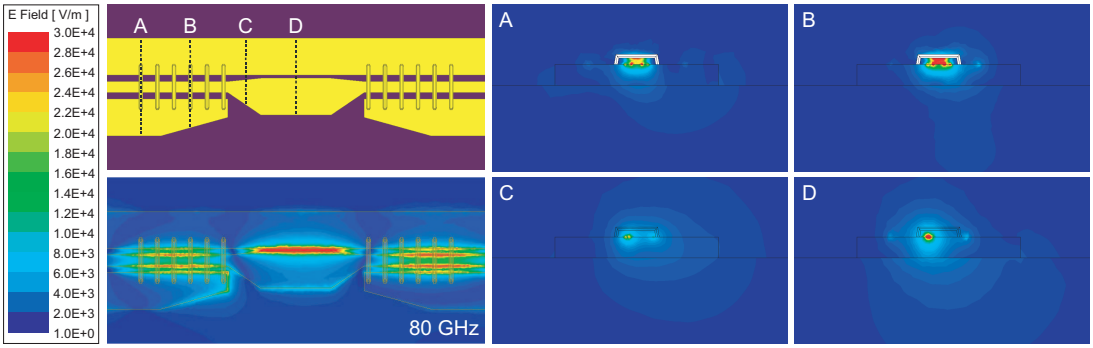

Figure 2.26: Electric field distributions at different cross-sections of the proposed CPW-to-CPS transition using wire bonding bridges together with an absorber layer at 80 GHz.

A prototype of the CPW-to-CPS transition shown in Fig. 2.23 was fabricated by Applied Thin-Film Product (ATP) with the purposes of proving the concepts and validating the designs. The transition was patterned on an AlN substrate with a thickness of 127 μm and the tolerance of the substrate thickness is 12.7 μm. The material of the conductor layer is gold and the thickness is 1.2 μm with a tolerance of 0.24 μm. The wire bonding bridges were made afterwards at Danchip (National Center for Micro- and Nanofabrication in Denmark). The diameter of the wire bonding bridges is 25 μm and the material is gold. The fabricated CPW-to-CPS transitions with and without wire bonding bridges are shown in Fig. 2.27.

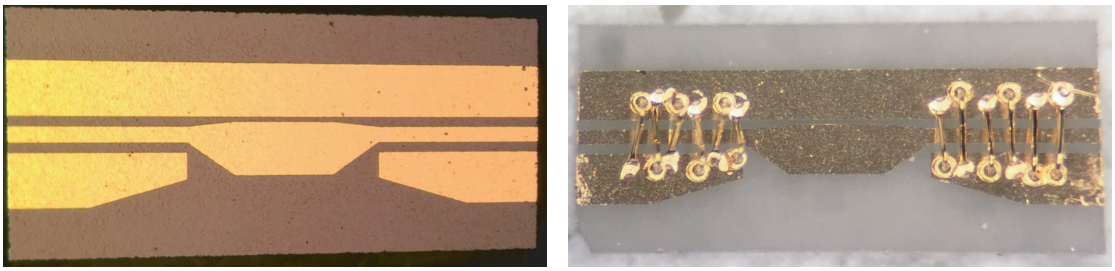

(a) Without wire bonding bridges. (b) With wire bonding bridges.

Figure 2.27: Fabricated CPW-to-CPS transitions in a back-to-back configuration based on an AlN substrate.

The fabricated CPW-to-CPS transition was characterized on-wafer from DC to 110 GHz using a probe station, a vector network analyzer and two GSG probes with 125 μm pitch. The red solid lines in Fig. 2.28 show the measurement results while the blue dashed lines are the simulation results. Since the bandwidth of the transition is referred as the width of the frequency band where the return loss is better than 10 dB and the insertion loss is less than 3 dB, the fabricated CPW-to-CPS transition in a back-to-back configuration achieves a bandwidth of 80 GHz ranging from DC. In comparison, a reasonable agreement between the simulation and measurement results has been achieved. The differences are mainly caused by the fabrication tolerances, especially for the shape and uniformity of the wire bonding bridges which are hard to control during the fabrication process at Danchip.

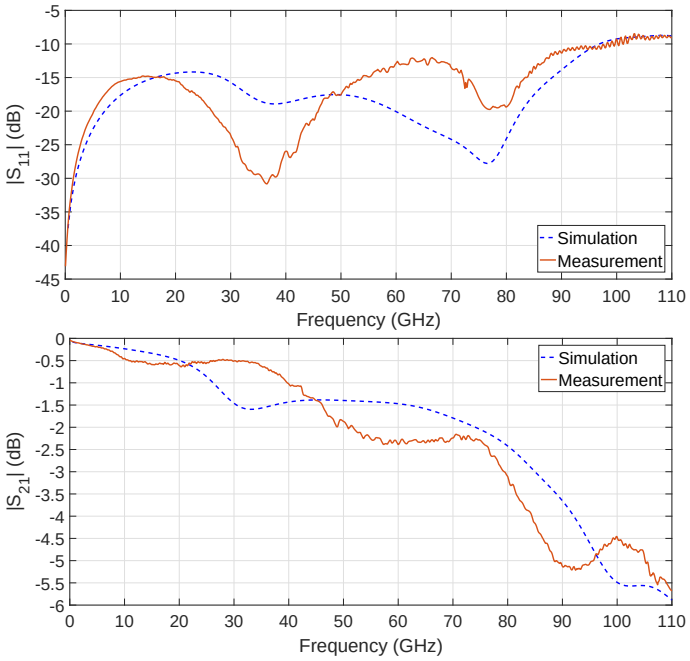

Figure 2.28: Measurement results of the CPW-to-CPS transition in a back-to-back configuration using wire bonding bridges together with an absorber layer.

When hollow plated vias are used for designing the transition, the width of the ground traces increases to 254 μm and another conductor layer is added on the backside of the AlN substrate for supporting the vias. For the CPW structure, the widths of the signal traces and the gaps reduce to 60 μm and 34 μm, respectively. For the CPS structure, the signal trace is optimized to have a width of 130 μm and a gap of 50 μm which becomes an ACPS. Instead of a CPW-to-CPS transition, it is classified as a CPW-to-ACPS transition. The proposed CPW-to-ACPS transition in a back-to-back configuration using hollow plated vias is shown in Fig. 2.29. The length and width of the AlN substrate increase to 2540 μm and 1400 μm, respectively, while the thickness is still 127 μm. The diameter of the hollow plated vias is 127 μm and the center-to-center distance between two vias is 254 μm, which according to the fabrication requirement has to be at least twice of the diameter. The back-to-back structure consists of two CPWs at the ends with a length of 635 μm, an ACPS in the middle with a length of 880 μm, and two transitions as interconnects with a length of 195 μm.

Fig. 2.29 also shows the details of the proposed transition structure. When the CPW is connected to the ACPS, one of the ground traces is reserved and connected directly to the ACPS without changing its dimension while the other one is terminated gradually forming a semicircle with a diameter of 254 μm. In order to compensate the differences in dimensions, the signal trace is tapered in on one edge where it moves 16 μm towards the center of the signal trace and the length of the tapered structure is 100 μm. On the other edge, the signal trace is tapered out for increasing the width where it moves 86 μm away from the center of the signal trace and the tapered structure follows the shape of the terminated ground trace forming an annular ring structure with a diameter of 322 μm. Besides, the red area on the tapered signal trace is chamfered in order to reduce the reflection caused by the termination of the ground trace and its length is 60 μm.

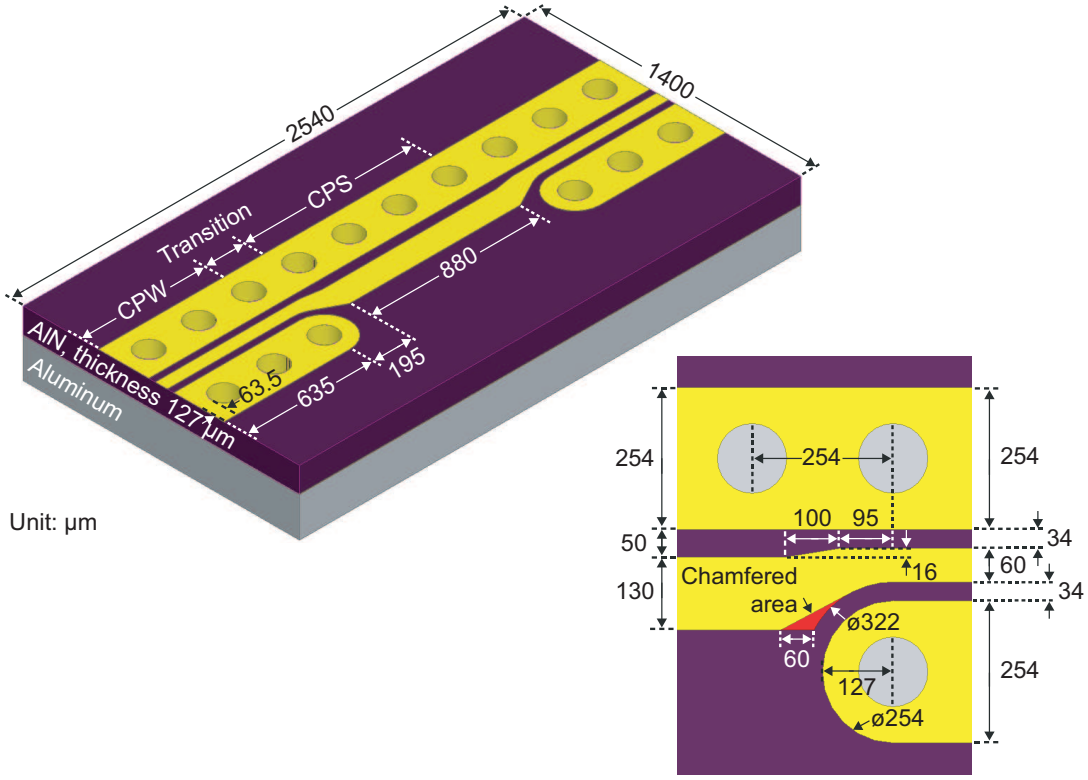

Figure 2.29: CPW-to-ACPS transition in a back-to-back configuration using hollow plated vias.

The red solid lines in Fig. 2.30 show the simulated S-parameters of the CPW-to-ACPS transition in a back-to-back configuration using hollow plated vias. The proposed transition is driven by a single-ended signal and a bandwidth of 170 GHz is achieved. In the whole frequency range, the simulated insertion loss is less than 2.8 dB and the return loss is better than 16 dB. Compared with the blue dashed lines which represent the the simulation results of the CPW-to-CPS transition using wire bonding bridges together with an absorber layer, the proposed CPW-to-ACPS transition using hollow plated vias exhibits a much larger bandwidth which makes it a competitive candidate for THz applications where the thick substrate, absorber layer, and extra structures on the top of the substrate have to be avoided due to the need for compact system integrations.

Fig. 2.31 illustrates the electric field distributions at different frequencies of the CPW-to-ACPS

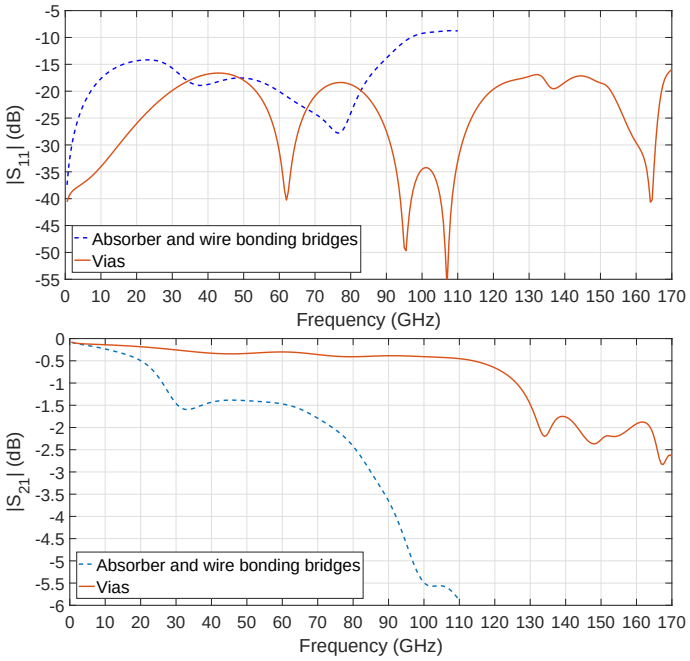

Figure 2.30: Simulation results of the CPW-to-ACPS transition using hollow plated vias (red solid lines) and the CPW-to-CPS transition using wire bonding bridges together with an absorber layer (blue dashed lines).

transition using hollow plated vias in compared with the CPW-to-CPS transition using wire bonding bridges together with an absorber layer. Though the parasitic modes are restricted successfully in both cases, the hollow plated vias show a better performance in preventing the leakage of electric fields at the transition structure especially at high frequencies which results in a lower insertion loss and thus a larger bandwidth.

Since the proposed CPW-to-ACPS transition using hollow plated vias exhibits a bandwidth of 170 GHz ranging from DC, the electric field distributions at 170 GHz is shown in Fig. 2.32. Compared with the electric field distributions at lower frequencies shown in Fig. 2.31, it is clear that part of the electric fields leaks from the gaps between the vias as well as the terminations of ground traces. By reducing the distance between the vias, it might be possible to further increase the bandwidth of the transition while more advanced fabrication technologies are needed. In addition, Fig. 2.32 shows the electric field distributions at different cross-sections of the CPW-to-ACPS transition using hollow plated vias. The cross-sections corresponds to the locations marked with the same letters. At the beginning of the transition structure, the electric fields mainly exist in the gaps between the signal and ground traces while part of them are also coupled to the bottom ground plane due to the thin AlN substrate. When one of the ground traces is terminated, the vias as well as the bottom ground plane help the electric fields move from one gap to another while part of the energy is also lost due to the radiation at the terminations. After that the signal trace is tapered out and the propagation mode is converted.

A prototype of the CPW-to-ACPS transition shown in Fig. 2.29 was fabricated by ATP in order to prove the concepts and validate the designs. The AlN substrate as well as the gold conductor

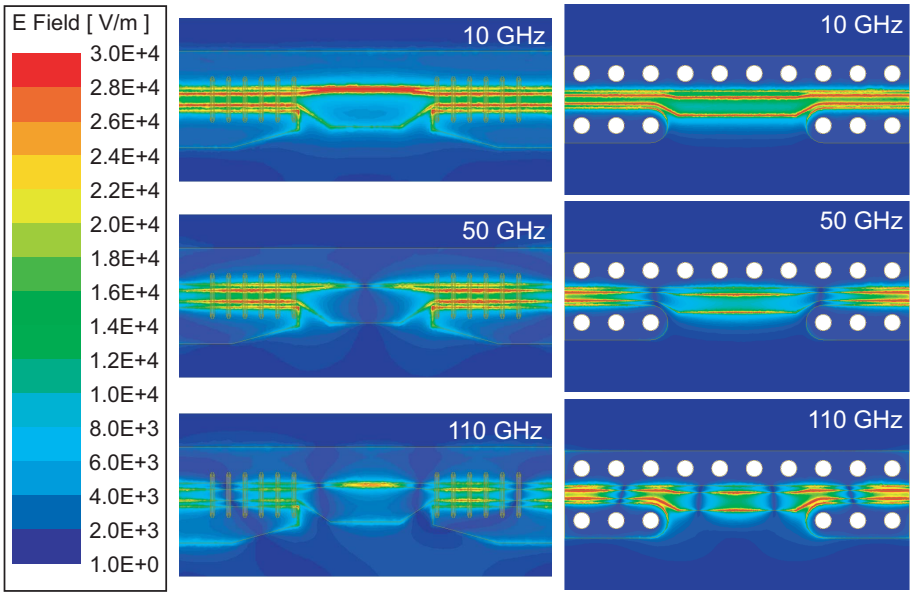

Figure 2.31: Electric field distributions at different frequencies of the CPW-to-ACPS transition using hollow plated vias (right column) and the CPW-to-CPS transition using wire bonding bridges together with an absorber layer (left column).

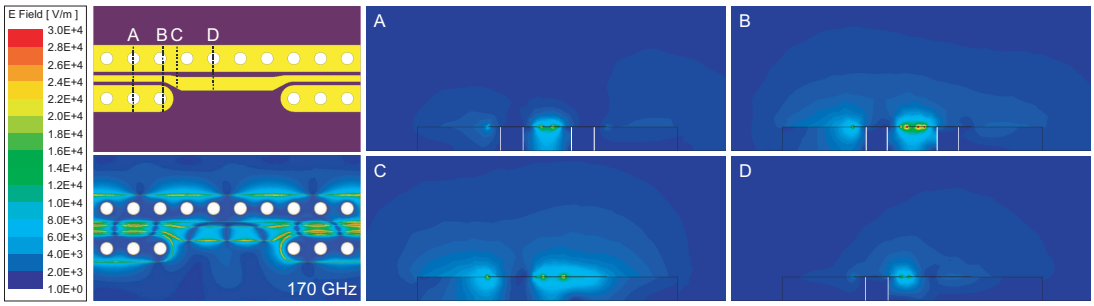

Figure 2.32: Electric field distributions at different cross-sections of the CPW-to-ACPS transition using hollow plated vias at 170 GHz.

layer are the same as those used for fabricating the CPW-to-CPS transition. The vias going through the AlN substrate are hollow plated inside by covering the inner cross-sections with a thin layer of gold conductor. The vias are filled with air and their diameter is 127 μm with a tolerance of 25.4 μm. The top and bottom views of the fabricated CPW-to-ACPS transition in a back-to-back configuration based on AlN substrate are shown in Fig. 2.33. It can be seen under the microscope that due to the fabrication processes at ATP, the vias are not completely identical and the gold conductors seem to have a high surface roughness.

The fabricated CPW-to-ACPS transition was characterized on-wafer from DC to 170 GHz using a probe station, a vector network analyzer and two GSG probes with 125 μm pitch. The two-port S-parameters were firstly measured from DC to 110 GHz and then the setup was reconfigured for the on-wafer measurement from 110 GHz to 170 GHz. The measurement results are shown by the red solid lines in Fig. 2.34 while the blue dashed lines represent the simulation results. Since the

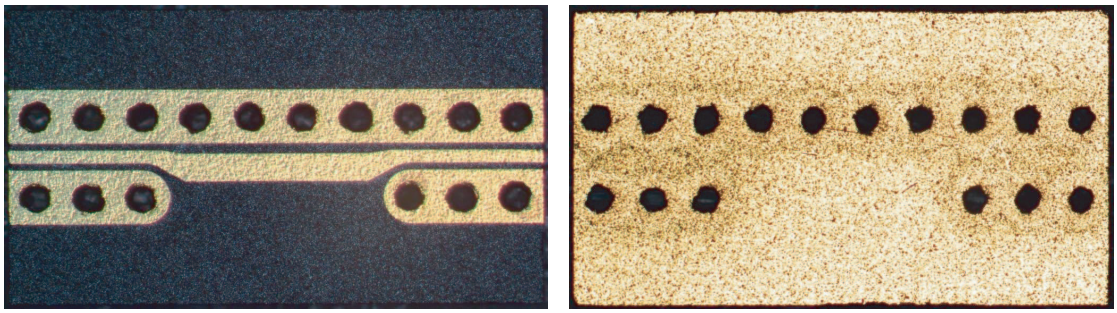

(a) Top view. (b) Bottom view.

Figure 2.33: Fabricated CPW-to-ACPS transition in a back-to-back configuration based on AlN substrate with hollow plated vias.

bandwidth is referred as the width of the frequency band where the return loss is better than 10 dB and the insertion loss is less than 3 dB, the fabricated CPW-to-ACPS transition in a back-to-back configuration achieves a bandwidth of 165 GHz ranging from DC. In comparison, a reasonable agreement between simulation and measurement has been achieved. The differences between simulation and measurement results are mainly caused by the variation of electrical properties for the AlN substrate in terms of frequency as well as the fabrication tolerances, especially for the surface roughness of the gold conductors and the uniformity of the vias. In Table. 2.1, the performances of the proposed coplanar transitions in a back-to-back configuration based on AlN substrate are summarized.

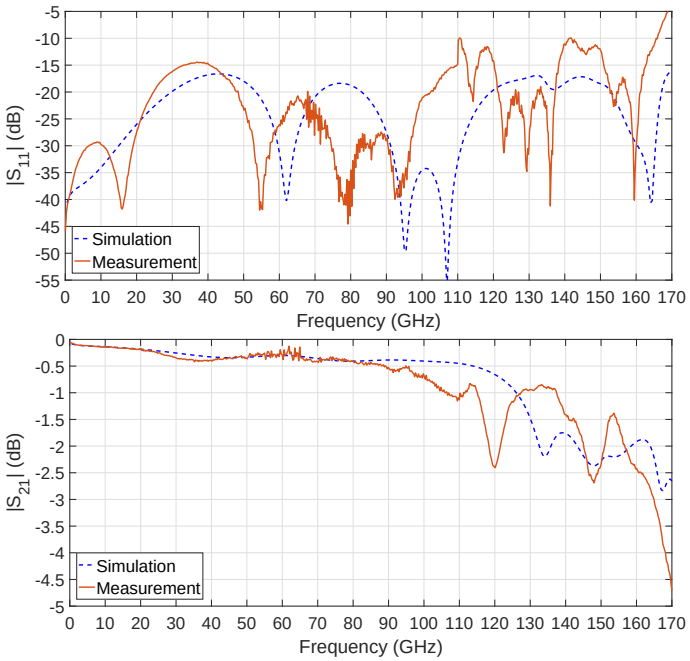

Figure 2.34: Measurement results of the CPW-to-ACPS transition in a back-to-back configuration using hollow plated vias.

Table 2.1: Coplanar transitions based on AlN substrate for single-ended signal

Transition type	Substrate	Method	Structure	Bandwidth*
CPW-to-CPS	AlN, 127 μm	POM absorber layer and wire bonding bridges	Back-to-back	80 GHz
CPW-to-ACPS	AlN, 127 μm	Hollow plated vias	Back-to-back	165 GHz

*The bandwidth is defined as the frequency band where the insertion loss is less than 3 dB and the return loss is better than 10 dB.

2.2 Interposer Design

For the system integration of the terabit transmitter, the interposer works as a connection between the DRVs and MZM. Fig. 2.35 illustrates the outline and the pads of the DRV chip which is based on an InP substrate with a thickness of 160 μm. The length and width of the chip are 3000 μm and 1800 μm, respectively. When the DRV is used for driving single-ended signals, the output is in a configuration of GSG and the dimensions of the pads are also shown in Fig. 2.35. As a part of PANTHER project, the DRV was designed and fabricated at III-V Lab, Palaiseau, France [82]. During the preliminary research, the performance of wire bonding connections between the DRV and the interposer was discussed in [46].

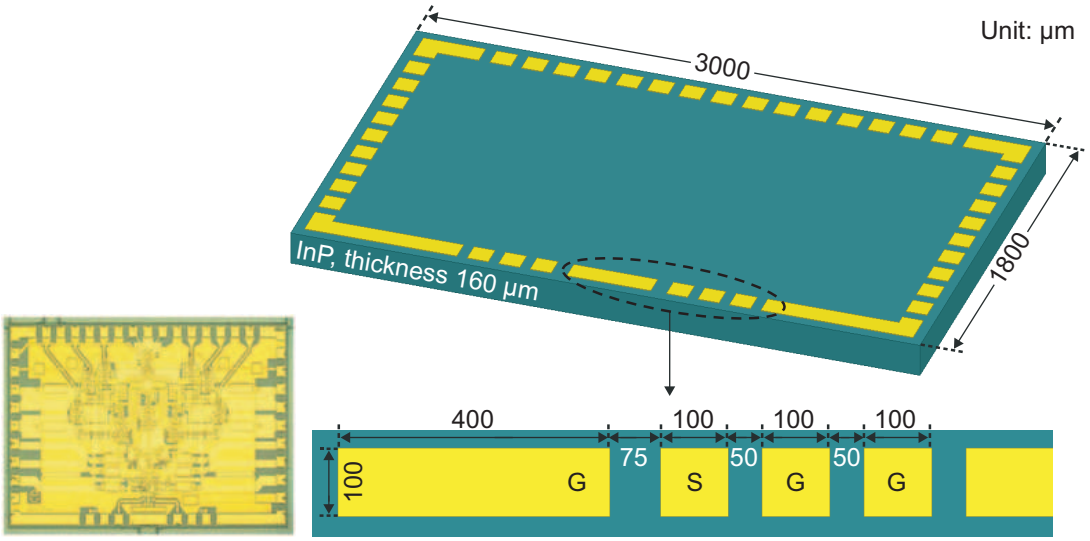

Figure 2.35: Chip outline, layout, and the fabricated DRV at III-V Lab.

Apart from the DRV, the MZM as another critical component involved in the system integration of the transmitter is demonstrated in Fig. 2.36. The MZM is based on an InP substrate and the thickness is 210 μm. The chip has a length of 10000 μm and a width of 2160 μm. When the MZM is configured for driving single-ended signals, four signal traces are connected at the same time and each input is in a configuration of GS. The length and width of the pads are 219 μm and 151 μm, respectively. The gap between the signal and ground traces is 18 μm. By going through the paths on the interposer, the electrical signals are guided to the MZM and modulated with the optical signals. As a part of PANTHER project, the MZM was designed and fabricated at Fraunhofer-Institut für Nachrichtentechnik, Heinrich-Hertz-Institut (Fraunhofer HHI), Berlin, Germany.

As is shown in Fig. 2.1, the interposer on the top and the MZM underneath have to be connected

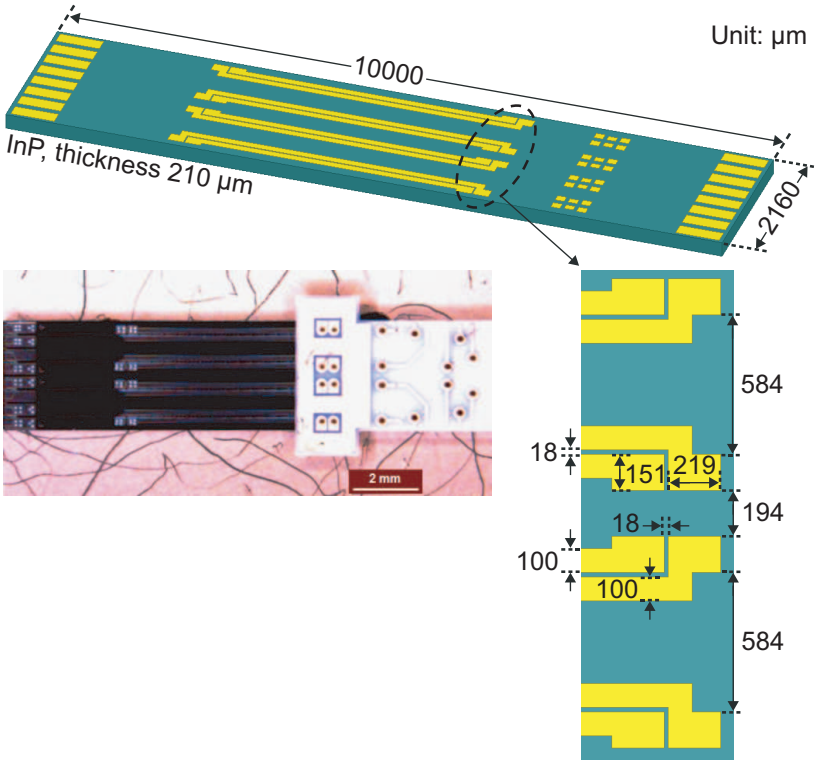

Figure 2.36: Chip outline, layout and the fabricated MZM at Fraunhofer HHI.

vertically which should be able to support data transmissions starting from DC. Therefor, hollow plated vias going through the AlN substrate are used as the vertical connections for the system integration of the terabit transmitter. Fig. 2.37 illustrates the structure of the vertical connections. Due to the fabrication requirements, the hollow plated vias follow the shape of a circular cone whose diameter is 100 μm on the top and 150 μm on the bottom, respectively. Besides, for each hollow plated via, an annular ring with a diameter of 230 μm needs to be added on the top of the AlN substrate and filled with silver epoxy in order to fix the interposer and provide sufficient connections. As a part of the preliminary research, the performance and equivalent circuit model of the vias being used as the vertical connections were also explained in [46].

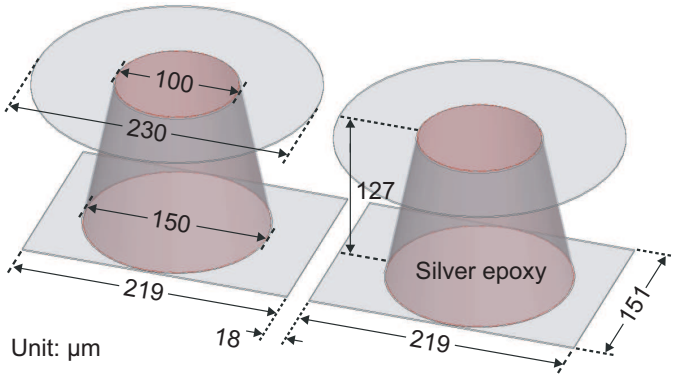

Figure 2.37: Hollow plated vias going through the AlN substrate.

The interposer is used as the transmission line guiding single-ended signals from the outputs of the DRVs to the inputs of the MZM. In order to be compatible with the DRVs and MZM, the inputs of the interposer need to be a GSG configuration while the outputs of the interposer should have a GS configuration. Besides, the interposer is located on the top of the MZM which means the method using hollow plated vias on the ground traces are not applicable since the extra conductor layer cannot be added on the backside of the substrate. As a result, wire bonding bridges on the top of the interposer together with an absorber layer under the MZM are used to restrict parasitic modes on the interposer. By combining the planar transmission lines and the coplanar transition introduced in Section 2.1.1, Section 2.1.2, and Section 2.1.3, the interposer is designed based on the same AlN substrate with a thickness of 127 μm whose performance has been proved by the fabricated transition prototypes. The alumina substrate with a thickness of 1600 μm provided by ATP is selected to be used as the absorber layer for the system integration. The ϵ_r and tanδ of the alumina substrate measured at 10 GHz are 9.7 and 2e-4, respectively. The substrate consists of 99.6% Al_2O_3 and 0.4% impurities. Since four single-ended signals (S1, S2, S3, S4) are guided through the paths on the interposer at the same time, the paths are carefully designed to have the same physical path length which guaranties the phase balance among different signal traces.

Fig. 2.38 shows the structure of the proposed interposer. Due to the symmetrical layout of the MZM, S1 and S2 are the same as S3 and S4, respectively. Each path consists of a CPW-to-CPS transition with wire bonding bridges, two CPSs, two CPS quadrants, and a vertical connection going through the AlN substrate to the input of the MZM. The physical length of each individual part that is involved in designing the interposer is listed in Table. 2.2. All signal traces on the interposer have the same physical path length which is calculated to be 4113 μm. For easier alignment and fabrication, the interposer is divided into three pieces. The interposer piece in the middle, having the same width as the MZM, is firstly integrated on the top of the MZM by using silver epoxy and then it connects to the rest two identical interposer pieces on both sides by using wire bonding connections. For each trace, four wire bonding connections are used in parallel with the purposes of providing stable physical connections as well as reducing the parasitic inductance introduced by the thin wires, especially at high frequencies.

Table 2.2: Physical lengths of individual parts involved in designing the interposer

Part	**Type**	**S1/S3**$^{+}$	**S2/S4**$^{++}$	**Length**
L1	CPW-to-CPS transition with wire bonding bridges	x	x	1030 μm
L2	CPS	x		1037.5 μm
L3	Inner path of the CPS quadrant	x	x	173 μm*
L4	CPS	x		1322.5 μm
L5	Outer path of the CPS quadrant	x	x	550 μm*
L6	CPS		x	2057.5 μm
L7	CPS		x	302.5 μm

*Approximate value which is calculated by using the radius in the middle of the trace.

$^{+}L_{S1,S3}$=L1+L2+L3+L4+L5=4113 μm.

$^{++}L_{S2,S4}$=L1+L3+L5+L6+L7=4113 μm.

Lumped ports are used as the excitation scheme for simulating the proposed interposer including

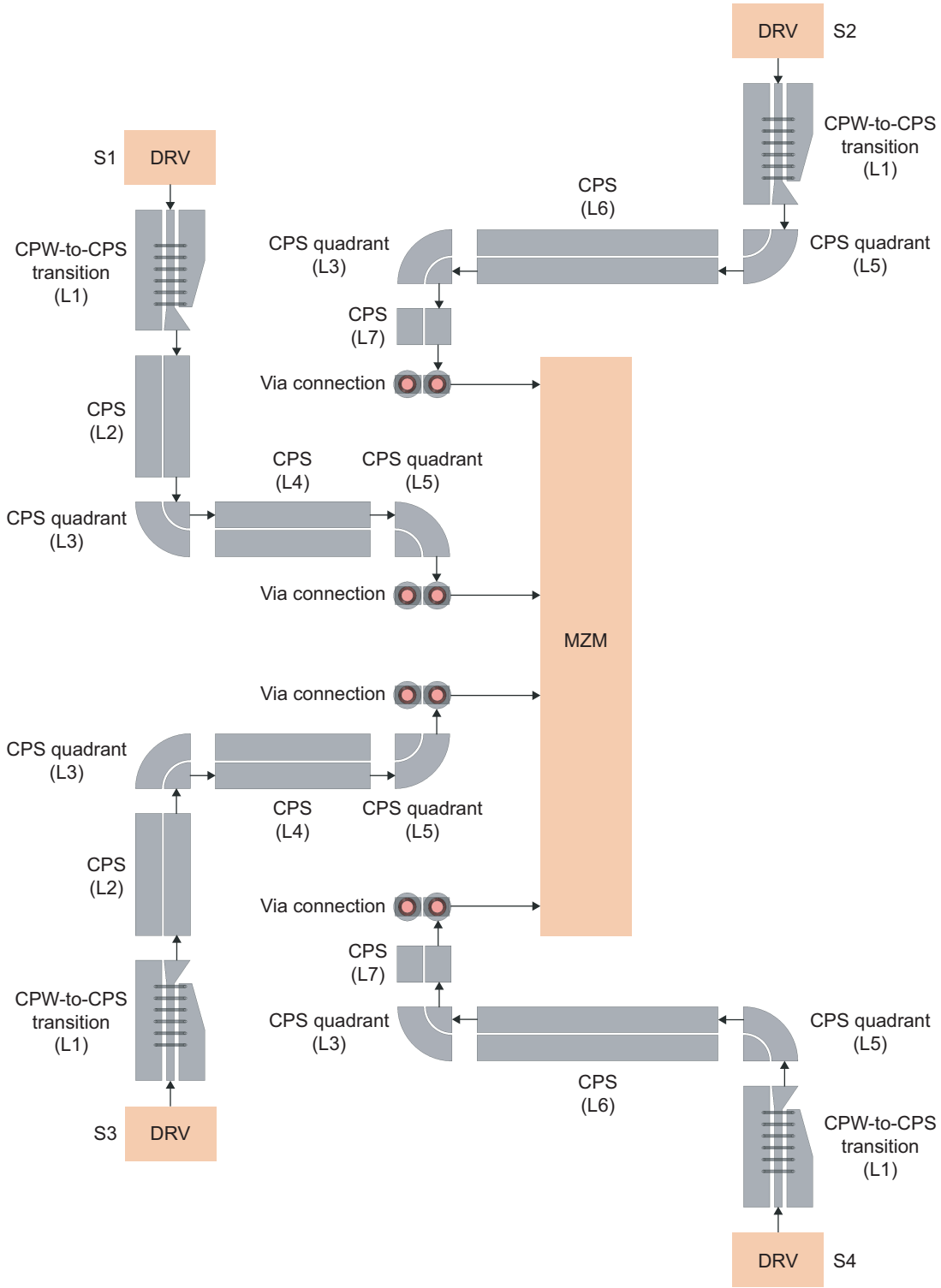

Figure 2.38: Interposer structure.

the via connections. Besides, in the simulation, an air cavity with radiation boundary conditions is added around the interposer structure for preventing the reflections caused by the surroundings. At the input of the interposer, the lumped ports are assigned to the vertical sheets located at the beginning of the paths between the signal traces and the vertical PEC bridges while at the output of the interposer, the lumped ports are assigned to the horizontal sheets located in the gaps between the signal and ground pads of the MZM. Due to the requirement of PANTHER project, the interposer needs to provide a bandwidth larger than 45 GHz ranging from DC. Fig. 2.39 shows the simulation results of the proposed interposer. Since the bandwidth is referred as the width of the frequency band where the return loss is better than 10 dB and the insertion loss is less than 3 dB, a simulated bandwidth of 51 GHz is achieved for S1 and S3 while it is 47.5 GHz for S2 and S4. Due to the wire bonding bridges along the CPW-to-CPS transitions and the alumina absorber layer underneath, the parasitic modes on the interposer are successfully restricted and there is no serious notch or resonance can be observed on the simulated S-parameters. Besides, when several signals are transmitted by the interposer simultaneously, it becomes essential to check the crosstalk intensity between different signal traces. As is shown in Fig. 2.39, the crosstalks between S1, S2, and S3 remain less than -20 dB which means the crosstalk effect on the interposer can be neglected. In addition, S2 and S4 locate far away from each other on the proposed interposer so that the crosstalk between them is even lower thus it is not included in Fig. 2.39.

Fig. 2.40 shows the electric field distributions of the proposed interposer at 45 GHz when it is driven by four single-ended signals. Though the parasitic modes are suppressed on the interposer, the leakage of electric fields is still noticeable especially on the CPS transmission lines. This phenomenon also follows the investigation of the CPS with an absorber layer whose electric field distributions are illustrated in Fig. 2.22. The bandwidth of the proposed interposer is mainly affected by the leakage of electric fields on the transmission lines as well as the parasitic inductance introduced by the wire bonding connections between the interposer pieces. Besides, it can be seen in Fig. 2.40 that the electric waves going through different paths arrive at the via connections at the same time which proves the phase balance among different signal traces.

For the proposed interposer, an alumina absorber layer is added between the MZM and the bottom aluminum carrier. In order to suppress parasitic modes efficiently, the absorber layer needs to be thick enough so that the couplings between the signal traces on the top of the interposer and the bottom ground plane can be minimized. Fig. 2.41 shows the simulated S-parameters of S1 when the alumina absorber layer has different thicknesses. By increasing the thickness of the absorber layer, the parasitic modes are restricted gradually and the transmission performance becomes acceptable when the thickness goes up to 1600 μm.

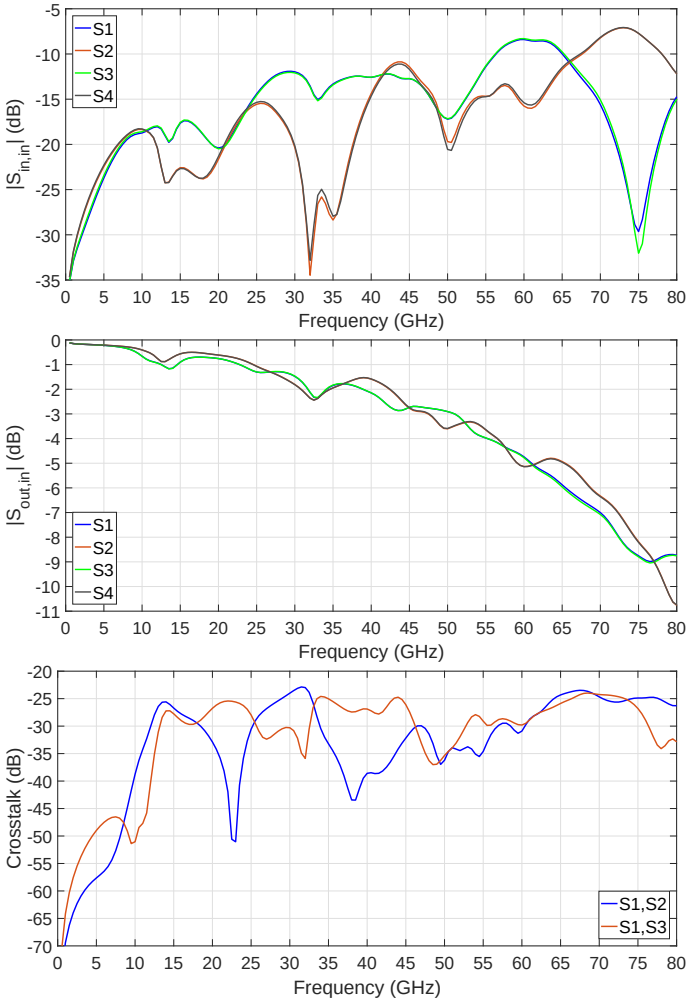

Figure 2.39: Simulation results of the interposer based on AlN substrate.

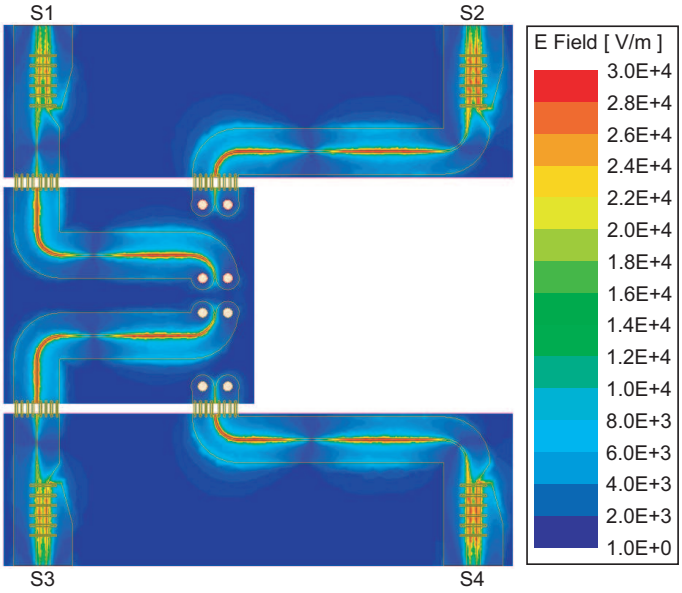

Figure 2.40: Electric field distributions of the interposer based on AlN substrate at 45 GHz.

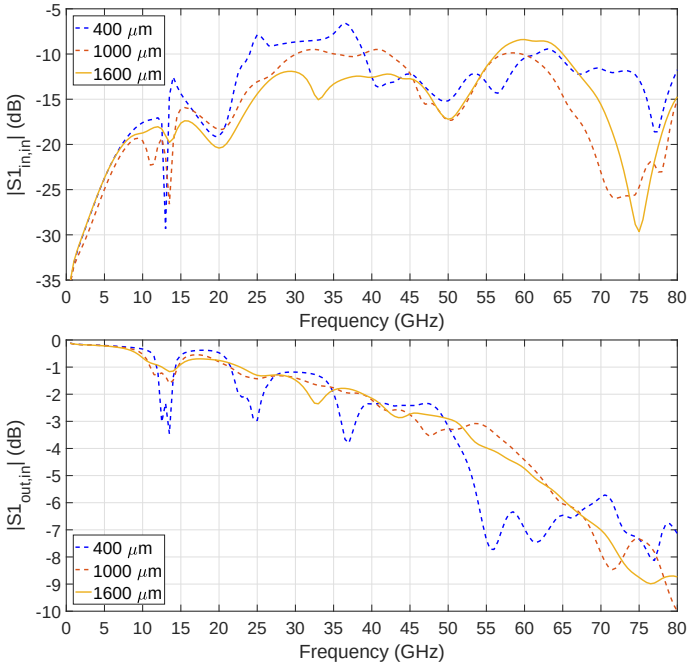

Figure 2.41: Simulation results of S1 when the alumina absorber layer has different thicknesses.

2.3 System Integration and Packaging

In order to have a foresight of the integration scheme, the co-simulations are normally carried out before the individual components being integrated into a system. The interposer based on AlN substrate has been introduced in Section 2.2 and the simulated eight-port S-parameters can be exported from ANSYS. Besides, the MZM based on InP substrate was fabricated and measured at Fraunhofer HHI. Due to the symmetry of the MZM layout, the two-port S-parameters were measured up to 67 GHz on one of the channels. Fig. 2.42 shows the schematic for the co-simulation which includes the interposer and the MZM. By importing the corresponding S-parameters into ADS and driving the schematic with four single-ended signals, the performance of the integrated system can be estimated. As is shown in Fig. 2.43, from DC to 45 GHz, the interposer together with the MZM exhibits an insertion loss of 10.3 dB and a return loss of 8 dB.

The DRVs, interposer, MZM, alumina absorber layer, and aluminum heat sink are integrated into a system by using wire bonding connections and hollow plated vias. The assembly of PANTHER terabit transmitter is based on the proposed 3D hybrid integration scheme and it is illustrated in Fig. 2.44. In order to compensate the thickness differences among different substrates for the system integration, several slots and platforms at different levels are reserved on the alumina absorber layer.

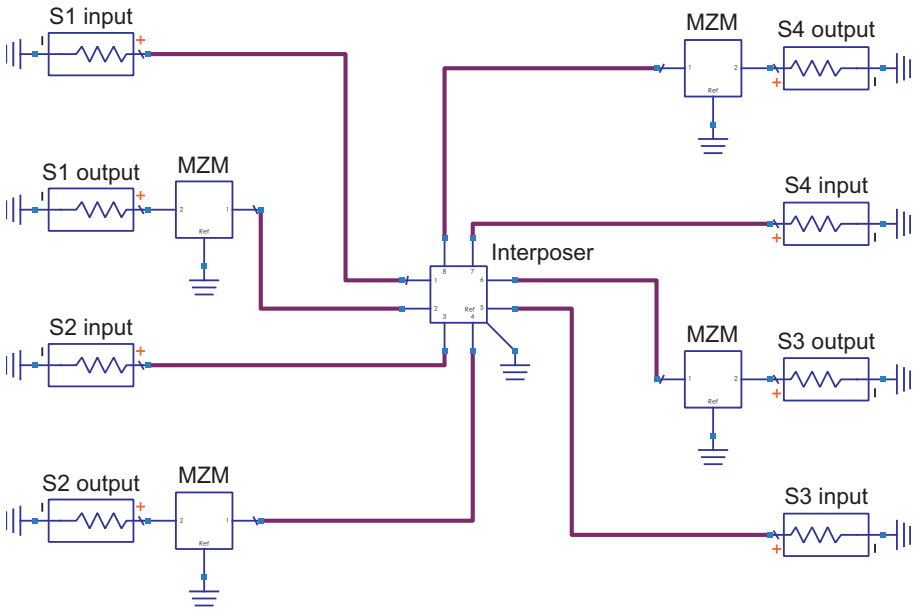

Figure 2.42: Schematic for the co-simulation.

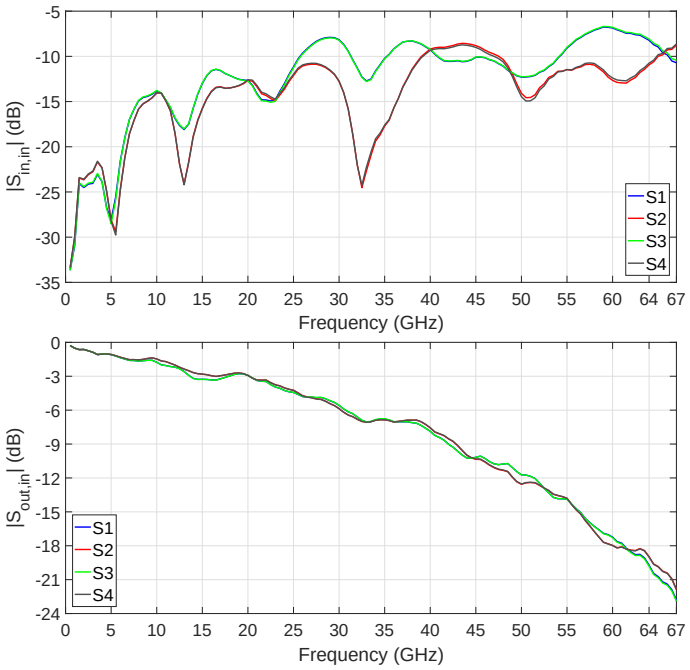

Figure 2.43: Co-simulation results of the integrated system.

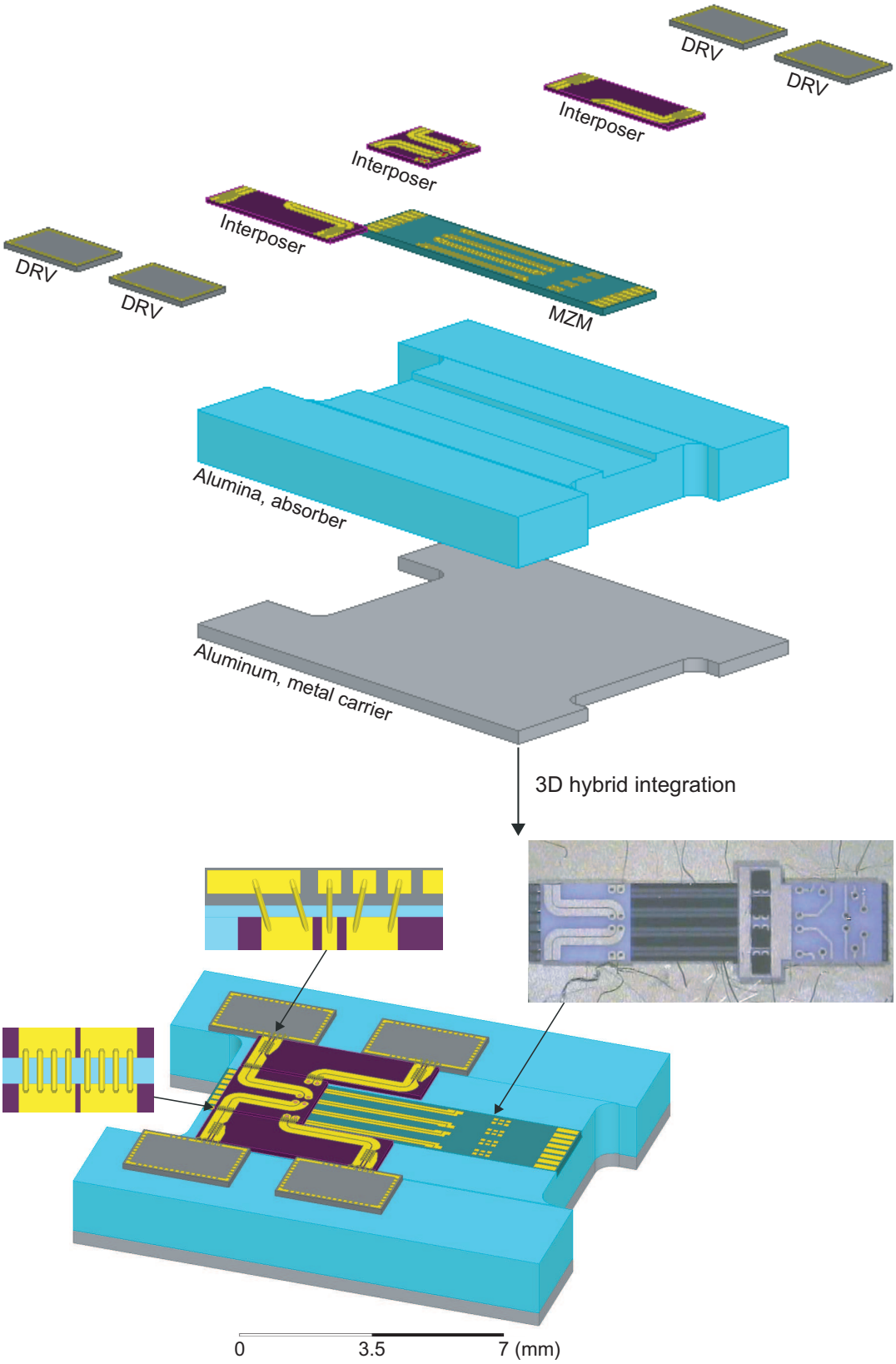

Figure 2.44: Assembly of PANTHER terabit transmitter.

2.4 Summary

The system integration and packaging of PANTHER terabit transmitter have been addressed in this chapter. As a part of the preliminary research, planar transmission lines including CPW and CPS based on thin AlN substrate have been presented at the beginning of this chapter. The structures, designs, simulation methods, performances, parasitic effects and the ways to suppress it have been discussed. Coplanar transitions are designed with the purpose of supporting data transmissions starting from DC and providing large bandwidths. For driving single-ended signals, a CPW-to-CPS transition using wire bonding bridges together with an alumina absorber layer and a CPW-to-ACPS transition using hollow plated vias going through the substrate have been designed, fabricated, and measured. The measurements were carried out by characterizing the transition prototypes on-wafer in a back-to-back configuration. The fabricated CPW-to-CPS transition using wire bonding bridges together with an absorber layer can provide a bandwidth of 80 GHz. When hollow plated vias are used for restricting the parasitic modes, the fabricated CPW-to-ACPS transition achieves a bandwidth of 165 GHz which has the largest bandwidth ranging from DC in comparison with other CPW-to-CPS and CPW-to-ACPS transitions in the literature.

At the end of this chapter, the 3D hybrid integration scheme of PANTHER terabit transmitter has been demonstrated. The components included in the system integration including the DRVs, MZM, and vertical via connections have been introduced individually in brief while the interposer based on AlN substrate has been explained in detail. By combining the proposed transmission lines, CPW-to-CPS transitions, wire bonding connections, and hollow plated vias, the designed interposer can support four single-ended signals at the same time and the signal traces have the same physical path lengths which keeps the phase balance among the transmitted signals. As a result, a simulated bandwidth of 47.5 GHz has been achieved and the crosstalk between different signal traces is below -20 dB. Besides, the thickness of the alumina absorber layer turns out to be 1600 μm which, according to the simulations, should be sufficient for suppressing the parasitic modes. The assembly of PANTHER terabit transmitter has been illustrated and the interposer is divided into three pieces for easier alignments. The co-simulation of the integrated system has been carried out by cascading the S-parameters of the components and the results have been presented.

CHAPTER 3

Rectangular Waveguide-to-Coplanar Waveguide Transitions

Apart from the planar transmission lines introduced in Chapter 2, rectangular waveguide is one of the widely used transmission lines for microwave systems at millimeter-wave and THz frequencies. The electromagnetic waves are guided inside a conductor tube which has a rectangular cross-section. Not only are rectangular waveguides one of the simplest types of transmission lines but also exhibit low-loss property and high power-handling capability within a wide range of frequencies. In general, rectangular waveguides are air-filled while other dielectric materials are also used especially for applications at low frequencies with the purpose of reducing the dimensions by a factor of $\sqrt{\epsilon_r}$. Unlike coaxial lines supporting TEM waves, rectangular waveguides can only propagate TE or TM modes since there is no conductor inside the rectangular tube. Due to the cutoff frequencies of TE and TM modes, the dimensions of rectangular waveguides are defined within each frequency band. For example, the width and height of an air-filled rectangular waveguide used for U-band (40-60 GHz) applications are 4.7752 mm (0.188") and 2.3876 mm (0.094"), respectively. The cutoff frequencies for such an U-band rectangular waveguide (WR-19) are 31.4 GHz for TE_{10} mode and 62.8 GHz for TE_{20} mode. With fixed dimensions for each frequency band, rectangular waveguides have become the standard interface for connecting or cascading different components and systems. At millimeter-wave and THz frequencies, rectangular waveguides are small in size and require accurate fabrication processes. On the one hand, by using spinners with smaller diameters, the traditional computer numerical control (CNC) milling process shows its advantages of high accuracy, stability, and repeatability for a wide range of materials. On the other hand, with continuous developments as well as improvements for new fabrication technologies, 3D printing has become a competitive candidate for fast prototyping or fabricating complicated structures with fine details. As for fabricating system packaging structures consisting of rectangular waveguides, one possible method is direct metal 3D printing process where metal powder is used to build the structure layer by layer while another method is using non-conductive material for 3D printing process and plating a conductor layer afterwards.

As is shown in Fig. 3.1, in order to figure out the possibility of using 3D printing process for system packaging at millimeter-wave and THz frequencies, a D-band (110-170 GHz) rectangular waveguide (WR-6.5) is designed which has a simple through structure with a length of 50.8 mm (2"). The width and height for a standard D-band rectangular waveguide are 1.651 mm (0.065") and 0.8255 mm (0.0325"), respectively. Besides, the standard rectangular waveguide flange with annular recess is also included in the design. For connecting two rectangular waveguides above V-band (50-75 GHz), at least one of the flanges needs to have annular recess in order to form a cover-to-choke connection which works as a quarter-wavelength transformer suppressing the wave leakage between two surfaces. The prototype is divided into two identical parts and printed using stereolithography (SLA) technology where liquid materials and composites are turned into solid cross-sections layer by layer, using an ultraviolet (UV) laser. After the 3D printing process, the prototype went through another process where a 5 μm nickel layer and a 15 μm copper layer were plated on the surfaces of the structures.

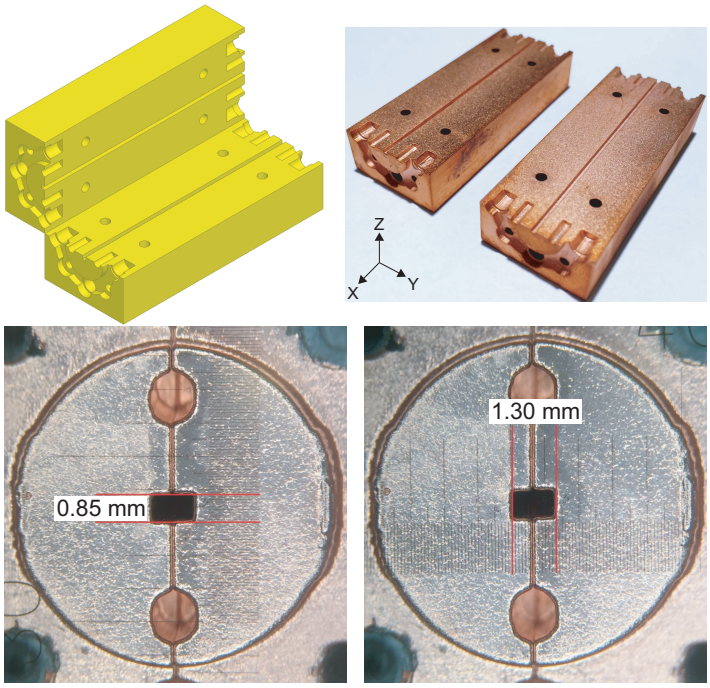

Figure 3.1: Design and fabrication of a D-band rectangular waveguide.

The fabricated D-band rectangular waveguide were measured under a microscope. The width and height are 1.30 mm and 0.85 mm, respectively. Due to the orientation of the 3D printing process, a higher accuracy has been achieved on the horizontal plane (xy-plane) instead of the vertical direction (z-axis) in which the structures are built layer by layer. The height difference between the designed rectangular waveguide and the fabricated prototype is within a tolerance of 50 μm while the width is around 0.35 mm shorter than the designed value which results in a shift of cutoff frequencies. Fig. 3.2 shows the measured S-parameters of the fabricated D-band rectangular waveguide using 3D printing and conductor plating processes. Except for the increased cutoff frequencies, the return loss of the fabricated rectangular waveguide remains better than 10 dB from

145 GHz to 170 GHz with an associated insertion loss of 1 dB. As a consequence, by taking into account the uncertainties caused by the 3D printing process, a traditional CNC milling process is selected to fabricate the packaging structures of the proposed rectangular waveguide-to-coplanar waveguide (CPW) transitions in this chapter.

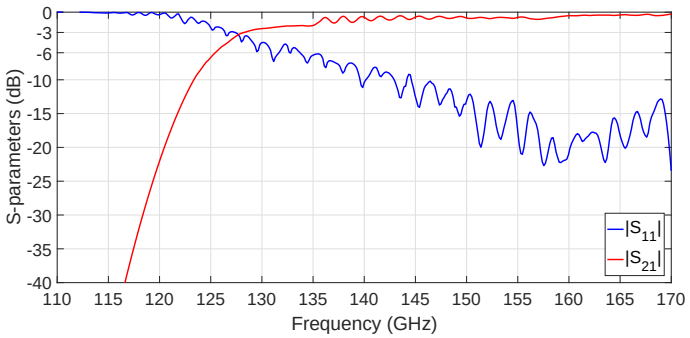

Figure 3.2: Measurement results of the fabricated D-band rectangular waveguide.

Though rectangular waveguide has become an essential part for system packaging at millimeter-wave and THz frequencies, the circuits as well as chips at such high frequencies still rely on planar structures due to their fabrication processes. Under this circumstance, the transitions between rectangular waveguides and planar transmission lines in particular CPW are under intensive study. This chapter presents the designs of rectangular waveguide-to-CPW transitions realized by different methods. The substrate used for designing the transitions is discussed at the beginning. In order to acquire the information of substrate properties at high frequencies, investigate the possibilities of in-house chip fabrications, and test measurement facilities, a CPW is designed at the beginning of this chapter. The CPW is patterned on both glass and quartz substrates and the measurement results are compared. After that, the proposed rectangular waveguide-to-CPW transitions at U-band are introduced. Two transition prototypes at U-band using E-plane probe and wire bonding probe are fabricated and measured. Besides, for system packaging at higher frequencies, the proposed rectangular waveguide-to-CPW transitions at D-band using E-plane probe, wire bonding probe, and wideband patch antenna are described. Three transition prototypes at D-band are fabricated and measured. For both U-band and D-band transition prototypes, the measurement results are compared with the simulation results and the performances among different methods are discussed. At the end of this chapter, the potential system packaging approaches at D-band based on the proposed transitions using different methods are demonstrated.

3.1 Substrate for Designing Transitions

When designing rectangular waveguide-to-CPW transitions at millimeter-wave and THz frequencies it is necessary to have the information of substrate properties at such high frequencies in particular the dielectric constant (ϵ_r) and dissipation factor (tanδ) which vary with frequency and are commonly measured by the supplier at low frequencies. Sometimes, the information is even not provided by the substrate suppliers since microwave integrated circuits (MICs) may not be their

main application field. In these cases, a simple prototype which contains a small piece of straight transmission line such as CPW or microstrip line (MSL) based on the selected substrate can be used for testing its performance at the expected operating frequencies.

Fig. 3.3 shows the structure of a CPW based on silicon dioxide (SiO_2) substrate with a thickness of 150 μm which, according to [60], is one of the commonly used substrate materials for designing waveguide transitions at millimeter-wave and THz frequencies. The ϵ_r and tanδ of the SiO_2 substrate are around 4 and 1.5e-5, respectively, which are measured at 1 MHz. The width of the signal trace is 100 μm and the width of the ground traces is 300 μm with a gap of 30 μm. The SiO_2 substrate has a width of 2000 μm and a length of 5000 μm. In the simulation, lumped ports with vertical perfect electric conductor (PEC) bridges are used as the excitation scheme where the PEC bridges are selected to be the reference. The lumped port has a width of 100 μm and a height of 50 μm. The parasitic sheet inductance is calculated and subtracted from the simulation results by post processing at the ports. Besides, for more realistic situations, a bottom ground plane under the substrate and an air cavity with radiation boundary conditions on the top of the substrate are also included in the simulation.

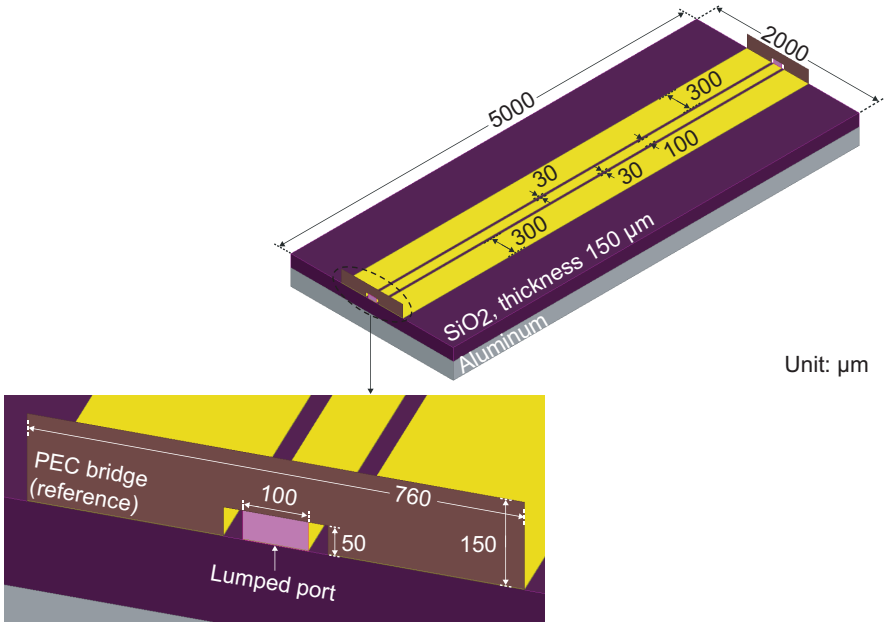

Figure 3.3: CPW based on SiO_2 substrate and the port excitation scheme used for simulations.

The simulated S-parameters of the CPW based on SiO_2 substrate at D-band are shown in Fig. 3.4. Since the CPW is mainly designed for validating the substrate properties and testing the in-house fabrication processes, it is not suppose to be a 50 Ω transmission line. The return loss is better than 7.7 dB from 110 GHz to 170 GHz and the insertion loss is less than 2.4 dB. Besides, Fig. 3.4 shows the simulated maximum insertion loss of the CPW at D-band in terms of the tanδ of the SiO_2 substrate. By solely increasing the tanδ from 1.5e-5 to 5e-2, the insertion loss of the designed CPW at D-band goes up to around 5 dB. Furthermore, it explains the necessity of choosing substrate materials with low tanδ at millimeter-wave and THz frequencies.

As is shown in Fig. 3.5, two CPW prototypes were fabricated in-house which are based on

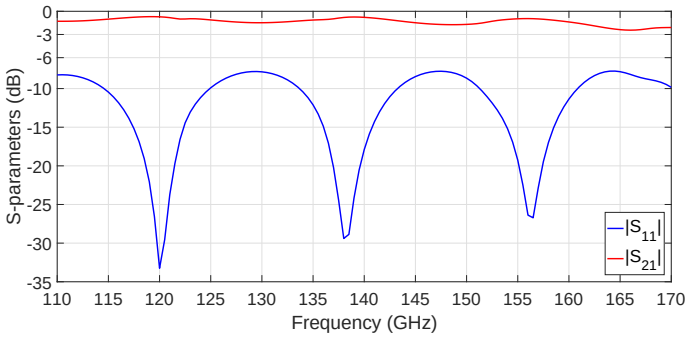

(a) S-parameters.

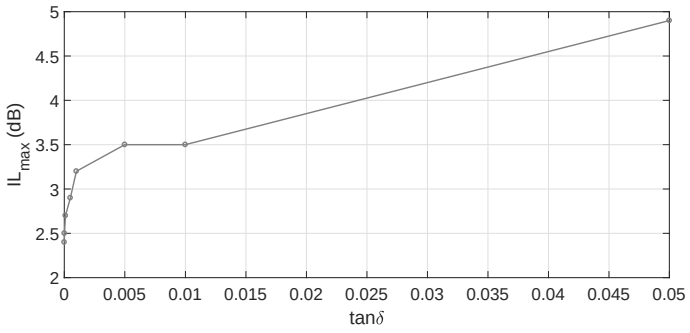

(b) Maximum insertion loss (IL).

Figure 3.4: Simulation results of the CPW based on SiO_2 substrate.

glass and quartz substrates with a thickness of 150 μm. The quartz substrate (CFQ-2557) from UQG Optics is selected to be used and the tolerance of the substrate thickness is 20 μm. Though SiO_2 is the major ingredient for both glass and quartz substrates, they contain different percentages of impurities which affects the tanδ especially at high frequencies. The conductor layer has a thickness of 400 nm and it was deposited using gold sputtering at Danchip (National Center for Micro- and Nanofabrication in Denmark). In order to improve the adhesion of the gold conductor, a titanium layer with a thickness of 30 nm was deposited first on top of the substrates. Then the CPW was patterned by laser ablation using a picosecond laser with a wavelength of 355 nm focused down to a spot size of approximate 10 μm. After patterning, the substrates were cut into pieces by using a dicing saw. The measured dimensions of the fabricated prototype under a microscope are also shown in Fig. 3.5. A good agreement between the design and the fabricated prototype has been achieved which validates the in-house fabrication processes and proves its accuracy.

The measurement results of the fabricated CPWs at D-band are shown in Fig. 3.6. In comparison with the simulation results (blue dashed lines), the fabricated CPW based on quartz substrate (green solid lines) achieves a reasonable agreement while the fabricated CPW based on glass substrate (red solid lines) shows a higher insertion loss due to the increasing of tanδ at high frequencies. The CPW based on quartz substrate exhibits an insertion loss of 0.4 dB/mm at 170 GHz while it is 1.3 dB/mm for the CPW based on glass substrate. As a result, the properties of quartz substrate have been validated up to 170 GHz, thus it is used for fabricating the proposed rectangular waveguide-to-CPW transitions in this chapter.

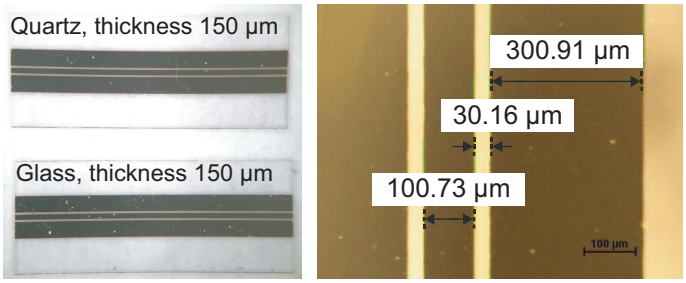

Figure 3.5: Fabricated CPWs based on glass and quartz substrates.

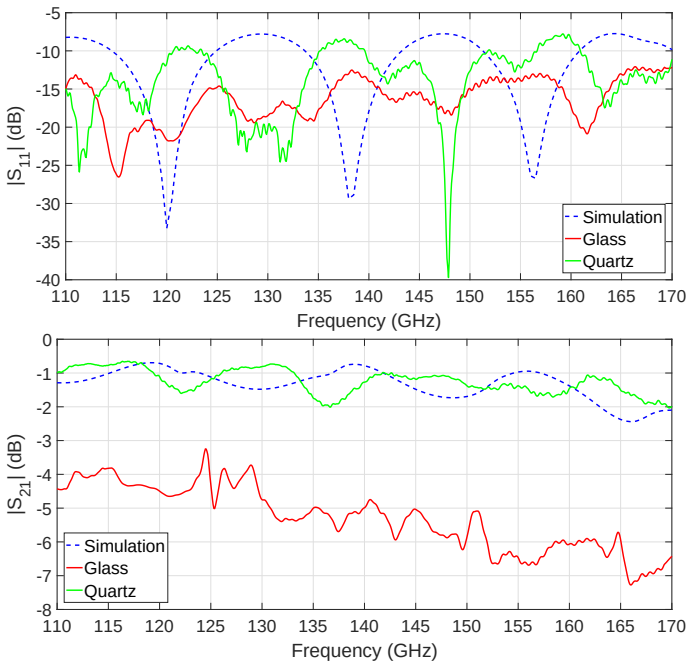

Figure 3.6: Measurement results of the CPWs based on glass and quartz substrates.

3.2 U-Band Rectangular Waveguide-to-Coplanar Waveguide Transitions

Fig. 3.7 shows the overview of the proposed rectangular waveguide-to-CPW transitions at U-band. By inserting the E-plane probe or wire bonding probe into a rectangular waveguide through an aperture cut in the broadwall parallel to the longitudinal axis, electromagnetic waves are guided from the U-band rectangular waveguide to the CPW connected to the probe. The E-plane probe is a rectangular patch patterned on the substrate which is connected to the signal trace of the CPW. By changing the width and length of the rectangular patch, the E-plane probe can be adjusted to different frequency bands. Besides, a wire bonding between the signal trace of the CPW and a small square pad patterned on the substrate also works as a probe. The operating frequencies of the wire bonding probe can be adjusted by changing the length and shape. In both cases, the inserted probe is placed around a quarter wavelength away from the end of the rectangular waveguide which forms an impedance transformer converting the termination from short to open.

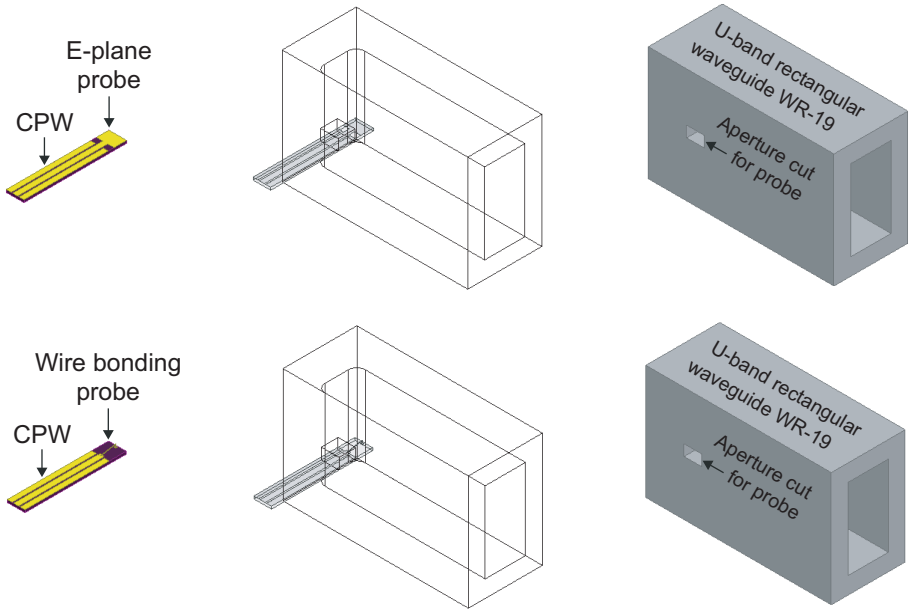

Figure 3.7: Overview of rectangular waveguide-to-CPW transitions at U-band (see Fig. 3.10 and Fig. 3.14 for detailed views).

3.2.1 Coplanar Waveguide Packaged Inside an Aluminum Cover

For system integration and packaging at millimeter-wave and THz frequencies, the environment conditions are normally changed from free space to a closed cavity when the circuits and chips are packaged inside a metal cover together with the rectangular waveguides. Fig. 3.8 shows the structure when a CPW is packaged inside an aluminum cover which results in new boundary conditions as well as dimension variations. The CPW is based on a quartz substrate with a thickness of 150 μm and it is firstly designed for operating at U-band with an environment condition of free space. In order to keep a characteristic impedance of 50 Ω, the width of the signal trace is optimized to be 300 μm with a gap of 85 μm. The vertical sidewalls of the aluminum cover work similar as the vias going through a thin substrate which have been introduced in Section 2.1.1. It helps to restrict the parasitic modes of the conductor-backed CPW based on the quartz substrate, thus the width of the ground traces is reduced to 290 μm which results in a width of 1050 μm for the quartz substrate. The air cavity for fitting the CPW has a height of 650 μm and its width is represented by CW. When the width of the air cavity is the same as the width of the substrate, the ground traces touch the sidewalls of the aluminum cover providing ground connections to the packaged CPW otherwise the ground traces are floating and might cause resonances. In the simulation, the length of the packaged CPW is set to 5 mm and wave ports are used as the excitation scheme. In order to generate the port field correctly, the wave port touches the ground traces by its vertical edges and the aluminum cover by its horizontal edges. The width and height of the wave port are 905 μm and 650 μm, respectively.

Fig. 3.9 shows the simulation results of the packaged CPW at U-band with different CW values. When CW equals 1050 μm, there is no gap between the aluminum cover and the substrate.

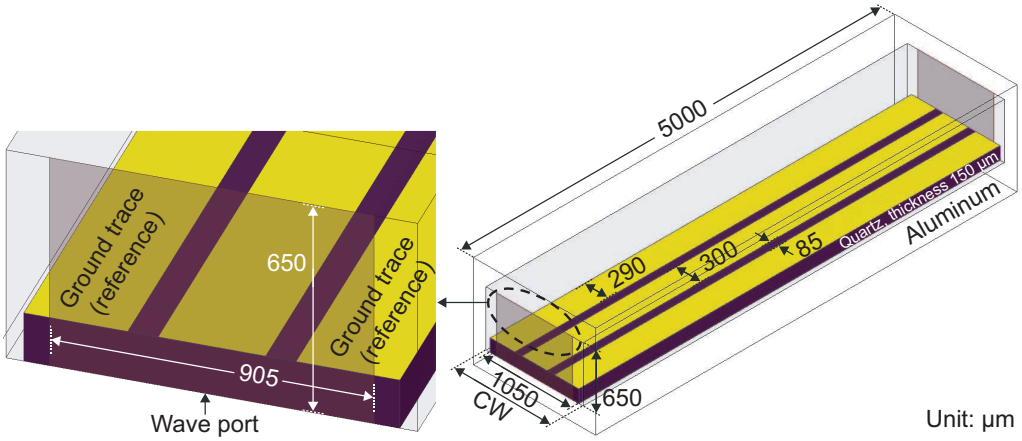

Figure 3.8: CPW packaged inside an aluminum cover at U-band and the port excitation scheme used for simulations.

The packaged CPW shows a smooth transmission from 40 GHz to 60 GHz where the return loss remains better than 20 dB and the insertion loss is less than 0.3 dB. However, because of the floating ground traces, the notches appear when the air cavity is wider than the substrate. For easier alignment and system packaging, the width of the air cavity, as fabricated by milling process, is normally slightly larger than the width of the diced substrate. Under this circumstance, silver conductive glue is needed for filling the gaps between the aluminum cover and the substrate as well as providing ground connections to the packaged CPW.

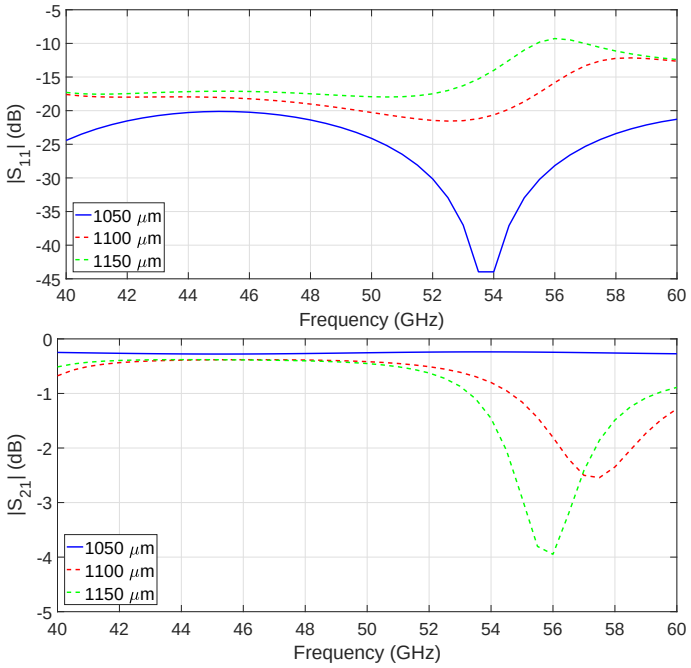

Figure 3.9: Simulation results of the packaged CPW at U-band with different CW values.

3.2.2 Transition Using E-plane Probe

As is shown in Fig. 3.10, a rectangular waveguide-to-CPW transition at U-band using E-plane probe is designed. Since E-plane probe has been widely used for designing transitions between rectangular waveguides and CPWs as well as MSLs, it works as a reference showing the performance of the transition using the existing technology. For the proposed transition at U-band using E-plane probe, a rectangular patch is inserted into a WR-19 rectangular waveguide through an aperture. The E-plane probe and the CPW are based on the same quartz substrate. The material of the conductor layer is gold and it has a thickness of 400 nm which is more than the skin depth calculated at U-band. The width and length of the rectangular patch are 1050 μm and 740 μm, respectively. By changing the dimensions of the rectangular patch, the E-plane probe can be adjusted to different frequency bands. In order to connect the packaged CPW to the rectangular patch, the signal trace is extended with a length of 340 μm. The distance between the center of the rectangular patch and the end of the rectangular waveguide is 1800 μm which works as a quarter-wavelength impedance transformer. Due to the milling process the corners at the end of the rectangular waveguide are rounded with a radius of 500 μm. Fig. 3.10 also shows the packaging structure of the proposed transition at U-band which is designed in a back-to-back configuration with the purposes of easier simulation, fabrication, and measurement. The packaging structure consists of two WR-19 rectangular waveguides with a length of 5 cm, a packaged CPW in the middle with a length of 2 cm, and two E-plane probe transitions. In the simulation, wave ports are used as the excitation scheme and they are assigned to the surfaces of the rectangular waveguides which are located at the input and output of the packaging structure. Besides, the proposed transition at U-band are simulated with different conductor thicknesses in order to investigate the skin effect.

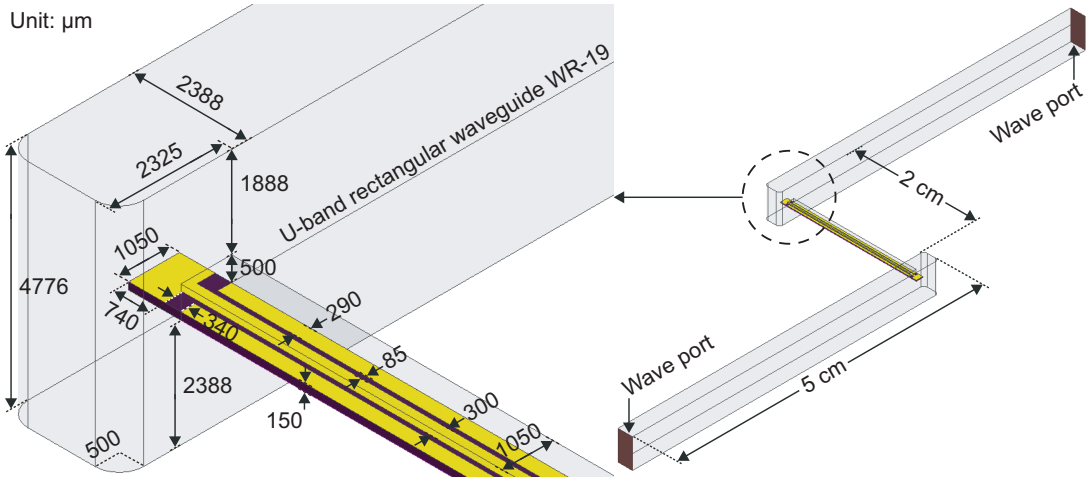

Figure 3.10: Rectangular waveguide-to-CPW transition at U-band using E-plane probe.

The simulation results of the rectangular waveguide-to-CPW transition at U-band using E-plane probe are shown in Fig. 3.11. The proposed transition using E-plane probe exhibits a smooth transmission with low insertion loss. The simulated return loss is better than 13.8 dB with an associated return loss of 1.5 dB from 40 GHz to 60 GHz. Howerver, with a thicker conductor layer,

the proposed transition shows a slightly better performance where the return loss remains the same level and the insertion loss is less than 1 dB at U-band.

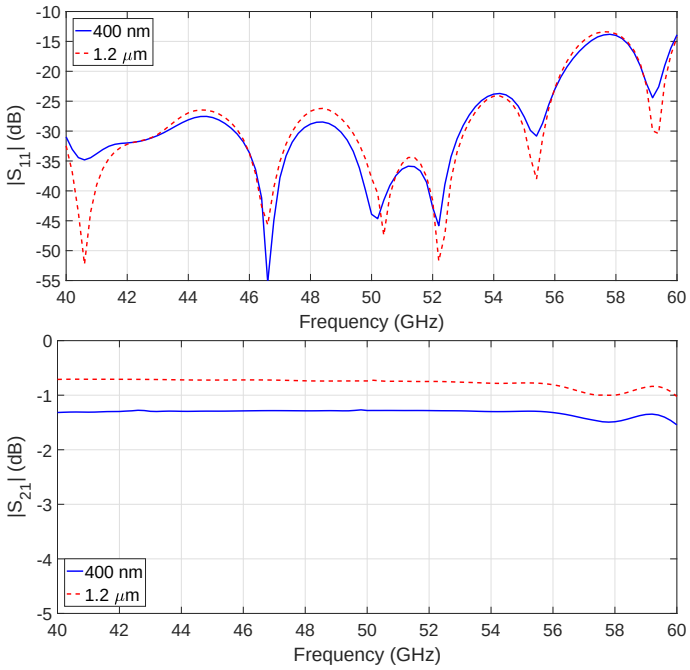

Figure 3.11: Simulation results of the rectangular waveguide-to-CPW transition at U-band using E-plane probe with different conductor thicknesses.

The rectangular waveguide-to-CPW transition at U-band using E-plane probe shown in Fig. 3.10 was fabricated. For easier fabrication and substrate alignment, the packaging structure was divided into two parts and each part was fabricated using an aluminum block by milling process. The bottom structure contains half of the input and output WR-19 rectangular waveguides and a recess in the middle with a depth of 150 μm which is used for fitting the quartz substrate. For the top structure, except for the rest half of the WR-19 rectangular waveguides, a 500 μm deep recess was milled in the middle and it works as the air cavity above the packaged CPW. Two guide pins and eight screws are used for accurate assembly. Besides, two standard WR-19 rectangular waveguide flanges were fabricated at the input and output of the packaging structure. The quartz substrate was ordered from UQG Optics and then the E-plane probe together with the CPW were fabricated at Danchip. The fabrication processes have been validated by the fabricated CPW prototypes. The thickness of the gold conductor layer is 400 nm with an extra titanium conductor layer underneath with a thickness of 30 nm. The patterning process was done by laser ablation using a picosecond laser and several identical samples were patterned on the same substrate. The width and length of each sample are 1.05 mm and 22.16 mm, respectively. Since the quartz substrate is fragile and the sample has a high length-to-width ratio, the patterned substrate was sticked to a silicon wafer and they were cut together using a dicing saw in order to overcome the stress during the process. Fig. 3.12 shows the fabricated packaging structure as well as the diced quartz substrate. The substrate was aligned inside the recess on the bottom structure where the depth of the recess is the same as the thickness of the substrate. The gaps between the substrate and the recess were

filled with silver conductive glue which not only restricts the parasitic modes by providing ground connections to the packaged CPW but also helps the quartz substrate to be fixed in the recess physically.

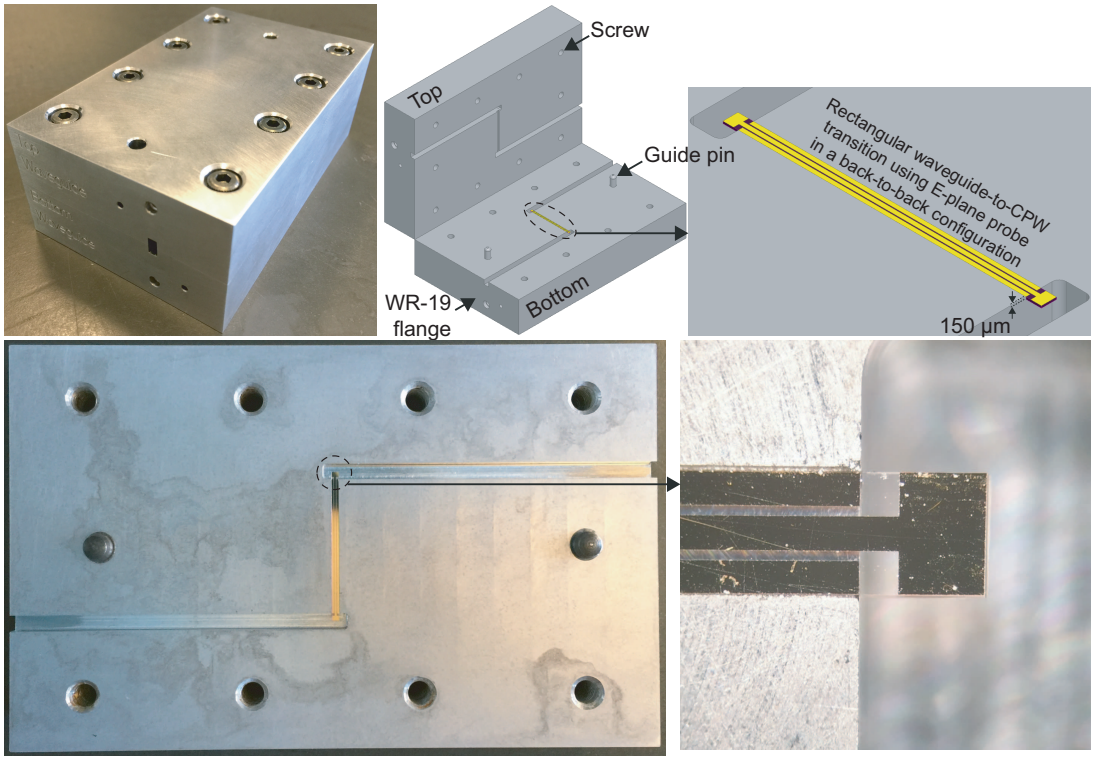

Figure 3.12: Fabricated rectangular waveguide-to-CPW transition at U-band using E-plane probe in a back-to-back configuration.

The measurement system comprises an Agilent E8361A vector network analyzer (VNA) and two rectangular waveguide-to-coax adapters (24094-VF50) from Flann Microwave which can measure two-port S-parameters from 40 GHz to 60 GHz. In order to improve the accuracy, an Agilent U11644A waveguide calibration kit was used for calibrating out the effects of the cables and adapters. Fig. 3.13 shows the measurement results (red solid lines) of the fabricated rectangular waveguide-to-CPW transition at U-band using E-plane probe in a back-to-back configuration. Compared with the simulation results (blue dashed lines), a reasonable agreement has been achieved. Since the bandwidth of the transition refers to the width of the frequency band where the return loss is better than 10 dB, the fabricated transition prototype at U-band exhibits a bandwidth of 18 GHz ranging from 40 GHz to 58 GHz with an associated insertion loss of 3 dB. The differences between the measurement and simulation results are mainly caused by the tolerance of fabrication, the ground connections between the CPW and the packaging structure, and the assembly between the top and bottom parts.

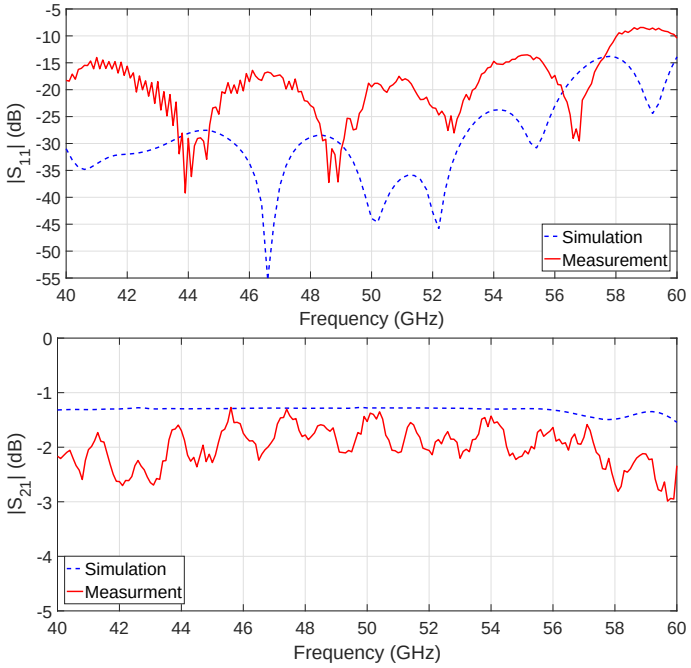

Figure 3.13: Measurement results of the fabricated rectangular waveguide-to-CPW transition at U-band using E-plane probe in a back-to-back configuration.

3.2.3 Transition Using Wire Bonding Probe

Though wire bondings have been widely used as bridges and chip-level connections between different components and circuits, it introduces significant parasitic inductances especially at millimeter-wave and THz frequencies which as a result, limits its usage. Fig. 3.14 demonstrates a novel method for realizing rectangular waveguide-to-CPW transition at U-band in which the wire bonding itself works as a probe guiding electromagnetic waves from the rectangular waveguide to the CPW. Instead of the rectangular patch used as the E-plane probe, a wire bonding is inserted into a WR-19 rectangular waveguide through an aperture. There is a small square pad patterned at the end of the substrate which is used for not only controlling the length of the wire bonding but also increasing the surface adhesion so that the wire bonding can start or terminate at a specific point on the substrate. By changing either the length or the shape, the wire bonding probe can be adjusted to different frequency bands. For the proposed transition at U-band, the square pad has a length of 100 μm and it locates 50 μm away from the edge of the substrate. Besides, the signal trace of the packaged CPW is extended with a length of 100 μm and a width of 240 μm which are optimized for connecting the wire bonding probe. By taking into account the fabrication process, the wire bonding probe goes from the small pad on the substrate to the extended signal trace of the packaged CPW. Fig. 3.14 also shows the packaging structure of the proposed transition at U-band in which the rectangular waveguides and the packaged CPW are the same as those used for the E-plane probe transition in Fig. 3.10. In this way, the performances of the proposed transitions at U-band can be compared since the packaging structure used for the E-plane probe is reused for the wire bonding probe. In the simulation, wave ports are used as the excitation scheme and the same

settings are applied.

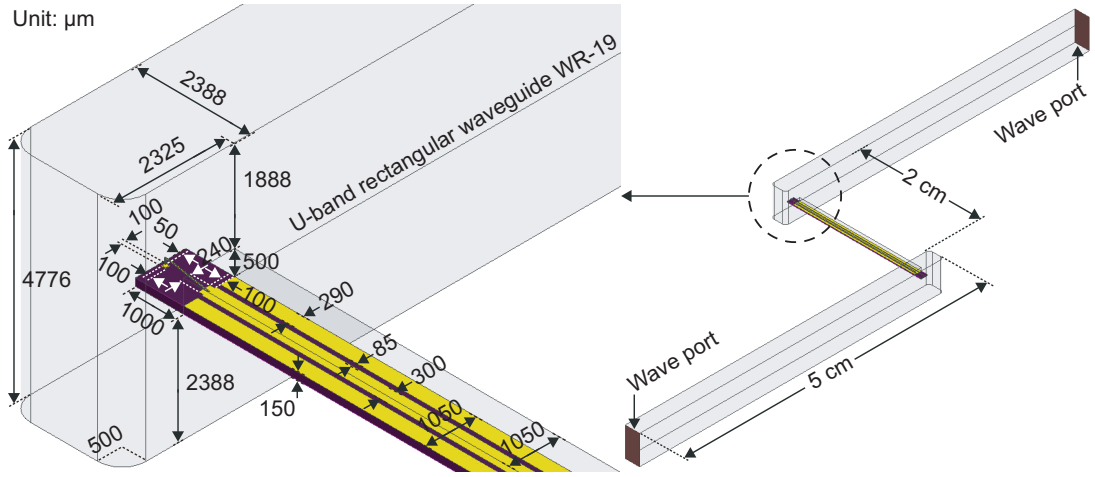

Figure 3.14: Rectangular waveguide-to-CPW transition at U-band using wire bonding probe.

During the fabrication process of the wire bonding probe, a high-voltage spark is generated at the terminal of the wire bonding which results in a conductor ball. After that the conductor ball is soldered and pressed at the start point on the substrate. Then the wire bonding is pulled up to a specific height and moved to the termination point. At the end, the fabricated wire bonding probe has a nature slope whose shape is mainly determined by the height of the wire bonding. For advanced wire bonders, more complex shapes can be specified and realized. In order to fix the wire bonding probe on the substrate, the start and termination points must locate at conductor area. For the proposed transition at U-band, the wire bonding probe starts at the square pad and terminates at the extended signal trace of the packaged CPW. Fig. 3.15 illustrates the details of the modeled wire bonding probe at U-band. The wire bonding has a diameter of 25 μm and the material is gold. The diameter of the conductor ball at the start point is 80 μm. The wire bonding has a fixed length of 850 μm which is the distance from the square pad to the extended signal trace. By solely changing the height, the wire bonding probe can have different shapes which corresponds to different occupation area in the vertical plane and results in a shift of operating frequency. In order to investigate the performance sensitivity against the shape variation, the proposed transition at U-band using wire bonding probe is simulated with different shapes.

Fig. 3.16 shows the simulation results of the rectangular waveguide-to-CPW transition at U-band using wire bonding probe with different shapes. Since the bandwidth of the proposed transition at U-band using wire bonding probe can not cover the whole frequency band, it becomes important to make sure that the operating frequency of the packaged circuit locates inside the frequency range of the proposed transition. When the height of the wire bonding probe is 300 μm, the proposed transition exhibits a bandwidth of 9 GHz ranging from 41 GHz to 50 GHz with an associated insertion loss of 2.2 dB. For the wire bonding probe with a height of 50 μm, a bandwidth of 6.5 GHz is achieved from 53.5 GHz to 60 GHz and the insertion loss is less than 2 dB.

The rectangular waveguide-to-CPW transition at U-band using wire bonding probe shown in Fig. 3.14 was fabricated. The fabrication follows the same processes of gold sputtering, patterning,

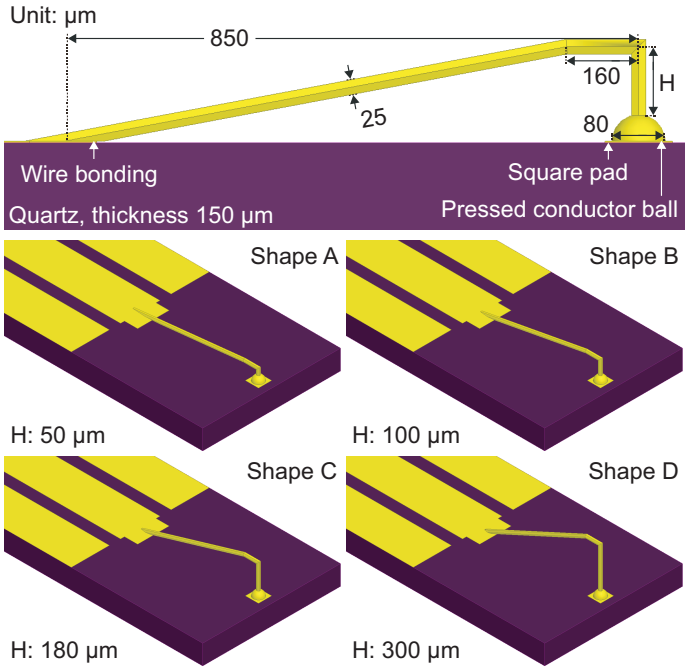

Figure 3.15: Different shapes of the wire bonding probe at U-band.

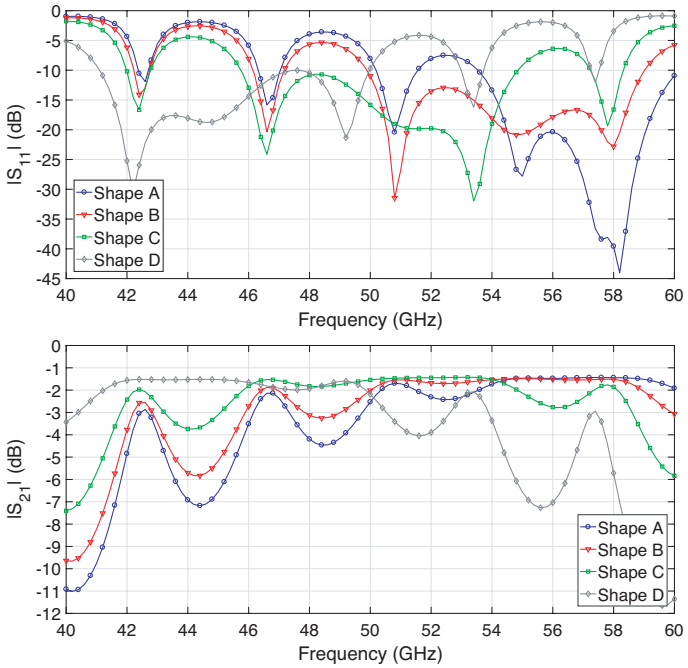

Figure 3.16: Simulation results of the rectangular waveguide-to-CPW transition at U-band using wire bonding probe with different shapes.

and dicing. The width and length of each diced sample are 1.05 mm and 22 mm, respectively. Besides, the wire bonding probes were made at the last step for the diced samples. Since the fabricated aluminum packaging structure for the proposed transition at U-band using E-plane probe was reused for the proposed transition at U-band using wire bonding probe, it was cleaned by acetone which works as the solvent for dissolving the silver conductive glue in the gaps and the substrate was replaced after that. Fig. 3.17 shows the reused packaging structure and the diced substrate with wire bonding. For restricting the parasitic modes and fixing the newly aligned substrate physically, the gaps between the substrate and the recess were also filled with silver conductive glue.

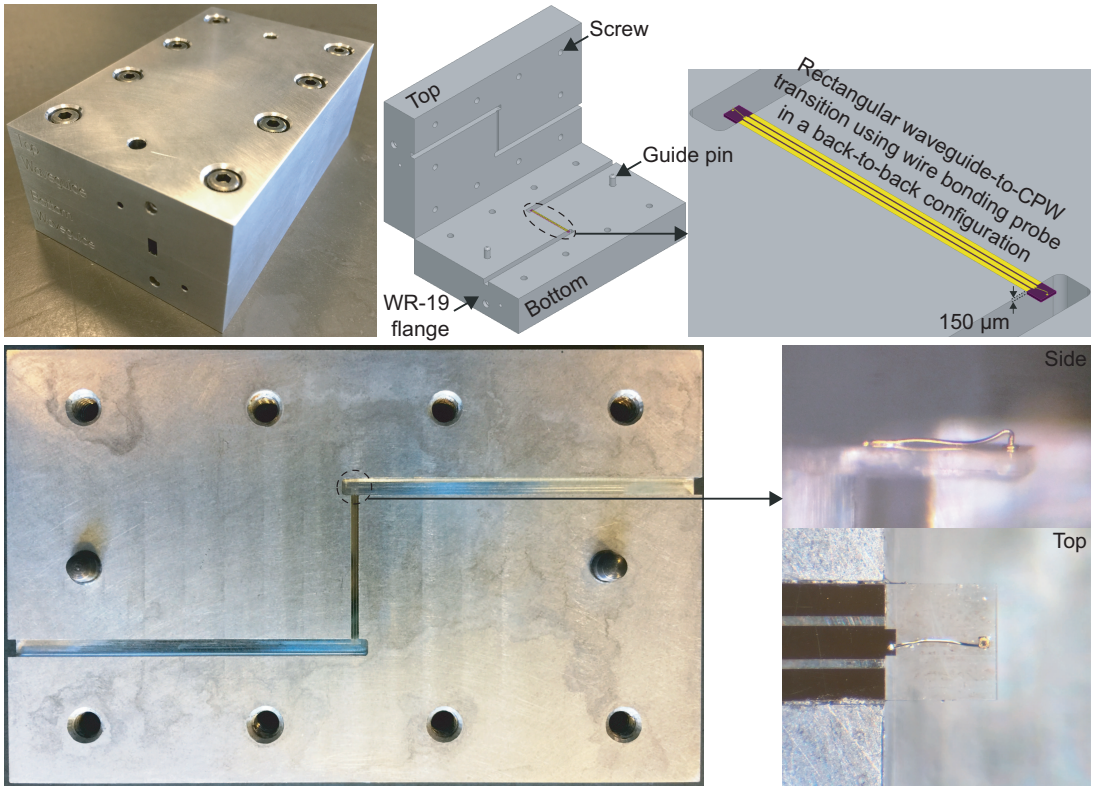

Figure 3.17: Fabricated rectangular waveguide-to-CPW transition at U-band using wire bonding probe in a back-to-back configuration.

The same measurement system including the waveguide calibration kit at U-band was used. The red solid lines in Fig. 3.18 are the measurement results of the fabricated rectangular waveguide-to-CPW transition at U-band using wire bonding probe in a back-to-back configuration while the blue dashed lines correspond to the simulation results when the height of the wire bonding probe is 100 μm. The fabricated transition prototype at U-band achieves a bandwidth of 11 GHz ranging from 49 GHz to 60 GHz with an associated insertion loss of 3 dB. The differences between the measurement and simulation results are mainly caused by the shape of the wire bonding probe.

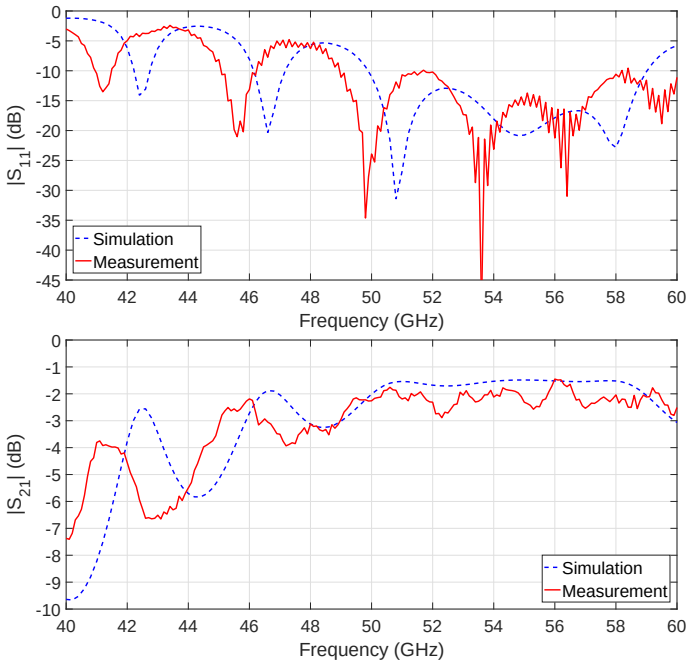

Figure 3.18: Measurement results of the fabricated rectangular waveguide-to-CPW transition at U-band using wire bonding probe in a back-to-back configuration.

3.3 D-Band Rectangular Waveguide-to-Coplanar Waveguide Transitions

Fig. 3.19 shows the overview of the proposed rectangular waveguide-to-CPW transitions at D-band. In order to prove the possibilities and compare the performances of using E-plane probe and wire bonding probe for the rectangular waveguide-to-CPW transitions at higher frequencies, two transition prototypes at D-band are designed in which the E-plane probe and wire bonding probe are adjusted to D-band together with the optimized CPW and aluminum packaging structure. Though the concepts are similar, the components and circuits at higher frequencies have smaller feature sizes which not only challenge the fabrication processes but also suffer from the parasitic effects. Except for using E-plane probe and wire bonding probe, a rectangular waveguide-to-CPW transition at D-band using wideband patch antenna is also proposed. For the proposed transitions using E-plane probe and wire bonding probe, the substrate is inserted into the rectangular waveguide around a quarter wavelength away from the end forming an impedance transformer converting the termination from short to open. However, for the proposed transition using wideband patch antenna, the substrate is placed inside a cavity at the end of the rectangular waveguide where the electromagnetic waves are guided from the CPW to the rectangular waveguide in the direction of maximum radiation.

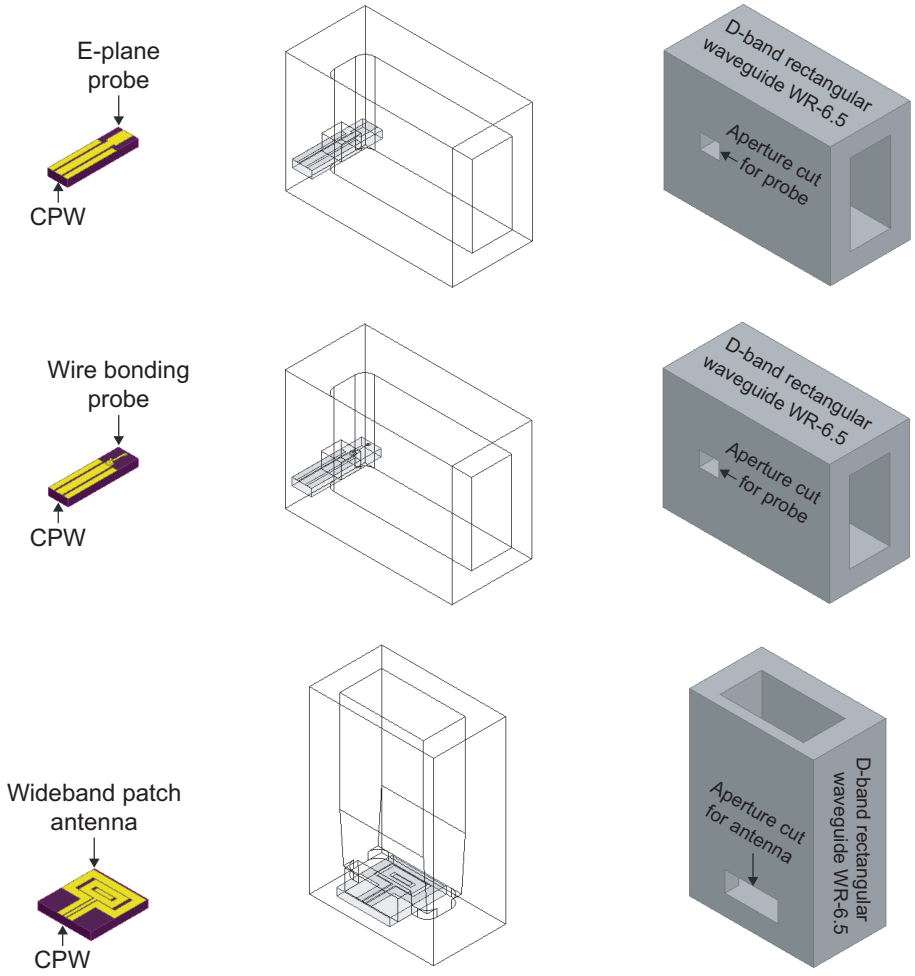

Figure 3.19: Overview of rectangular waveguide-to-CPW transitions at D-band (see Fig. 3.22, Fig. 3.27, and Fig. 3.34 for detailed views).

3.3.1 Coplanar Waveguide Packaged Inside an Aluminum Cover

The CPW shown in Fig. 3.20 is packaged inside an aluminum cover and it is designed as the connection between the chip and the transition which operates at D-band. For system packaging, the chips are normally placed in a large cavity with two apertures on both sides for connecting to the transitions. The width of the packaged CPW or MSL is kept small in order to restrict parasitic modes and provide isolation for the chip [27], [47], [63], [64]. The quartz substrate has a thickness of 150 μm and the characteristic impedance of the packaged CPW is designed to be 50 Ω at D-band. Since the dimensions of the air cavity are reduced in order to restrict parasitic modes, the packaged CPW is optimized for a more compact structure. The width of the signal trace reduces to 135 μm and the width of the ground traces reduces to 97.5 μm with a gap of 35 μm. As a result, the quartz substrate has a width of 400 μm and it is placed inside the air cavity where the height is 310 μm and the width is represented by CW. When the width of the air cavity is the same as the width of the quartz substrate, the ground traces touch the sidewalls of the aluminum cover providing ground connections to the packaged CPW otherwise the ground traces are floating and might cause

resonances. In the simulation, the packaged CPW has a length of 5 mm and wave ports are used as the excitation scheme. The width and height of the wave port are 352 μm and 310 μm, respective.

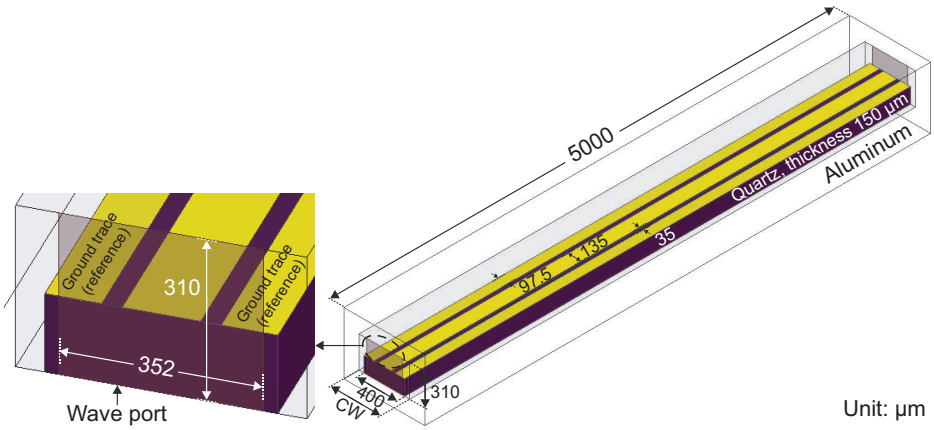

Figure 3.20: CPW packaged inside an aluminum cover at D-band and the port excitation scheme used for simulations.

The packaged CPW at D-band is simulated with different CW values and the results are shown in Fig. 3.21. When CW equals 400 μm, the ground traces of the packaged CPW touch the aluminum cover. In this case, for the packaged CPW from 110 GHz to 170 GHz, the return loss is better than 18 dB and the insertion loss is less than 0.6 dB. Compared with the packaged CPW at U-band with the same physical length, a similar performance is achieved. When there are gaps between the aluminum cover and the substrate, the notches appear and degrade the performance of the CPW. Besides, since the packaged CPW at D-band has a longer electrical length, the simulation results exhibit several notches periodically in the frequency band. For system packaging at D-band, due to the milling process and substrate alignment, the width of the air cavity is slightly larger than the width of the diced substrate. As a result, silver conductive glue is used to fill the gaps and provide ground connections to the packaged CPW.

3.3.2 Transition Using E-plane Probe

The proposed rectangular waveguide-to-CPW transition at D-band using E-plane probe is illustrated in Fig. 3.22 and it is designed to be a reference showing the performance of the transition using the existing technology. The E-plane probe is realized by a rectangular patch which is patterned at the end of the substrate and inserted into a WR-6.5 rectangular waveguide through an aperture. The quartz substrate as well as the gold conductor layer are the same as those used for the proposed transitions at U-band. When the operating frequency increases from U-band to D-band, the width and length of the rectangular patch are reduced to 200 μm and 350 μm, respectively. In order to connect the packaged CPW to the rectangular patch and achieve a wideband matching, the signal trace is extended with a length of 85 μm and a width of 120 μm. The designed E-plane probe locates 540 μm away from the end of the rectangular waveguide which works as a quarter-wavelength impedance transformer. Since the packaging structure is fabricated by milling process, the round corners at the end of the rectangular waveguide have a radius of 200 μm. The packaging structure

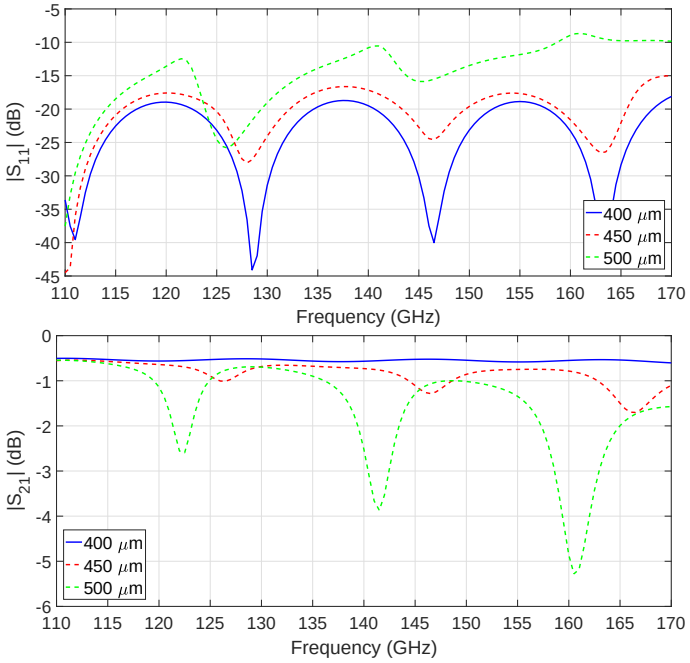

Figure 3.21: Simulation results of the packaged CPW at D-band with different CW values.

of the proposed transition at D-band is also shown in Fig. 3.22 which is designed in a back-to-back configuration consisting of two WR-6.5 rectangular waveguides with a length of 2 cm, a packaged CPW in the middle with a length of 2 mm, and two E-plane probe transitions. In the simulation, wave ports are used as the excitation scheme and they are located at the input and output of the packaging structure.

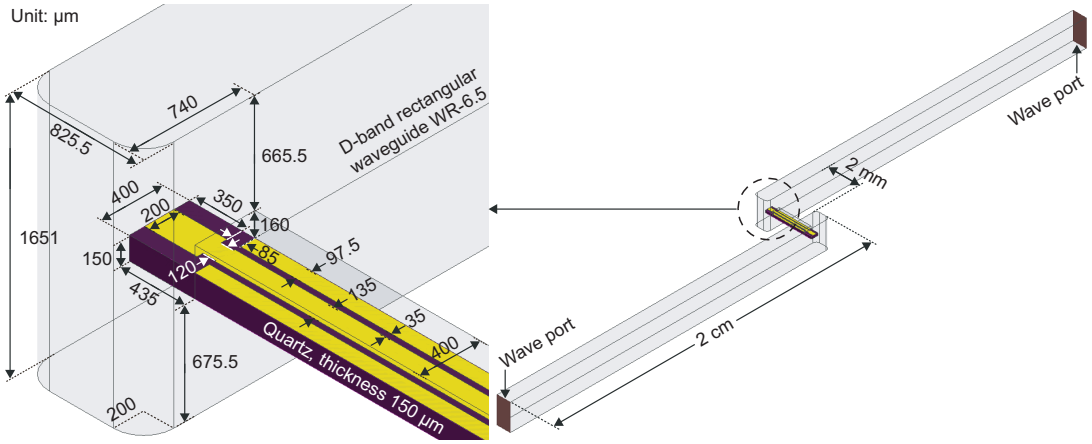

Figure 3.22: Rectangular waveguide-to-CPW transition at D-band using E-plane probe.

The proposed rectangular waveguide-to-CPW transition at D-band using E-plane probe was fabricated by following the same processes of gold sputtering, patterning, and dicing. Several samples were patterned on the quartz substrate and diced into pieces. For each diced sample, the width and length are 0.4 mm and 2.87 mm, respectively. With the purposes of easier fabrication and substrate alignment, the packaging structure was divided into two parts and each part was fabricated

using an aluminum block by milling process. Half of the input and output WR-6.5 rectangular waveguides and a recess with a depth of 150 μm were realized on the bottom structure while the top structure contains the rest half of the WR-6.5 rectangular waveguides as well as a 160 μm deep recess. The bottom recess is used for fitting the quartz substrate and the top recess works as the air cavity above the packaged CPW. Besides, in order to assemble the packaging structure accurately, two guide pins and four screws are used. Fig. 3.23 shows the fabricated packaging structure as well as the diced quartz substrate. The substrate was aligned inside the recess on the bottom structure and the gaps between the substrate and the recess were filled with silver conductive glue. Two standard WR-6.5 rectangular waveguide flanges without annular recess were fabricated at the input and output of the packaging structure.

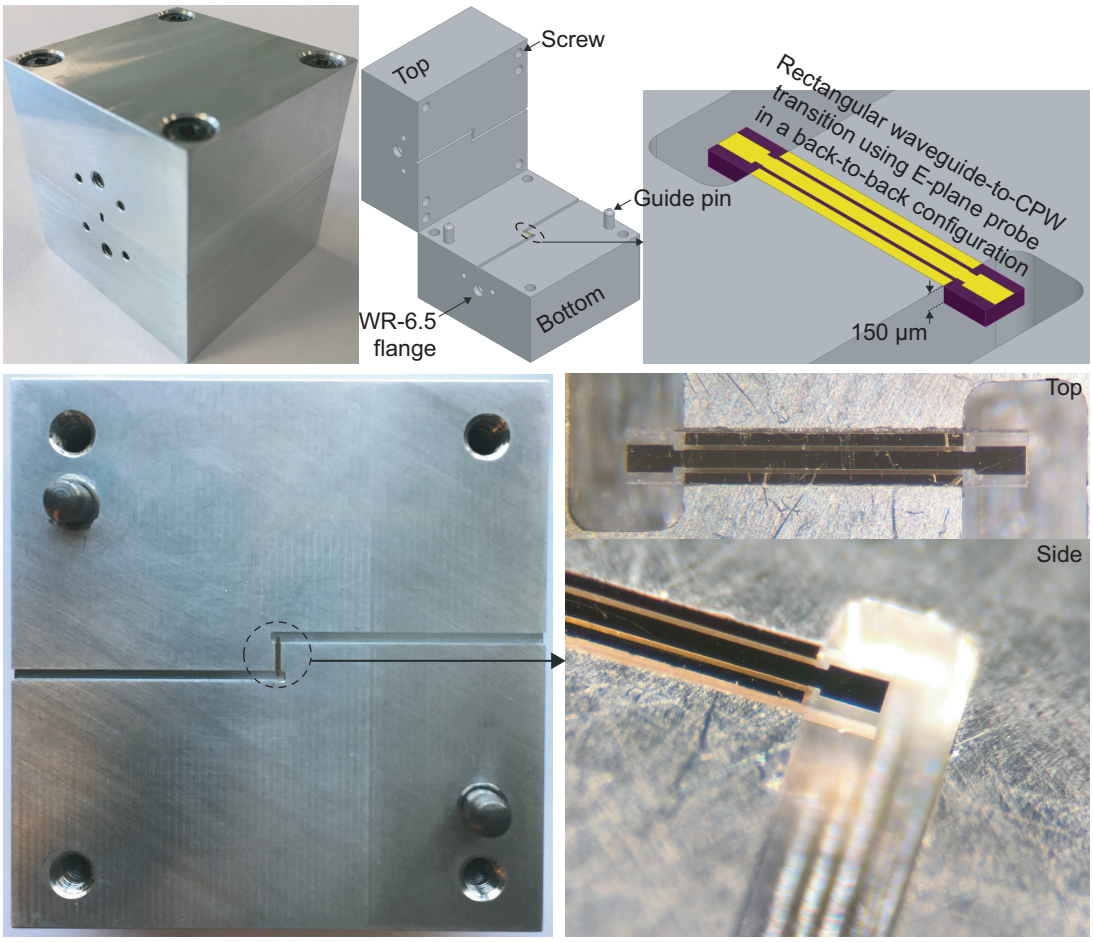

Figure 3.23: Fabricated rectangular waveguide-to-CPW transition at D-band using E-plane probe in a back-to-back configuration.

In order to improve the accuracy of measurements at D-band, a rectangular waveguide calibration kit has been designed and fabricated in-house. By implementing the through-reflect-line (TRL) calibration, the measured S-parameters can be calibrated to the input and output of the device under test (DUT). As is shown in Fig. 3.24, the calibration kit consists of a short reflection and three line structures which are straight WR-6.5 rectangular waveguides with lengths of 0.72 mm, 1.00 mm

and 1.44 mm, respectively. As a redundancy of the designed calibration kit, other lengths such as 1.72 mm and 2.44 mm can also be obtained by cascading two line structures together. The material of the calibration kit is brass and it was fabricated by milling process which uses a spinner with a diameter of 400 μm.

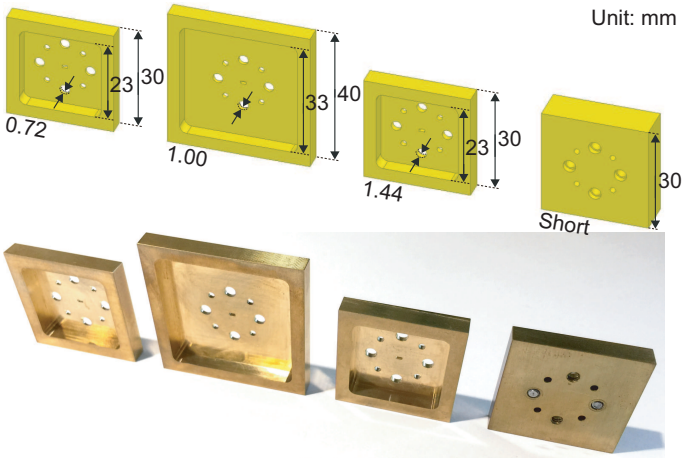

Figure 3.24: Rectangular waveguide calibration kit at D-band.

Fig. 3.25 shows the experimental setup which is used for measuring the proposed rectangular waveguide-to-CPW transitions at D-band. The measurement system comprises an Anritsu ME7808B VNA and two D-band extenders from VDI with WR-6.5 rectangular waveguide connections. Two-port S-parameters of the DUT can be measured from 110 GHz to 170 GHz and the TRL calibration is executed before each measurement.

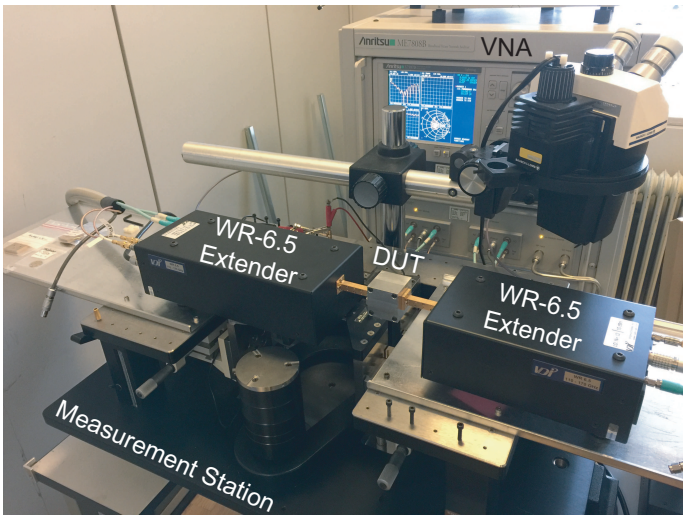

Figure 3.25: Experimental setup for rectangular waveguide measurement at D-band.

The measurement results (red solid lines) of the fabricated rectangular waveguide-to-CPW transition at D-band using E-plane probe in a back-to-back configuration are shown in Fig. 3.26 in comparison with the simulation results (blue dashed lines). Since the bandwidth is defined as

the width of the frequency band where the return loss is better than 10 dB, the proposed transition shows a simulated bandwidth of 60 GHz with an associated insertion loss of 0.7 dB which covers the whole D-band. For the fabricated transition prototype at D-band, the return loss remains better than 10 dB from 112.7 GHz to 170 GHz which corresponds to a bandwidth of 57.3 GHz and the insertion loss is less than 1.6 dB. Though the fabricated transition prototype exhibits a slightly higher insertion loss at D-band, a good agreement between simulation and measurement has been achieved.

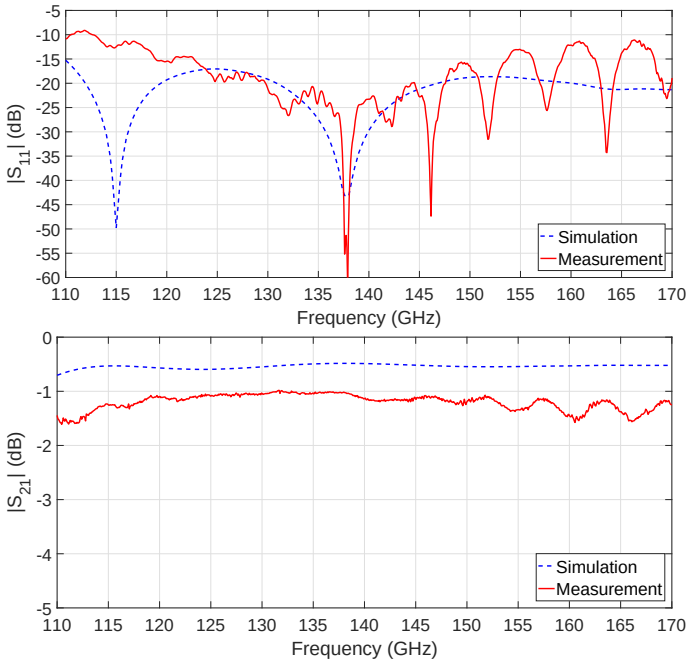

Figure 3.26: Measurement results of the fabricated rectangular waveguide-to-CPW transition at D-band using E-plane probe in a back-to-back configuration.

3.3.3 Transition Using Wire Bonding Probe

Since the method of using wire bonding probe for guiding electromagnetic waves from the rectangular waveguide to the CPW has been validated by the proposed transition prototype at U-band, another transition is designed at D-band with the purpose of investigating the performance of using wire bonding probe at higher frequencies. Fig. 3.27 demonstrates the proposed rectangular waveguide-to-CPW transition at D-band using wire bonding probe. The wire bonding itself works as a probe which connects the extended signal trace of the packaged CPW to a small square pad at the end of the substrate and it is inserted into a WR-6.5 rectangular waveguide through an aperture. When the operating frequency increases from U-band to D-band, the length of the square pad reduces to 50 μm and it locates 50 μm away from the edge of the substrate. Besides, for connecting the wire bonding probe, the extended signal trace of the packaged CPW has a length of 80 μm and a width of 100 μm. Since a conductor ball with a diameter of 80 μm have to be soldered and pressed at the start point on the substrate during the fabrication process of the wire bonding probe,

for the proposed transition at D-band, the wire bonding probe starts at the extended signal trace of the packaged CPW and terminates at the square pad. As is shown in Fig. 3.27, the packaging structure is designed in a back-to-back configuration. The rectangular waveguides as well as the packaged CPW are the same as those used for the E-plane probe transition in Fig. 3.22. In the simulation, wave ports are used as the excitation scheme and the same settings are applied.

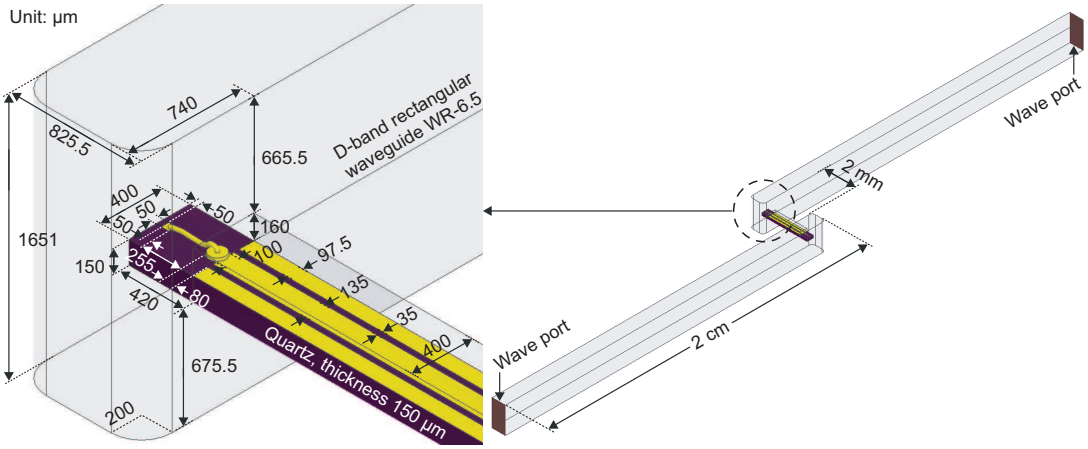

Figure 3.27: Rectangular waveguide-to-CPW transition at D-band using wire bonding probe.

Fig. 3.28 shows the details of the modeled wire bonding probe at D-band. The diameter of the wire bonding is 25 μm and the material is gold. The wire bonding has a fixed length of 320 μm which is the distance from the square pad to the extended signal trace. However, controlling the shape of the wire bonding probe is not as easy as controlling its length. As a result, the shape is modeled from the fabricated wire bonding with a similar length and it is described by six points on the curve. By adjusting the vertical positions of the points, the modeled wire bonding probe can be configured to different shapes which results in different operating frequencies. In order to investigate the performance sensitivity against the shape variation, the proposed transition at D-band using wire bonding probe is simulated with four different shapes.

Fig. 3.29 shows the simulation results of the rectangular waveguide-to-CPW transition at D-band using wire bonding probe with different shapes. By fixing the length of the wire bonding probe and increasing the total height from 53 μm to 83 μm, the operating frequency of the proposed transition shifts 7.5 GHz at D-band. Since the bandwidth of the transition refers to the width of the frequency band where the return loss is better than 10 dB, for the shape when $H1$ equals 20 μm, the proposed transition achieves the maximum bandwidth of 53.5 GHz ranging from 110 GHz to 163.5 GHz with an associated insertion loss of 1.1 dB.

The proposed rectangular waveguide-to-CPW transition at D-band using wire bonding probe shown in Fig. 3.27 was fabricated. The quartz substrate with a thickness of 150 μm was used and the same fabrication processes were followed. The samples patterned on the quartz substrate were diced into pieces with a width of 0.4 mm and a length of 2.84 mm. The wire bonding probes were made at the last step on the diced samples and according to the simulation results in Fig. 3.29, the height was kept as low as possible in order to achieve a larger bandwidth at D-band. Besides, the fabricated aluminum packaging structure for the proposed transition at D-band using E-plane probe

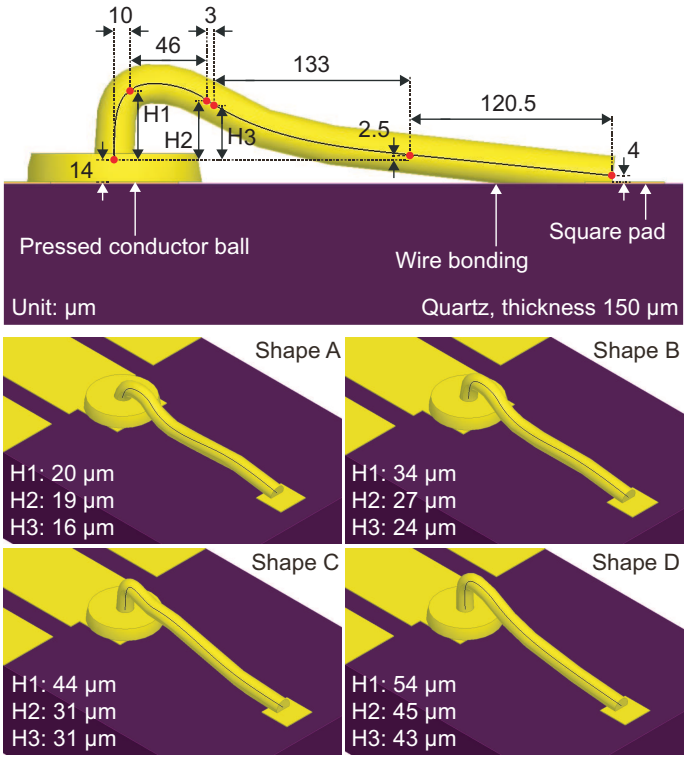

Figure 3.28: Different shapes of the wire bonding probe at D-band.

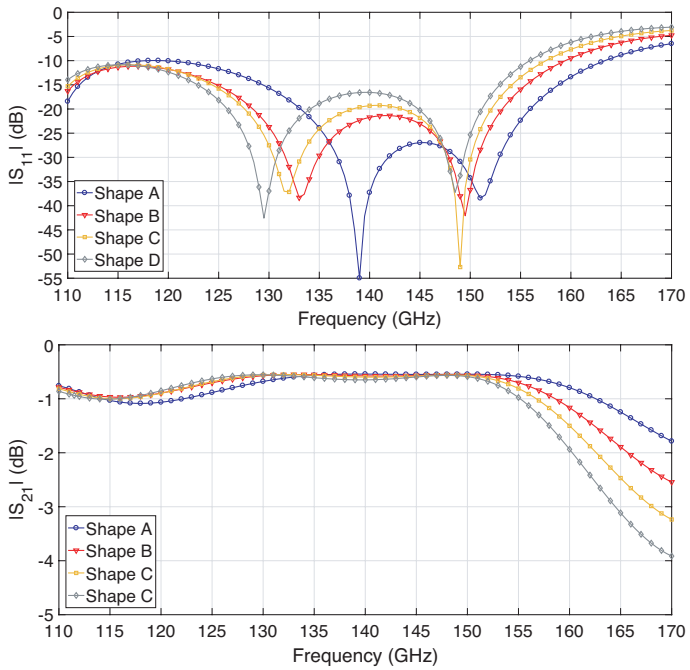

Figure 3.29: Simulation results of the rectangular waveguide-to-CPW transition at D-band using wire bonding probe with different shapes.

was reused by replacing the sample in the recess where the silver conductive glue was dissolved by acetone. Fig. 3.30 shows the reused packaging structure and the fabricated wire bonding probe at D-band.

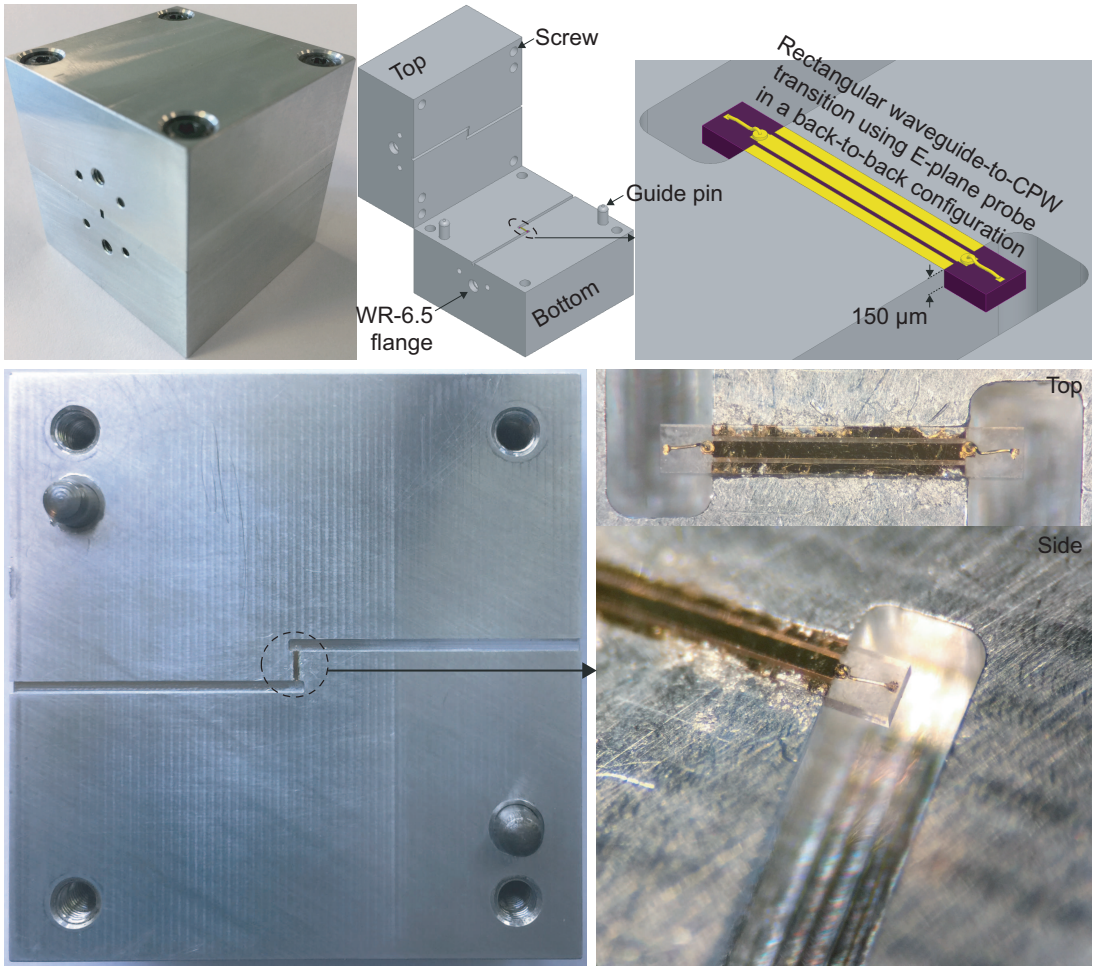

Figure 3.30: Fabricated rectangular waveguide-to-CPW transition at D-band using wire bonding probe in a back-to-back configuration.

The same measurement system was used and the TRL calibration was carried out. The red solid lines in Fig. 3.31 show the measurement results of the fabricated rectangular waveguide-to-CPW transition at D-band using wire bonding probe in a back-to-back configuration while the blue dashed lines are the simulation results. The fabricated transition prototype achieves a bandwidth of 56.3 GHz ranging from 110 GHz to 166.3 GHz with an associated insertion loss of 2 dB. Compared with the simulation results, a good agreement between simulation and measurement has been achieved. The differences between the simulation and measurement results are mainly caused by the fabrication and alignment tolerances, especially for the shape of the wire bonding probes and the gaps between the aluminum cover and the substrate.

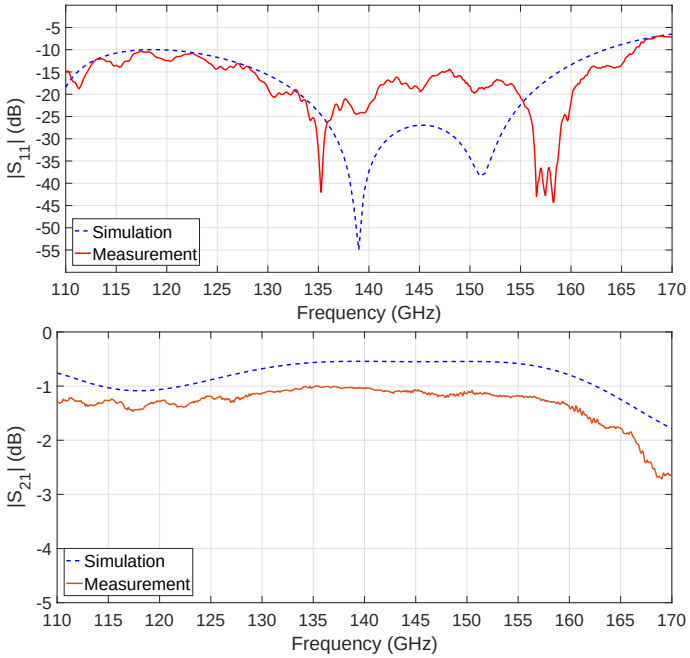

Figure 3.31: Measurement results of the fabricated rectangular waveguide-to-CPW transition at D-band using wire bonding probe in a back-to-back configuration.

3.3.4 Transition Using Wideband Patch Antenna

In free space, antennas are normally used for receiving and transmitting electromagnetic waves for wireless communications. However, when the electromagnetic waves are radiated into a specific environment such as a rectangular waveguide, the antenna works as the transition guiding electromagnetic waves from the feed line to the rectangular waveguide. At millimeter-wave and THz frequencies, antennas become small in size. Since most of the circuits as well as chips at such high frequencies rely on planar structures due to their fabrication processes, planar antennas have been widely used for direct wireless communication as well as system integration and packaging. The challenge of designing planar antennas is to achieve a high gain and at the same time a large bandwidth within a limited occupation area. Fig. 3.32 illustrates a novel patch antenna that is designed for wireless communications at D-band. The conventional patch antenna can be fed by different planar transmission lines and its dimensions are mainly related to the operating frequency which normally results in narrowband radiation with low directivity. Though hemispherical silicon lens, stacked dielectric resonators, and antenna arrays might be applied to increase the directivity of the planar antenna, either extra chip-level assembly or large occupation area on the substrate is required. Being optimized for wideband radiation, the proposed patch antenna has a rectangular ring structure which increases the gain and enlarges the bandwidth without adding extra element. In addition, the proposed patch antenna is directly fed by a CPW where the patch geometry is connected to the signal trace and the ground traces are designed as a part of the patch antenna.

The quartz substrate has a thickness of 150 μm and it has been used for other proposed transitions at D-band. The layer stack contains two conductor layers with a thickness of 400 nm

and the material is gold. The patch antenna is designed on the top conductor layer while the bottom conductor layer works as a ground plane. As a part of the patch antenna, a CPW feed with a length of 670 μm is included in the design which makes it possible for integrating directly with other circuits and chips based on CPW. The width of the signal trace is 50 μm and the width of the ground traces is 100 μm with a gap width of 20 μm. The signal trace is connected to a patch geometry which contains a rectangular ring with a width of 72 μm and a smaller rectangular patch at the center of the patch geometry. The ground traces are tapered out from 100 μm to 176 μm around the patch geometry forming another rectangular ring. Besides, the proposed patch antenna is a compromise by taking into account the performance and occupation area. The width and length of the quartz substrate are 1700 μm and 1462 μm, respectively. The ground plane is large enough to support antenna radiation while the dimensions of the proposed patch antenna are optimized for achieving the maximum bandwidth and gain at D-band.

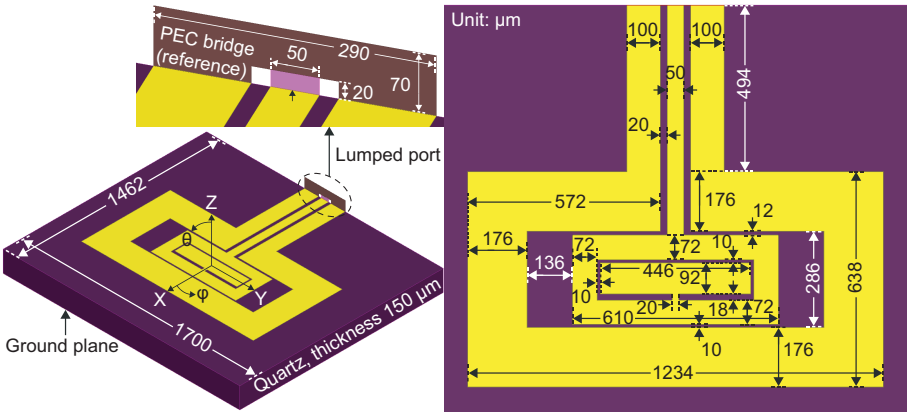

Figure 3.32: Wideband patch antenna for wireless communications at D-band.

For simulating the far-field radiation characteristics, the coordinate system is assigned to the center of the patch geometry and an air box with radiation boundary conditions is added around the patch antenna which has to be large enough to reach the antenna far-field region. Since the proposed patch antenna has a CPW feed, lumped port with vertical PEC bridge is used as the excitation scheme and the parasitic sheet inductance of the port is subtracted from the simulation results by post processing. The blue and red solid lines in Fig. 3.33 show the simulated far-field radiation patterns of the proposed patch antenna at 140 GHz when ϕ equals 0° and 90°, respectively. Based on the assigned coordinate system, a simulated antenna gain of 7.4 dBi is achieved in the direction perpendicular to the patch antenna where θ and ϕ are 0°. The gray solid line in Fig. 3.33 is the simulated return loss of the proposed patch antenna at D-band. With the rectangular ring structure, the return loss remains better than 10 dB from 115.3 GHz to 165.6 GHz which corresponds to a bandwidth of 50.3 GHz, or in other words 36% fractional bandwidth centered at 140 GHz. Compared with the conventional patch antenna at D-band, a larger bandwidth and a higher gain can be provided by the proposed patch antenna while the occupation area is still comparable.

As is shown in Fig. 3.34, apart from being implemented for direct wireless communications at D-band, the proposed patch antenna is inserted into a WR-6.5 rectangular waveguide through

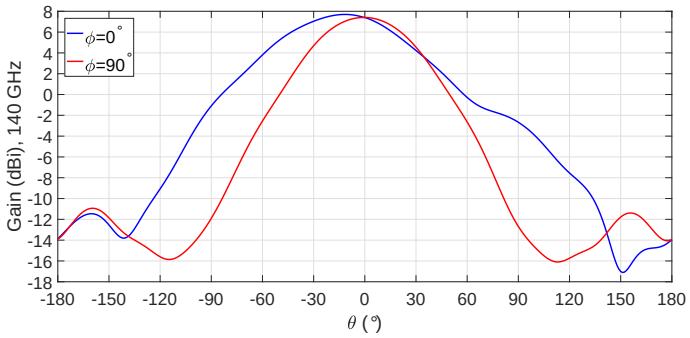

(a) Antenna gain at 140 GHz.

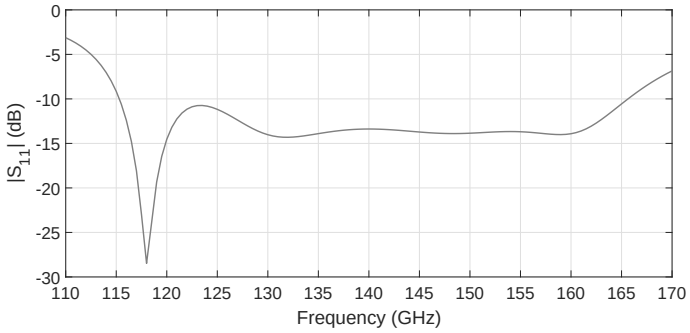

(b) Return loss at D-band.

Figure 3.33: Far-field simulation results of the wideband patch antenna.

an aperture which forms a rectangular waveguide-to-CPW transition at D-band. The rectangular waveguide is perpendicular to the patch antenna and aligned to the center of the patch geometry in the direction of maximum radiation. Besides, in order to guide electromagnetic waves smoothly from the rectangular waveguide to the patch antenna, a tapered waveguide is introduced between them where the width is kept constant and the height is reduced from 825.5 μm to 680 μm within a distance of 1000 μm. With the purpose of restricting the parasitic modes, the aperture has a width of 1050 μm which equals the width of the quartz substrate and the height of the air cavity above the CPW feed is 250 μm. Since the quartz substrate is placed at the end of the rectangular waveguide, the cavity has a depth of 150 μm and the termination works as the bottom ground plane for the patch antenna which also makes it unnecessary to have another conductor layer on the backside of the quartz substrate. Due to the milling process, the cavity for fitting the quartz substrate has round corners whose radius is 200 μm. Fig. 3.34 also demonstrates the packaging structure of the proposed transition at D-band in a back-to-back configuration. The packaging structure consist of two WR-6.5 rectangular waveguides including the bent and tapered structures, an air cavity in the middle, and two wideband patch antennas. In the simulation, wave ports are used as the excitation scheme and the same settings are applied.

When the proposed patch antenna shown in Fig. 3.32 is implemented as a rectangular waveguide-to-CPW transition, the dimensions of the patch antenna are optimized for the new environment condition which is changed from free space to a closed cavity. Fig. 3.35 shows the optimized dimensions of the wideband patch antenna in a back-to-back configuration which is used for

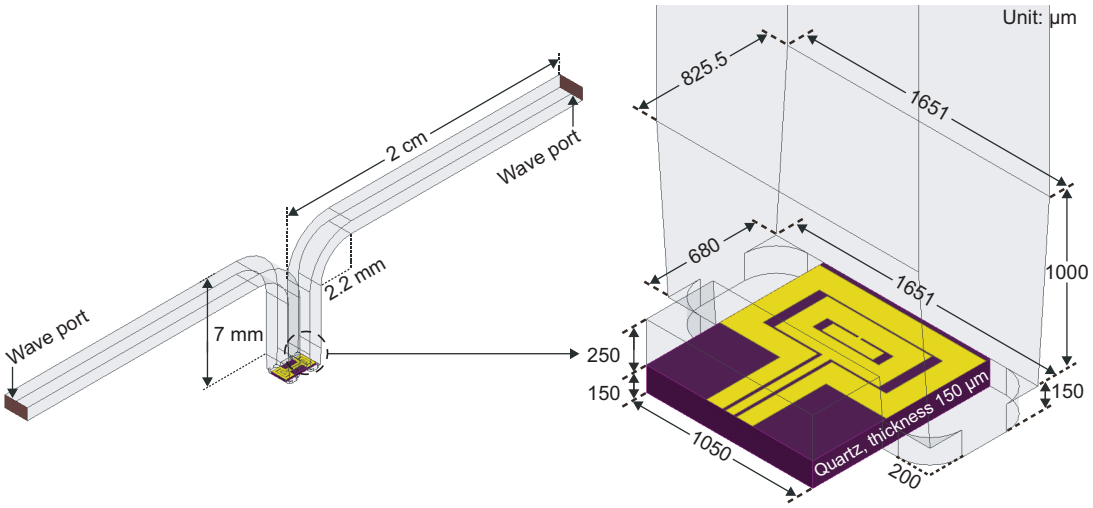

Figure 3.34: Rectangular waveguide-to-CPW transition at D-band using wideband patch antenna.

the proposed rectangular waveguide-to-CPW transition at D-band. The patch antenna shown in Fig. 3.32 is designed for direct wireless communications at D-band and it has a relatively large ground plane for radiation enhancement in free space while a more compact design can be achieved when the patch antenna is packaged inside a rectangular waveguide. The quartz substrate has a width of 1050 μm and a length of 2238 μm. The CPW in the middle of the quartz substrate has a length of 1200 μm which is the feed for the patch antennas on both sides. The width of the signal trace is 50 μm and the width of the ground traces is 100 μm with a gap width of 20 μm. The total width and length of the patch geometry are reduced to 1050 μm and 628 μm, respectively. Besides, the distance between the patch geometry and the the edge of the quartz substrate is 27 μm.

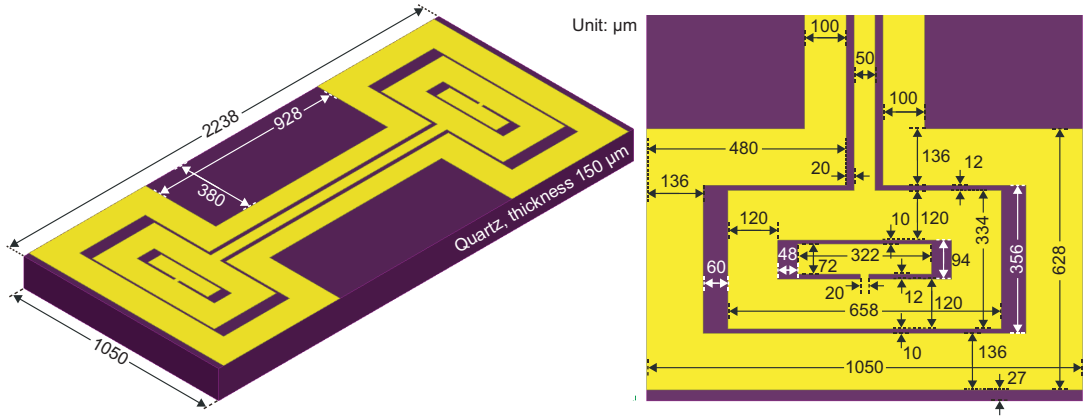

Figure 3.35: Wideband patch antenna in a back-to-back configuration for rectangular waveguide-to-CPW transition at D-band.

The proposed rectangular waveguide-to-CPW transition at D-band using wideband patch antenna was fabricated. Fig. 3.36 shows the fabricated packaging structure as well as the diced quartz substrate. The wideband patch antenna was fabricated on the quartz substrate by following the processes of gold sputtering, patterning, and dicing. In order to align the substrate and fabricate

the rectangular waveguides including bent and tapered structures, the packaging structure was divided into three parts and each part was fabricated using an aluminum block by milling process. The left and right parts have identical structures and each of them contains half of the WR-6.5 rectangular waveguides as well as the air cavity above the the CPW feed in the middle. The terminations of the rectangular waveguides and the cavity for fitting the quartz substrate were realized on the bottom part. Besides, the gaps between the quartz substrate and the cavity sidewalls were filled with silver conductive glue. Two standard WR-6.5 rectangular waveguide flanges without annular recess were also fabricated at the input and output of the packaging structure. During the assembly process, the left and right parts were firstly combined by using two guide pins and two screws. After that the bottom part was fixed to the combined structure by using four guide pins and four screws.

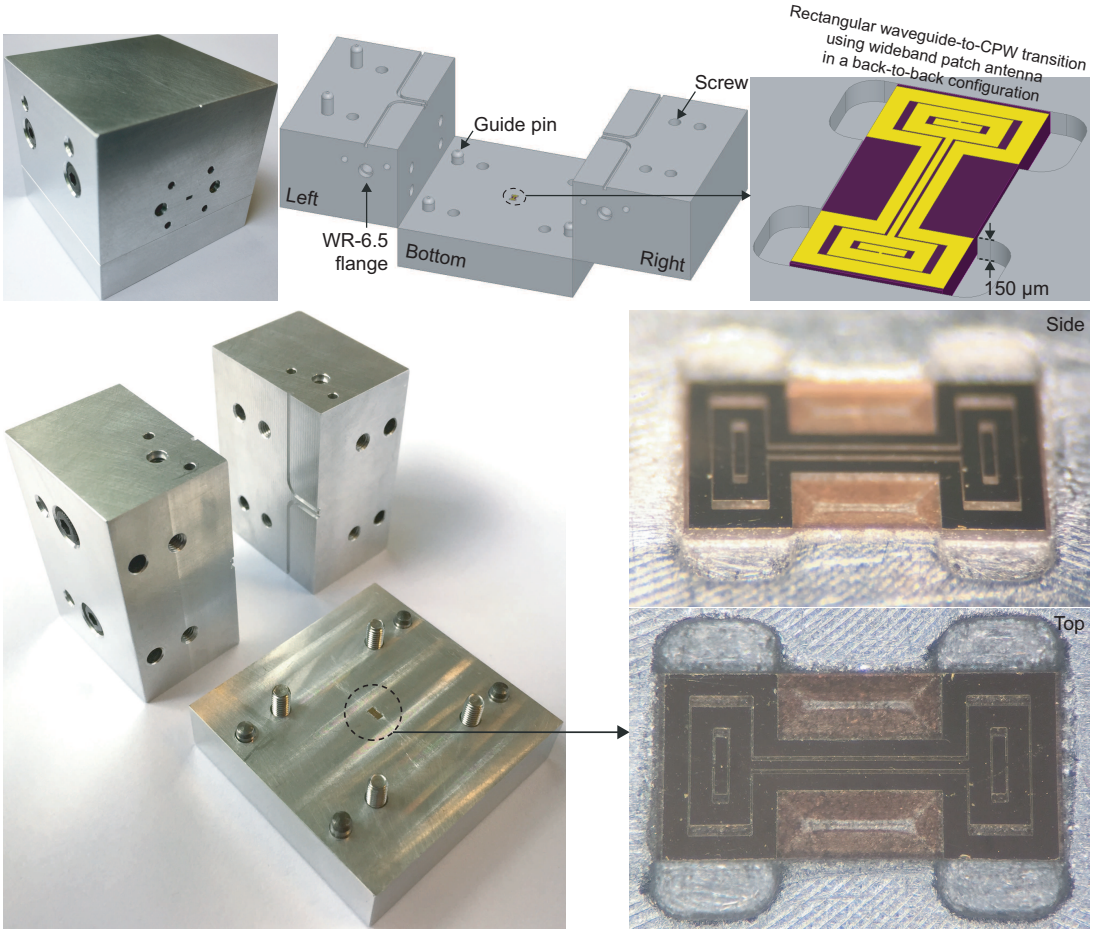

Figure 3.36: Fabricated rectangular waveguide-to-CPW transition at D-band using wideband patch antenna in a back-to-back configuration.

Fig. 3.37 shows the measurement results (red solid lines) of the fabricated rectangular waveguide-to-CPW transition at D-band using wideband patch antenna in comparison with the simulation results (blue dashed lines). The proposed transition was simulated and measured in a back-to-back configuration. The TRL calibration was applied to the measurement and the S-parameters were calibrated to the input and output of the fabricated packaging structure. For the fabricated transition

prototype at D-band, the return loss remains better than 10 dB from 118.8 GHz to 161 GHz which corresponds to a bandwidth of 42.2 GHz and the insertion loss is less than 4 dB. In other words, each transition contributes to 2 dB insertion loss. Compared with the simulation results, a similar bandwidth has been achieved while the fabricated transition prototype shows a higher insertion loss which is 2.6 dB more than the simulation. The differences between the measurement and simulation results are mainly caused by the fabrication tolerance of the milling and assembly processes especially the gaps between different parts of the packaging structure.

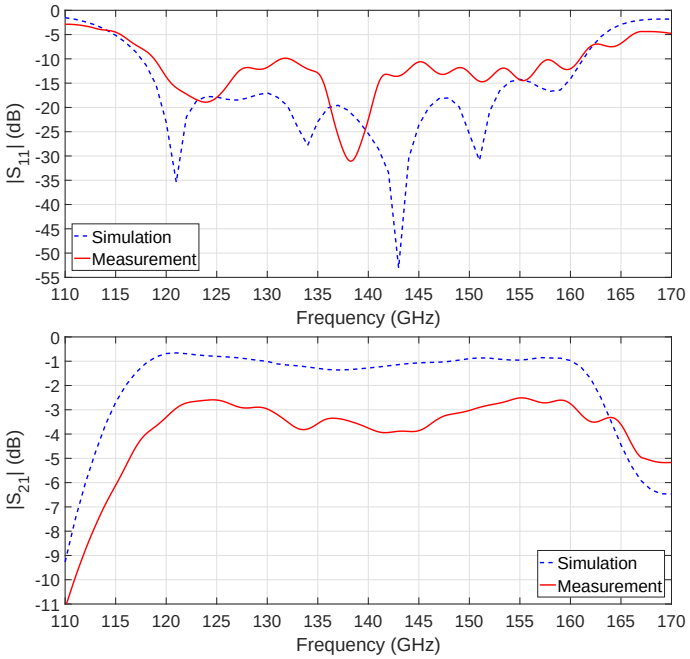

Figure 3.37: Measurement results of the fabricated rectangular waveguide-to-CPW transition at D-band using wideband patch antenna in a back-to-back configuration.

3.3.5 System Packaging Approaches

Though the methods of using E-plane probe, wire bonding probe, and wideband patch antenna for realizing rectangular waveguide-to-CPW transitions at D-band have been validated by the fabricated transition prototypes, each method has its own characteristics which suits for different applications and results in different system packaging approaches. In order to explain and compare the possible approaches for system packaging based on the proposed rectangular waveguide-to-CPW transitions using different methods, the layout of the chip reported in [26] is used as an example demonstrating the system packaging approaches regardless of its original operating frequencies and applications. Fig. 3.38 shows two possible approaches for system packaging where the electromagnetic waves are guided by the E-plane probe from the rectangular waveguide to the planar transmission line on the chip. Since both the chip and the E-plane probe are based on CPW, coplanar transitions between different transmission lines are not required. For the carrier substrate approach, the E-plane probe is fabricated on a separate substrate whose material as well as thickness can be different from the chip substrate. In this case, the E-plane probe is designed independently and the same design

can be reused for different chips operating at the same frequency band which makes it a standard component for system packaging. However, since the E-plane probe is separated from the chip, extra chip-level connections between them are required and it becomes the most critical part in a packaged system which normally affects the performance. For example, when wire bondings are used as the chip-level connections, it introduces parasitic inductance that degrades the bandwidth of the packaged system especially at high frequencies. As an alternative, the E-plane probe can be fabricated together with the chip on the same substrate forming the so-called on-chip E-plane probe [63]. For the on-chip approach, the chip-level connections can be avoided and a low-loss transmission can be achieved. However, under this circumstance, the E-plane probe have to be designed individually for each chip. Due to the width difference it normally leads to a substrate with concave corners which may require more advanced fabrication technologies. In some cases, with the purpose of restricting parasitic modes, the width of the designed E-plane probe might be much smaller than the thickness of the substrate. As a result, the dicing process may be complex for the fabricated E-plane probe due to its high thickness-to-width ratio. Besides, it is difficult to test or adjust the chip individually before system packaging which becomes a risk when several chips are packaged together. For packaging the chips with large sizes, an absorber might also be included inside the cavity above the circuits in order to prevent parasitic modes [52].

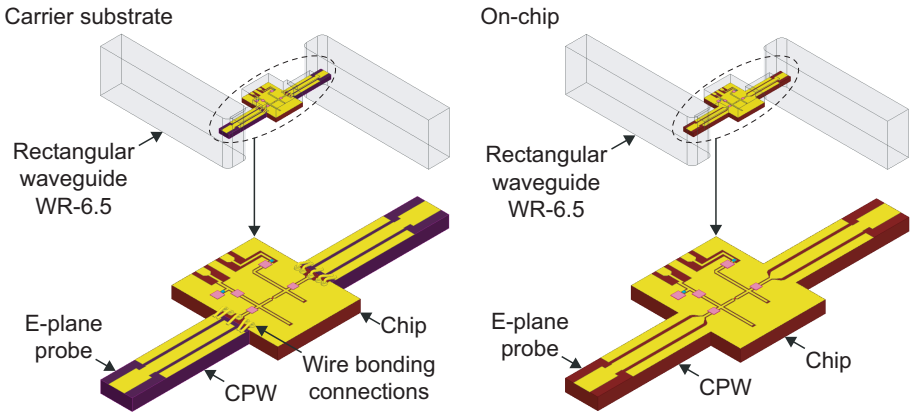

Figure 3.38: System packaging approaches using E-plane probe.

Fig. 3.39 shows two possible approaches for system packaging based on the rectangular waveguide-to-CPW transition using wire bonding probe. For both approaches, the wire bonding itself works as a probe connecting the signal trace of the chip to the conductor pad on the substrate. Because the wire bonding probe does not connect to the ground traces of the chip, it becomes versatile for packaging the chips based on different transmission lines such as CPW and MSL. Besides, there is no transmission line between the chip and the probe which means the chip-level connections can be avoided. For the carrier substrate approach, the conductor pad is patterned on a separate substrate which is used as a carrier under the chip. In this case, by taking into account the fabrication processes as well as substrate alignment, at the beginning the chip is fixed to the carrier substrate on the top for fabricating the wire bonding probe and the integrated components are aligned into a customized cavity inside the packaging structure afterwards. For the on-chip

approach, the conductor pad is patterned together with the chip on the same substrate. However, due to the width difference between the chip layout and the wire bonding probe, there are normally concave corners on the substrate which require more advanced fabrication technologies. Since the conductor pads on the chip are placed away from the chip layout, the testing and adjustment of the chip can be carried out prior to the fabrication of the wire bonding probe.

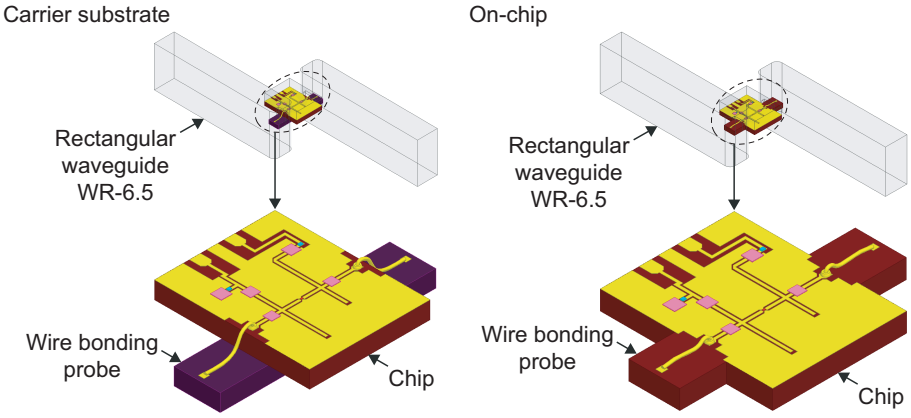

Figure 3.39: System packaging approaches using wire bonding probe.

Three possible approaches for system packaging based on the rectangular waveguide-to-CPW transition using wideband patch antenna are illustrated in Fig. 3.40. Since the wideband patch antenna has a CPW feed, it contains the same type of transmission line as the chip which can be directly connected to each other without adding coplanar transitions. For the carrier substrate approach, the wideband patch antenna including the CPW feed is designed and fabricated independently while the transition should provide a low-loss transmission at the operating frequencies of the chip. Wire bondings are used as the chip-level connections between the chip and the wideband patch antenna which introduces parasitic inductance and affects the bandwidth of the packaged system especially at high frequencies. For the on-chip approach, the wideband patch antenna is patterned together with the chip layout. Though the chip-level connections can be avoided in this case, the wideband patch antenna needs to be designed individually for each chip whose substrate thickness might not be suitable for designing wideband patch antennas. Besides, the concave corners on the substrate are also unavoidable and increase the fabrication complexity. Apart from the carrier substrate and on-chip approaches, the wideband patch antenna can be used for direct wireless communication which does not rely on any packaging structure or rectangular waveguide. The electromagnetic waves are radiated into free space from the wideband patch antenna. The transmitter and receiver chips are aligned towards each other in the direction of maximum radiation and a wireless communication link is established. Due to the intrinsic properties of wireless communications at high frequencies, the link is sensitive to the physical as well as electrical environments. In addition, the maximum distance for realizing stable transmission is one of the key concerns when designing the communication system.

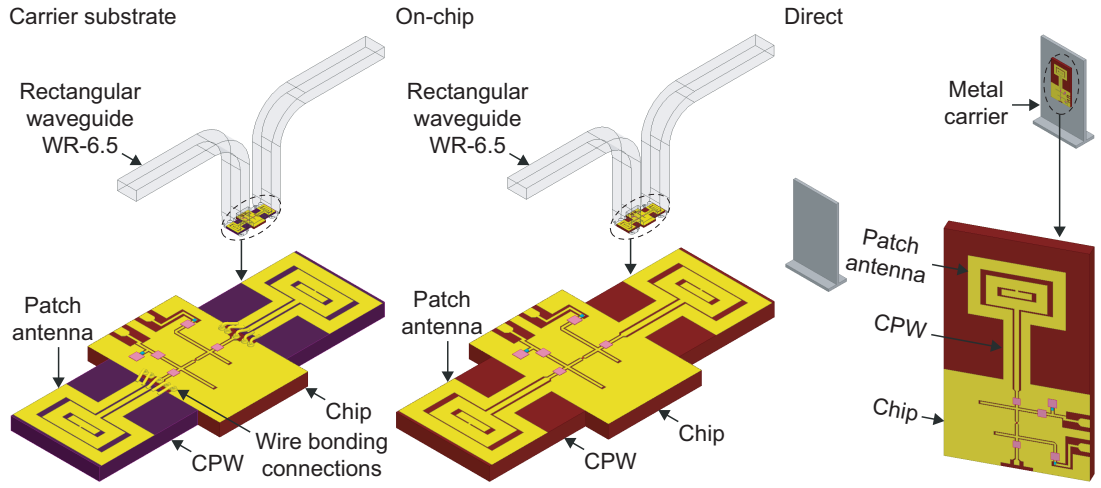

Figure 3.40: System packaging approaches using wideband patch antenna.

3.4 Summary

Rectangular waveguide-to-CPW transitions using different methods have been presented in this chapter. The structure, performance, and fabrication methods of rectangular waveguides have been discussed at the beginning. A D-band rectangular waveguide was fabricated by using 3D printing and copper plating processes. The fabricated waveguide prototype has a straight line structure with a length of 50.8 mm and the measurement results show a shift of the cutoff frequency for TE_{10} mode. Due to the uncertainties of the 3D printing process, the packaging structures including rectangular waveguides in this chapter were fabricated by using a traditional CNC milling process. Besides, a CPW has been designed with the purpose of acquiring the information of substrate properties at millimeter-wave and THz frequencies in particular the variations of ϵ_r and $\tan\delta$ which were measured by the supplier at a low frequency. Two prototypes with a length of 5 mm were fabricated based on glass and quartz substrates, respectively. The measurement results validate the performance of the quartz substrate up to 170 GHz and thus it has been used for fabricating the transitions proposed in this chapter.

After that, the proposed rectangular waveguide-to-CPW transitions at U-band have been demonstrated. A 50 Ω CPW based on the quartz substrate and packaged inside an aluminum cover has been designed as a part of the proposed transitions at U-band. Two transition prototypes at U-band using E-plane probe and wire bonding probe were fabricated and measured in a back-to-back configuration. The measurement system at U-band together with the rectangular waveguide calibration kit are also introduced. Being a reference using the existing technology, a bandwidth of 18 GHz with an associated insertion loss of 3 dB has been achieved at U-band by the fabricated transition prototype using E-plane probe. As a novel method, the wire bonding has been used as a probe guiding electromagnetic waves from the rectangular waveguide to the CPW. The fabricated transition prototype at U-band using wire bonding probe can provide a bandwidth of 11 GHz and an insertion loss of 3 dB. In addition, the performance sensitivity of the proposed transition at U-band against the shape variation of the wire bonding probe has been investigated.

For system packaging at higher frequencies, the proposed rectangular waveguide-to-CPW transitions at D-band have been illustrated. As a part of the proposed transitions, the packaged CPW was optimized for operating at D-band with the purposes of restricting parasitic modes and at the same time having a characteristic impedance of 50 Ω. Three transition prototypes at D-band using E-plane probe, wire bonding probe, and wideband patch antenna were fabricated and measured in a back-to-back configuration. Besides, a D-band rectangular waveguide calibration kit containing a short reflection and three straight line structures has been designed and fabricated for carrying out the TRL calibration. The measurement system at D-band has been introduced. The fabricated transition prototype at D-band using E-plane probe exhibits a bandwidth of 57.3 GHz while the insertion loss is less than 1.6 dB. Since the rectangular waveguide-to-CPW transition at D-band using E-plane probe is designed as a reference, it shows a smooth transmission with low insertion loss within a wide range of frequencies. In comparison, a bandwidth of 56.3 GHz and an insertion loss of 2 dB has been achieved by the fabricated transition prototype at D-band using wire bonding probe. The model and the performance sensitivity against the shape variation of the wire bonding probe at D-band are also investigated. While having a comparable performance at D-band, the wire bonding probe is more versatile and compact for system packaging. As an alternative, the wideband patch antenna which is originally designed for direct wireless communications at D-band has been implemented as a rectangular waveguide-to-CPW transition. The fabricated transition prototype at D-band using wideband patch antenna achieves a bandwidth of 42.2 GHz with an associated insertion loss of 4 dB. In Table. 3.1, the performances of the fabricated transition prototypes are compared.

Table 3.1: Rectangular waveguide-to-CPW transitions based on quartz substrate

Frequency	**Method**	**Structure**	**Insertion loss***	**Bandwidth+**
U-band	E-plane probe	Back-to-back	3 dB	18 GHz
U-band	Wire bonding probe	Back-to-back	3 dB	11 GHz
D-band	E-plane probe	Back-to-back	1.6 dB	57.3 GHz
D-band	Wire bonding probe	Back-to-back	2 dB	56.3 GHz
D-band	Wideband patch antenna	Back-to-back	4 dB	42.2 GHz

*The insertion loss is measured in a back-to-back configuration including two identical transitions.

+The bandwidth is defined as the width of the frequency band where the the return loss is better than 10 dB.

At the end of this chapter, the system packaging approaches at D-band based on the proposed rectangular waveguide-to-CPW transitions using E-plane probe, wire bonding probe, and wideband patch antenna have been demonstrated, respectively. For the carrier substrate approach, the proposed transitions are designed independently which are patterned on a separate substrate and extra chip-level connections are needed. For the on-chip approach, though the chip-level connections can be avoided where the proposed transitions are patterned on the same substrate as the chip, individual design and optimization are required. Besides, when the wideband patch antenna is used for direct wireless communications, the transceiver chips are aligned towards each other establishing a wireless communication link where the packaging structure is unnecessary.

CHAPTER 4

Integration and Packaging of Terahertz Photodetector

With the fast development of lightwave systems and the increasing demand for high-speed data transmissions through not only optical fibers over a long distance but also wireless links to mobile terminals [83]–[86], terahertz (THz) photodetectors as one of the principal devices used in communication systems are under intensive study. Photodetectors are normally based on either photodiodes or photoconductors which are electro-optic devices that can convert signals from optical domain to electrical domain. Photodiodes as well as photoconductors operating at THz frequencies have been pushed to achieve larger bandwidths [87]–[91]. Though both components can be implemented into photodetectors, they are based on different electro-optic effects which result in different characteristics. By adding an undoped region in a semiconductor junction, the photodiodes work as a rectifier converting light photons into current while the resistance of photoconductors is related to the number of free carriers in the photoconductive material generated by the light photons. At millimeter-wave and THz frequencies, not only the components but also the strategies for system integration and packaging are being challenged and efforts have been paid to improve the performances [21], [92]–[96]. Fig. 4.1 shows the system diagram of a THz photodetector based on a photoconductor which is packaged inside a rectangular waveguide and included as a part of the transmitter (Tx) for wireless data transmissions at W-band. Instead of directly using a log-periodic antenna with a silicon lens [97], the rectangular waveguide allows the packaged photodetector being easily cascaded with the amplifiers and horn antenna in the system.

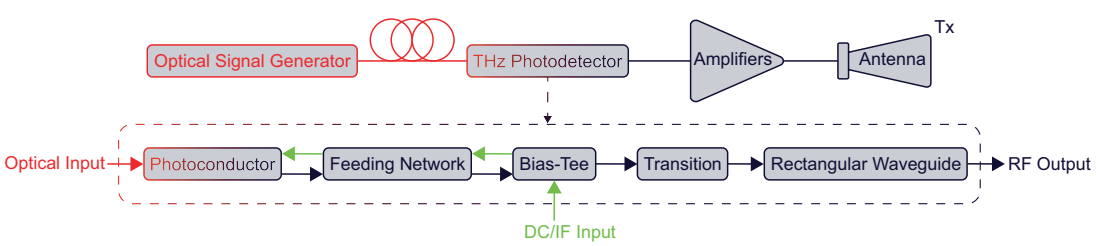

Figure 4.1: System diagram of the THz photodetector as a part of the transmitter for wireless data transmissions at W-band.

In THz communication systems, as one of the possible methods, a laser can be used as the light source and the data is modulated to the optical carrier by using a Mach-Zehnder modulator (MZM). After that, the modulated optical signal is transmitted to the photodetector through an optical fiber which needs to be aligned accurately with the photoconductor. The photoconductor is attached to a feeding network and the radio frequency (RF) signal is generated by the photoconductor based on the optical input. Besides, depending on the modulation scheme of the communication system, not only the direct current (DC) bias but also the intermediate frequency (IF) signal might have to be provided to the photoconductor. As a consequence, a bias-tee is connected to the feeding network and chip-level connections between them are required. The bias-tee is a three-port component based on planar transmission lines where the RF signal is transmitted freely towards to the connected component while the DC bias and IF signal can only be guided backwards to the photoconductor [98]. Since a rectangular waveguide serves as the interface of the packaging structure, a transition based on planar transmission lines is inserted for guiding the RF signal from the bias-tee to the rectangular waveguide. By its nature, the rectangular waveguide isolates the DC bias as well as the IF signal, otherwise a DC block needs to be included in the bias-tee or implemented before the RF output of the photodetector [99].

The system integration and packaging of a photodetector at W-band (75-110 GHz) for terahertz (THz) communications are addressed in this chapter. The photoconductor and its feeding network based on indium phosphide (InP) substrate are introduced at the beginning. After that the design of a bias-tee at W-band is described and the effects of parasitic modes are discussed. Besides, the E-plane probe transition between a W-band rectangular waveguide (WR-10) and a coplanar waveguide (CPW) is illustrated. The bias-tee as well as the E-plane probe transition are based on high-resistivity silicon (Si) substrate where wire bonding bridges are added on the top for restricting parasitic modes. The integration approach and the packaging structure are introduced. The proposed bias-tee and the E-plane probe transition including the rectangular waveguide are fabricated, integrated, and measured. The measurement is carried out on-wafer in a back-to-back configuration and the results are presented. At the end of this chapter, the assembly of the packaged photodetector is demonstrated and a THz heterodyne communication system is implemented.

4.1 Feeding Network for Photoconductor

For guiding the RF signal at W-band generated by the photoconductor, a CPW is used as the feeding network due to its planar structure, low-loss property, and adjustable dimensions. At the same time, the DC bias and IF signal have to be provided to the photoconductor through the feeding network. Fig. 4.2 shows the structure of the proposed CPW feed based on InP substrate with a thickness of 350 μm which was designed at the Terahertz Systems Technology Group, Technische Universität (TU) Darmstadt, Darmstadt, Germany. The CPW was originally designed to have a characteristic impedance of 50 Ω based on the InP substrate with a bottom ground plane. The width of the signal trace is 50 μm and the width of the ground traces is 300 μm with a gap of 50 μm. The gold conductor layer has a thickness of 400 nm. For aligning the photoconductor, the width of the signal trace is reduced to 8 μm at the end while the ground traces are merged into a ground pad.

The distance between the signal trace and the ground pad is 6 μm. Wire bonding bridges are added on the top of the substrate along the CPW with the purpose of restricting parasitic modes. The diameter is 25 μm and the height is 50 μm. The InP substrate has a width of 750 μm and a length of 800 μm. The ϵ_r and tanδ are 12.56 and 2e-4, respectively. In the simulation, lumped ports are used as the excitation scheme. The photoconductor is represented by a lumped port located in the gap between the signal and ground traces. The parasitic sheet inductance is calibrated out by post processing. An air cavity with radiation boundary conditions around the substrate is also included.

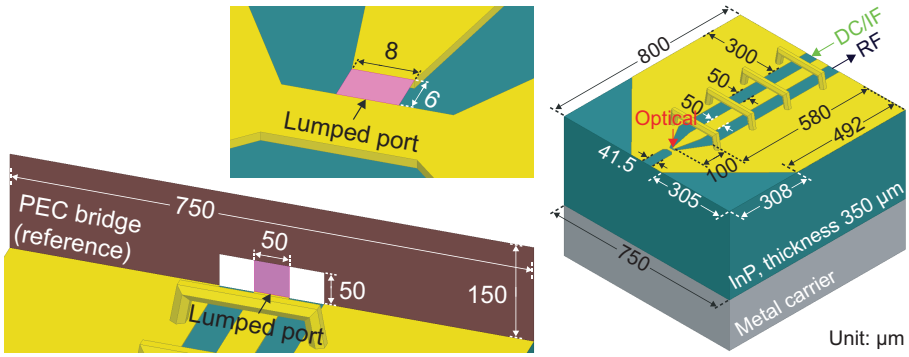

Figure 4.2: CPW feed based on InP substrate for the photoconductor.

The simulation results of the CPW feed at W-band with wire bonding bridges are shown by the blue solid lines in Fig. 4.3. The return loss remains better than 17 dB and the insertion loss is less than 0.5 dB. The red dashed lines are the simulation results when the wire bonding bridges are removed from the CPW feed. A similar performance is achieved and no visible notch can be observed in the frequency band.

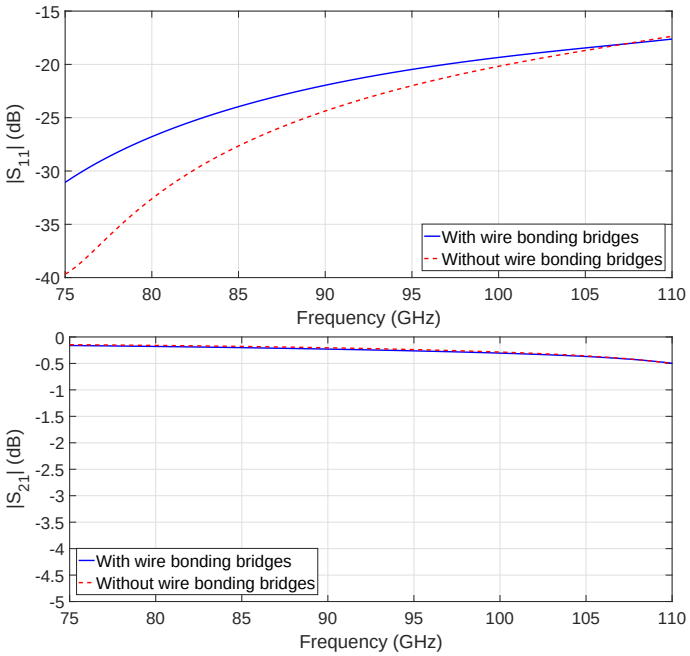

Figure 4.3: Simulation results of the CPW feed at W-band.

4.2 W-Band Bias-Tee

The bias-tee in the integrated system is used for guiding not only the RF signal from the feeding network to the transition but also the DC supply and IF signal to the photoconductor through the feeding network. Under this circumstance, the bias-tee at W-band has to provide a low-loss transmission on the RF path and at the same time a good isolation on the DC/IF path. By taking into account the feeding network, transition, and rectangular waveguide, the bias-tee is designed using CPWs which is more versatile for adjusting the dimensions as well as characteristic impedance. Fig. 4.4 illustrates the proposed bias-tee based on high-resistivity Si substrate with a thickness of 280 μm. The ϵ_r and tanδ of the Si substrate are 11.6 and 4e-3, respectively.

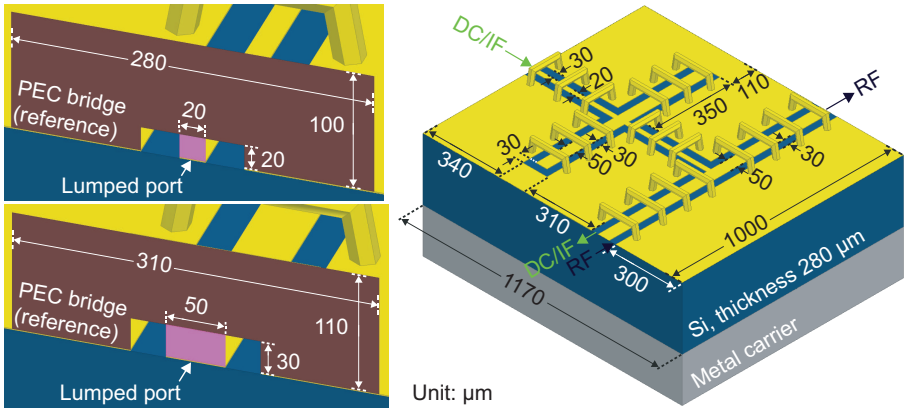

Figure 4.4: Bias-Tee based on Si substrate.

The RF path is a CPW through line with a length of 1 mm and a characteristic impedance of 50 Ω. For easier integration with the feeding network, the width of the signal trace is designed to be identical which is 50 μm. The DC/IF path is connected to the RF path in the middle and the width of the signal trace is optimized to 20 μm. In both cases, the gap between the signal and ground traces is 30 μm. In order to prevent the RF signal from leaking to the DC/IF path, two open-circuited CPW stubs are implemented in parallel. The equivalent schematics of the proposed bias-tee and the corresponding impedance transformations on the Smith chart are shown in Fig. 4.5. The original idea for designing the bias-tee is to implement a through line structure on the RF path and a quarter-wavelength transformer on the DC/IF path which converts the termination from short to open. For the first schematic, a quarter-wavelength CPW is followed by a half-wavelength CPW short-circuited stub. P_1, as the start point in the schematic, locates at the short-circuited point on the Smith chart. When the short-circuited CPW stub has a length of half wavelength, P_1 moves 360° along the edge of the Smith chart and reaches P_2 which locates at the same point. Due to the quarter-wavelength transformer, P_2 moves another 180° and terminates at P_3 which corresponds to the open-circuited point on the Smith chart. In this case, the RF signal is isolated from the DC/IF path. However, the DC bias is directly short-circuited by the stub. As an alternative, the short-circuited CPW stub is replaced by an open-circuited CPW stub whose length is reduced to quarter wavelength. The second schematic shows the optimized design. In the corresponding Smith chart, P_1 at the open-circuited point moves 180° at the beginning and arrives at P_2 which

locates at the short-circuited point. After that, P_2 moves 180° towards the open-circuited point and terminates at P_3. In this way, not only the DC bias survives but also a more compact design is achieved. As is shown in the third schematic, by adding another identical open-circuited CPW stub in parallel, the isolation for the RF signal can be further improved while it does not increase the occupation area of the bias-tee.

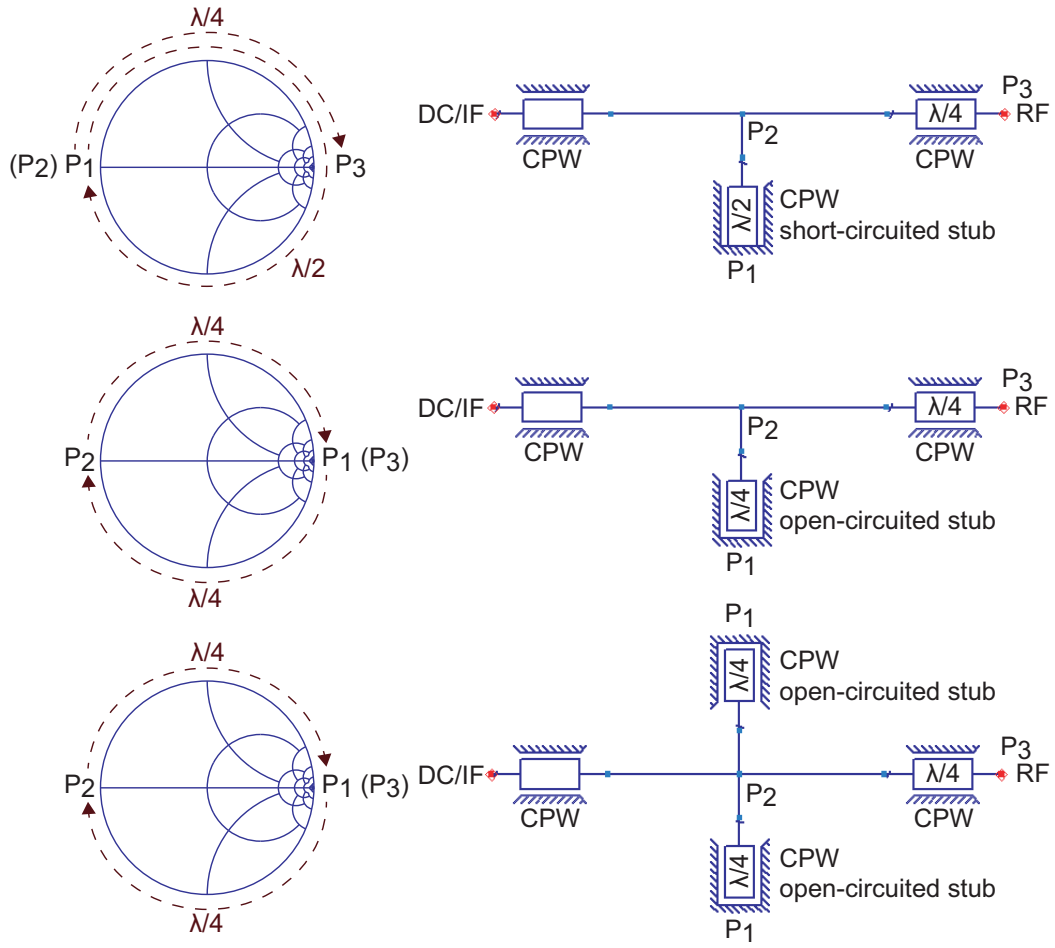

Figure 4.5: Equivalent schematics of the bias-tee.

The bias-tee is designed by following the third schematic in Fig. 4.5 and the dimensions are optimized for the RF signal at W-band. For restricting parasitic modes, wire bonding bridges are added along the paths. In the simulation, the bias-tee is surrounded by an air cavity with radiation boundary conditions. For both RF and DC/IF paths, lumped ports with vertical perfect electric conductor (PEC) bridges are used as the excitation scheme and their parasitic sheet inductances are subtracted from the simulation results. Fig. 4.6 shows the simulation results of the proposed bias-tee at W-band. With wire bonding bridges, as is shown by the blue solid lines, the proposed bias-tee exhibits a smooth transmission. The return loss is better than 16.6 dB with an associated insertion loss of 0.9 dB. Besides, the simulated isolation for the RF signal is more than 18.6 dB. In comparison, the red dashed lines are the simulation results of the proposed bias-tee without wire bonding bridges. The performances degrade seriously above 95 GHz.

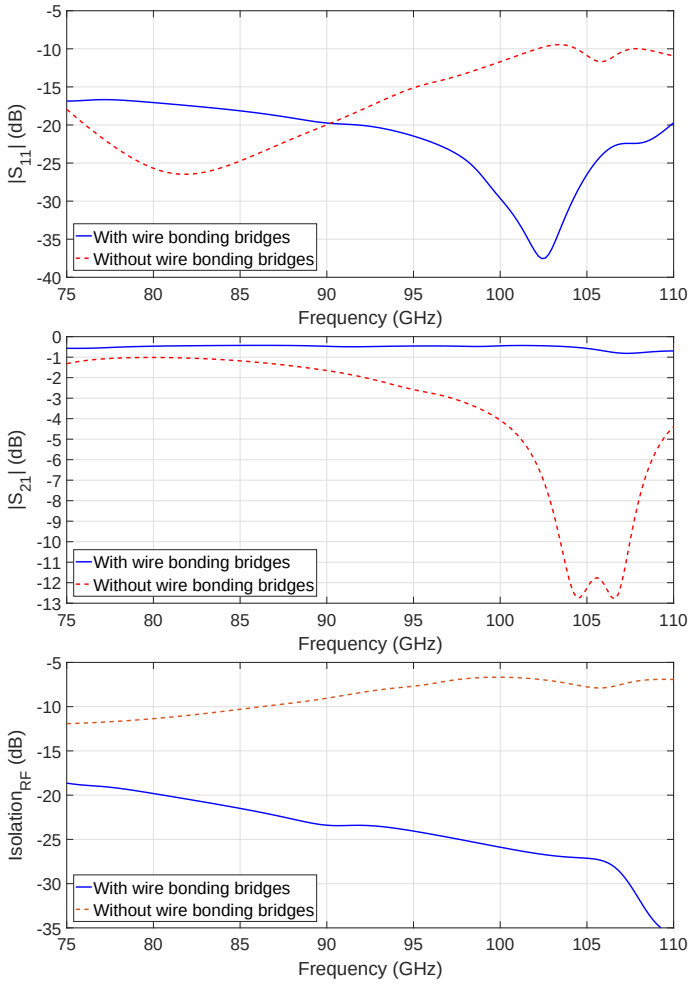

Figure 4.6: Simulation results of the bias-tee at W-band.

4.3 W-Band Rectangular Waveguide-to-Coplanar Waveguide Transition

According to the research work described in Chapter 3, the E-plane probe transition shown in Fig. 4.7 is designed for packaging the photoconductor. The rectangular patch patterned on a high-resistivity Si substrate works as the E-plane probe which is inserted into the WR-10 rectangular waveguide through an aperture cut. The E-plane probe is placed 740 μm from the end of the rectangular waveguide which forms a quarter-wavelength transformer converting the termination from short to open. In order to guide the RF signal from the bias-tee to the E-plane probe smoothly, a CPW is included in the transition structure which has a length of 1 mm and a characteristic impedance of 50 Ω. Though the CPW is patterned on the same Si substrate, its dimensions are optimized for the new environment conditions due to the metal cover. The signal trace has a width of 80 μm and the width of the ground traces is 110 μm with a gap of 50 μm. On one side, for connecting the packaged CPW to the RF path on the bias-tee, the widths of the signal trace and the gap are reduced to 50 μm and 30 μm, respectively, within a distance of 100 μm. On the other side, the signal trace is extended with a length of 70 μm and a width of 50 μm. For fitting the substrate,

the thickness of the slot is 280 μm while the air cavity above the CPW has a height of 200 μm. In addition, wire bonding bridges are added along the CPW for restricting parasitic modes.

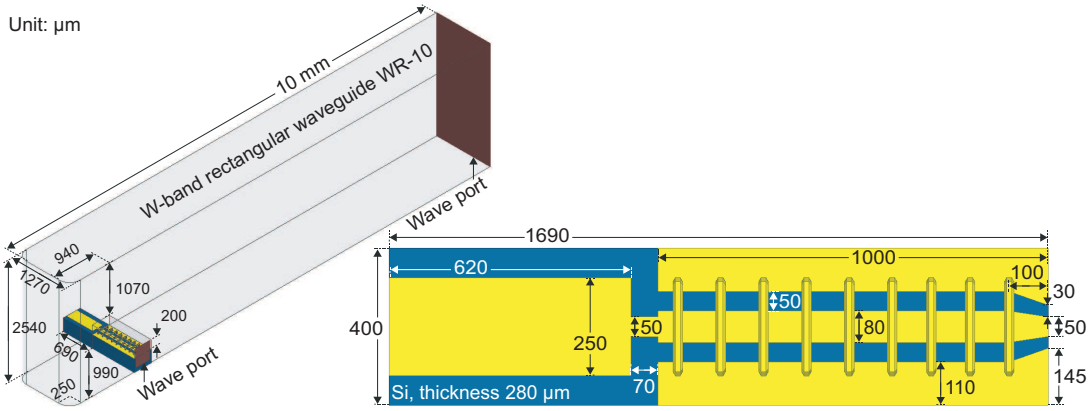

Figure 4.7: Rectangular waveguide-to-CPW transition at W-band using E-plane probe.

In the simulation, the length of the rectangular waveguide is set to 10 mm and wave ports are used as the excitation scheme. The rounded corners at the end of the rectangular waveguide are also included for being compatible with the milling process which results in a radius of 250 μm. Fig. 4.8 shows the simulation results of the proposed E-plane probe transition at W-band. As is shown by the blue lines, the transition with wire bonding bridges exhibits a wideband behavior. The return loss remains better than 18.8 dB with an associated insertion loss of 0.6 dB. In contrast, the red lines represent the simulation results of the transition without wire bonding bridges and a notch appears around 93 GHz which is due to the parasitic mode in the transition cavity.

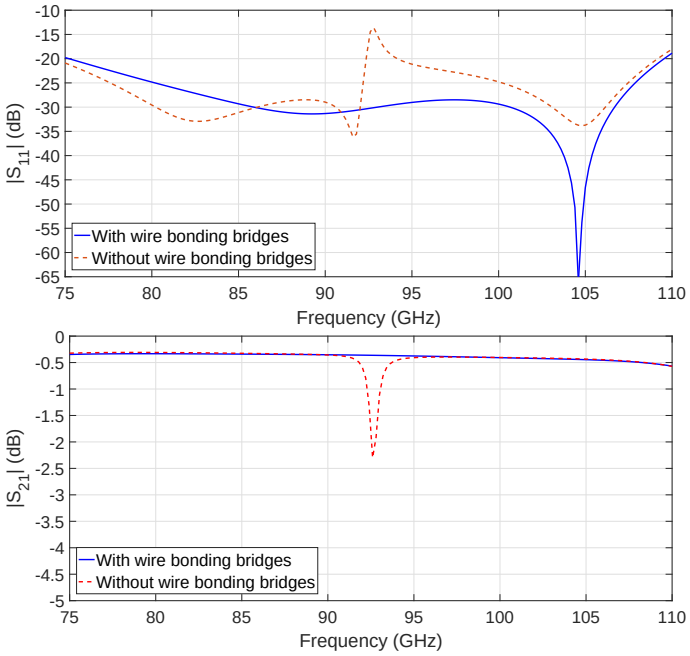

Figure 4.8: Simulation results of the rectangular waveguide-to-CPW transition at W-band using E-plane probe.

4.4 System Integration and Packaging

Based on the system diagram shown in Fig. 4.1 and the individual components introduced in this chapter, the photoconductor is packaged into a W-band photodetector. As is shown in Fig. 4.9, the integration method and packaging structure of the bias-tee and E-plane probe transition are firstly addressed. A metal cover is used for realizing the WR-10 rectangular waveguide, packaging the E-plane probe transition, and supporting the bias-tee. Wire bondings are implemented as the chip-level connections between the bias-tee and the E-plane probe transition. The bias-tee is also optimized from the original design.

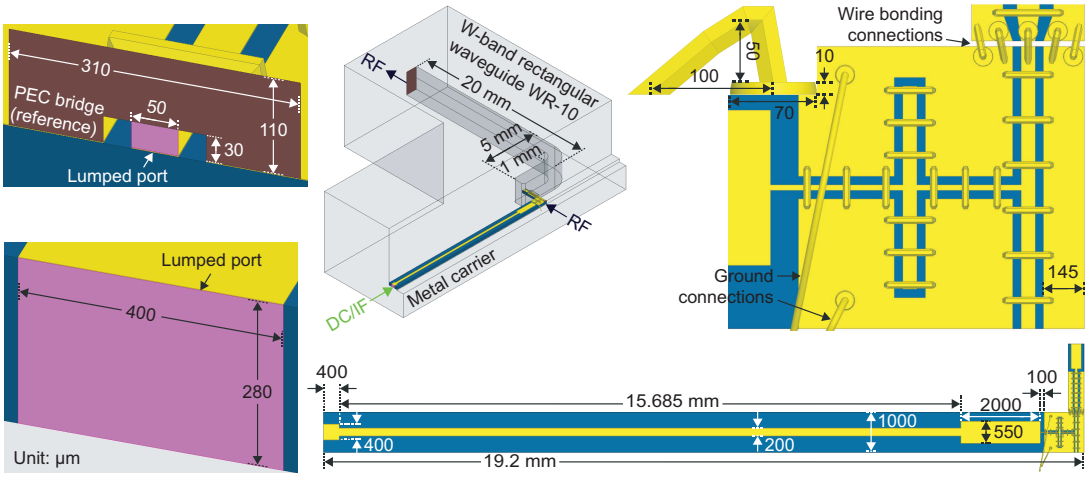

Figure 4.9: Integration of the bias-tee and E-plane probe transition.

For the RF path, the width of the ground trace is reduced from 300 μm to 145 μm which touches the metal carrier on the edge and makes it easier to be aligned with the packaged CPW. Wire bondings are used as the chip-level connections between the bias-tee and the E-plane probe transition whereas it introduces parasitic inductance especially at high frequencies and affects the bandwidth of the integrated system. As a results, the bias-tee and the E-plane probe transition are placed as close as possible in order to reduce the length of the wire bonding connections. In addition, another two wire bondings are used for providing ground connections to the bias-tee. For the DC/IF path, the feed line is extended in order to reach the inputs which are connected to the bias-tee through a SMA connector at the far end. The signal trace of the CPW on the DC/IF path is extended at the beginning with a length of 100 μm. After that, the feed line goes through an impedance transformer, a 50 Ω microstrip line (MSL), and a square pad. With the purpose of increasing the bandwidth, an impedance transformer based on MSL is inserted as a part of the feed line whose width and length are 550 μm and 2 mm, respectively. For the 50 Ω MSL, it has a width of 200 μm and a length of 15.685 mm. The square pad at the end of the feed line has a length of 400 μm and is reserved for connecting to the SMA connector. Based on the optimizations, the length of the Si substrate is still 1 mm while the width increases from 1.17 mm to 19.2 mm. The WR-10 rectangular waveguide shown in Fig. 4.7 has a through line structure which results in an incompatible packaging structure for the experimental setup at W-band. As an alternative, the

rectangular waveguide is bent 90° by using a quadrant structure. For minimizing the reflection, the quadrant structure has an inner radius of 1 mm and it is placed 4 mm away from the end of the rectangular waveguide. In the simulation, different types of excitation schemes are used. Lumped port with PEC bridge is used for the RF input while wave port is used for the RF output. Since the feed line of the DC/IF path is based on MSL, lumped port is used for the IF input which is assigned to the sheet between the MSL and the metal carrier. Besides, the parasitic sheet inductances caused by the lumped ports are calibrated out from the simulation results.

When the CPW feed with the photoconductor is integrated with the designed bias-tee and E-plane probe transition, the integration method and packaging structure is shown in Fig. 4.10. Compared with the packaging structure illustrated in Fig. 4.9, the CPW feed with the photoconductor is aligned with the RF path of the bias-tee. In order to compensate the thickness difference between the InP and Si substrates, the CPW feed is placed on a platform which is 70 μm lower than the platform supporting the bias-tee and the E-plane probe transition. The vertical gap on the metal carrier between two platforms also helps to align the components at the correct positions. Wire bondings are used for not only providing ground connections but also chip-level connections. In the simulation, the photoconductor is replaced by a sheet which is located in the gap between the signal and ground traces. As is shown in Fig. 4.2, lumped port is used as the RF input which is assigned to the sheet representing the photoconductor. The RF output and IF input are the same as those illustrated in Fig. 4.9.

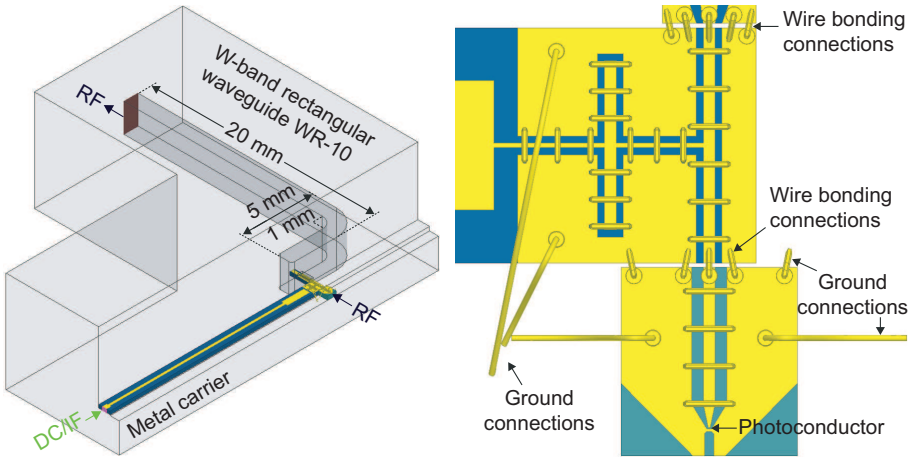

Figure 4.10: Integration of the photoconductor, CPW feed, bias-tee, and E-plane probe transition.

Fig. 4.11 shows the simulation results of the integrated components. The blue solid lines correspond to the simulation results of the packaging structure shown in Fig. 4.9 which includes the bias-tee, E-plane probe transition, and WR-10 rectangular waveguide. The red dashed lines represent the simulation results of the packaging structure shown in Fig. 4.10 in which the CPW feed is also integrated. For the RF signal at W-band, in both cases, the return loss remains better than 15 dB and at the same time the isolation is more than 14.5 dB. The insertion loss is increased from 1.5 dB to 2.3 dB when the CPW feed is integrated. For the IF signal, in both cases, the return loss is better than 7.7 dB up to 10 GHz while the insertion loss is less than 2 dB.

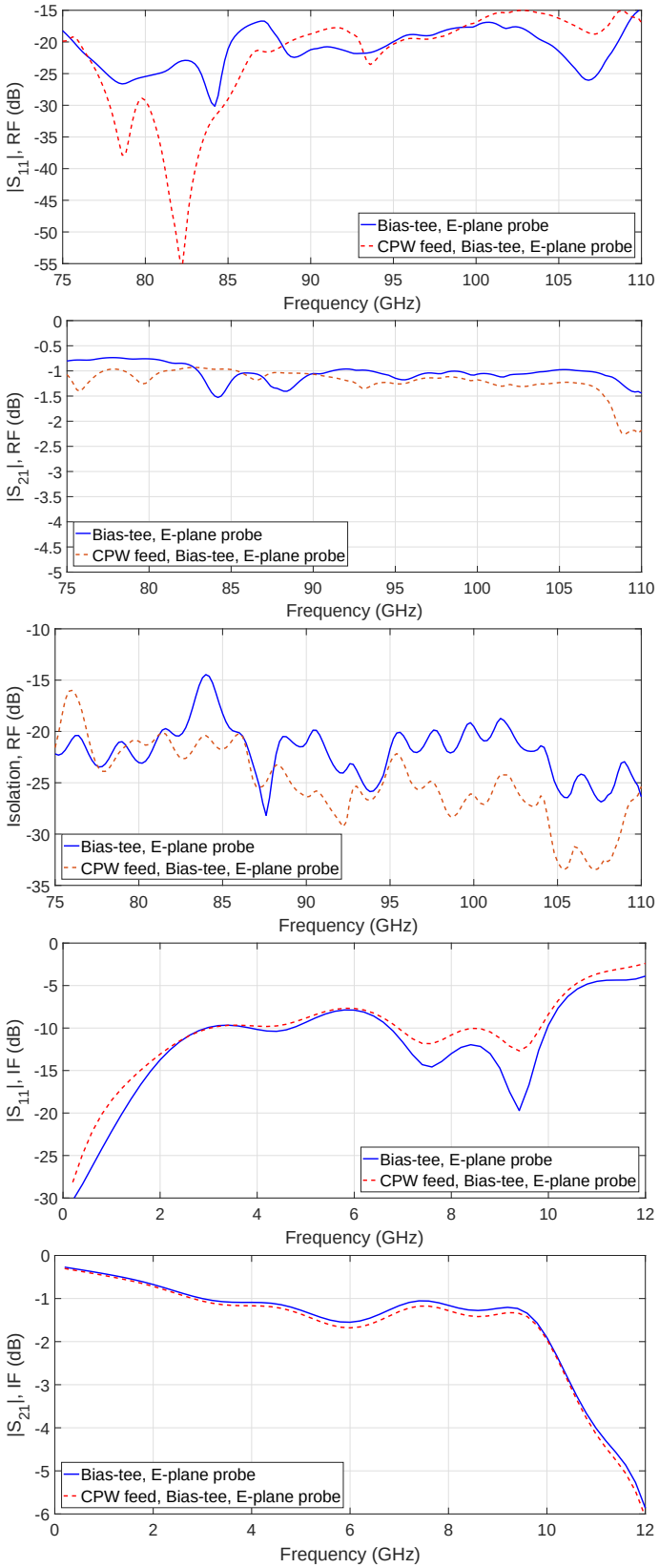

Figure 4.11: Simulation results of the integrated components.

Though the packaging structure shown in Fig. 4.10 contains the principle components in the system diagram, other accessories such as optical fibers, connectors, and metal covers are also necessary parts of the fully packaged photodetector which have to be designed carefully. Fig. 4.12 demonstrates the assembly of the packaged photodetector. During the packaging process, the CPW feed with the photoconductor, bias-tee, and E-plane probe transition are firstly aligned on the bottom metal package which contains half of the WR-10 rectangular waveguide. Silver conductive glue is used for fixing the components, filling the gaps, and providing ground connections. After that the wire bonding bridges as well as chip-level connections are implemented. By adding another metal package on the top which contains the rest half of the WR-10 rectangular waveguide, the RF path is formed. Besides, a SMA connector inserting through the sidewall of the waveguide package is connected to the DC/IF path on the bias-tee. For the optical path, an angled physical contact (APC) connector with an optical fiber is used for guiding the optical signal all the way to the photoconductor. Since the optical signal needs to be illuminated to the photoconductor from the top, by taking into account the efficiency as well as accuracy, a fiber holder with customized dimensions was employed. The fiber holder was fabricated using a polyvinyl chloride (PVC) block by milling process and the optical fiber was fixed inside a though hole drilled from the top. In the last step, the outer metal covers are added which provides both physical and electrical protections.

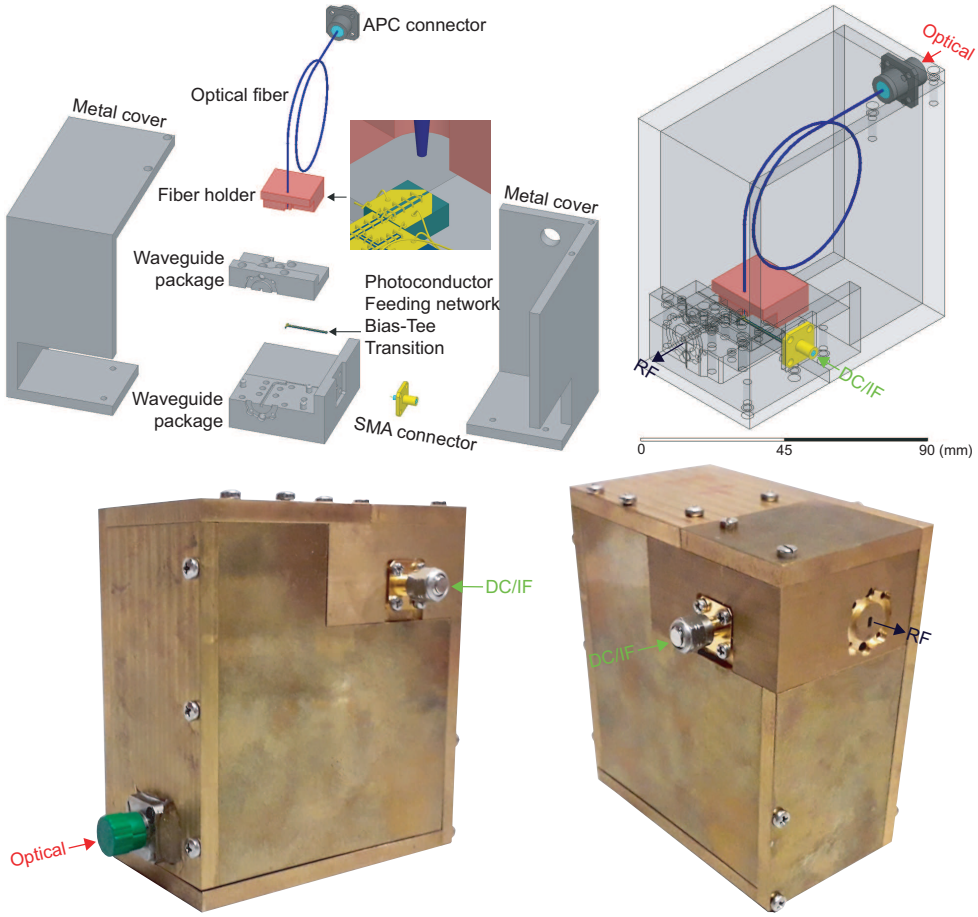

Figure 4.12: Assembly of the packaged photodetector.

4.5 Fabrications, Experimental Setups, and Results

In order to prove the designs and validate the proposed method for system integration, the bias-tee, E-plane probe transition, and waveguide packages illustrated in Fig. 4.9 were fabricated. The fabrications were firstly carried out at TU Darmstadt and then the fabricated components were brought to Danchip (National Center for Micro- and Nanofabrication in Denmark) for system integration and packaging. The bias-tee and the E-plane probe transition were patterned on a high-resistivity Si wafer which is an n-type wafer with a diameter of 2" (50.8 mm) and an orientation of <100>. The main steps for fabricating the bias-tee and the E-plane probe transition are shown in Fig. 4.13 which follows the process of UV photolithography. At the beginning, the layouts of the bias-tee and the E-plane probe transition were rearranged and repeated in an area that fits the size of the wafer. The prepared layouts were printed on a polyester photo mask with a resolution of 6.4e4 DPI (dots per inch). After that, the layouts on the photo mask were transferred to a glass mask which was used for wafer exposure during the photolithography process. A thin layer of photoresist was added on the top of the wafer by using a spin coater. The layouts were transferred to the wafer when the UV light went through the glass mask. Besides, depending on the type of the photoresist, either the layouts or blank area is removed. A conductor layer with a thickness of 400 nm was deposited on the top of the wafer using gold evaporation. Though the conductor layer covers the whole wafer, the gold-plated area with photoresist underneath can be removed when the photoresist is dissolved. Finally, the wafer was diced into samples which were integrated into two identical prototypes.

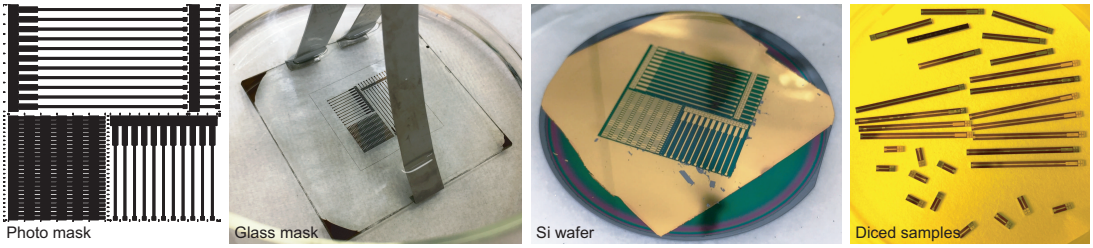

Figure 4.13: Main steps for fabricating the bias-tee and the E-plane probe transition.

Fig. 4.14 shows the integration and packaging of the fabricated bias-tee and E-plane probe transition. The metal package including the rectangular waveguide was divided into two parts and each part was fabricated using a brass block by milling process which was carried out by using a spinner with a radius of 250 μm. For accurate assembly, three guide pins and nine screws were used. For accurate assembly, guide pins as well as screws were used and a standard WR-10 rectangular waveguide flange with annular recess was also applied to the fabricated brass package. The bias-tee and E-plane probe transition were first aligned on the brass carrier and the gaps were filled with silver epoxy. Then the wire bonding bridges along the CPWs, wire bonding connections between the components, and ground connections at different positions were added by ball bonding process. The brass cover was assembled at the last step.

The experimental setup shown in Fig. 4.15 is used for on-wafer measurement at W-band. The measurement system comprises an Anritsu ME7808B vector network analyzer (VNA), two WR-10

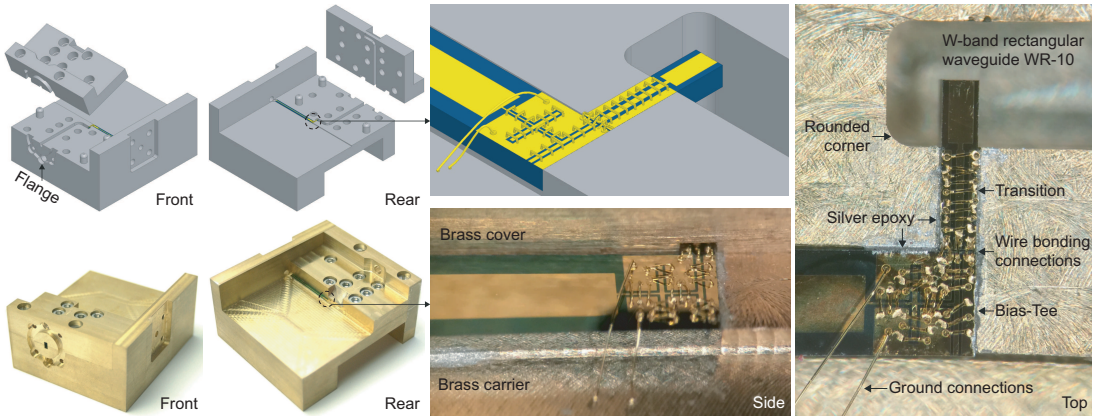

Figure 4.14: Integration and packaging of the fabricated bias-tee and E-plane probe transition.

extenders from Anritsu, and two ground-signal-ground (GSG) probes with 125 μm pitch. Two-port S-parameters of the device under test (DUT) can be measured from 75 GHz to 110 GHz and the on-wafer calibration is executed before each measurement.

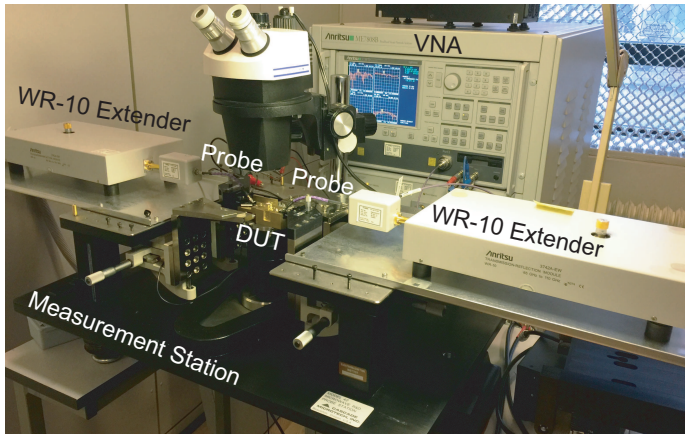

Figure 4.15: Experimental setup for on-wafer measurement at W-band.

As is shown in Fig. 4.16, for easier measurements, two identical samples were fabricated and combined into a back-to-back structure by connecting to each other through the rectangular waveguide flanges. The back-to-back structure was characterized on-wafer by applying the GSG probes to the bias-tee at both sides.

The measurement results (red solid lines) of the packaged bias-tee and E-plane probe transition are shown in Fig. 4.17 in comparison with the simulation results (blue dashed lines). For the back-to-back structure, the measured return loss is better than 10 dB at most of the frequencies from 75 GHz to 110 GHz while it degrades to 8.4 dB in the worst case at 83.3 GHz. The measured insertion loss is less than 7 dB from 75 GHz to 88.7 GHz while it increases to 8 dB at 108.4 GHz and 8.6 dB at 110 GHz. As a result, each fabricated prototype contributes to 4.3 dB insertion loss at the maximum. Besides, there is no visible notch or resonance in the measurement results which means the parasitic modes are successfully restricted. Compared with the simulation results, the

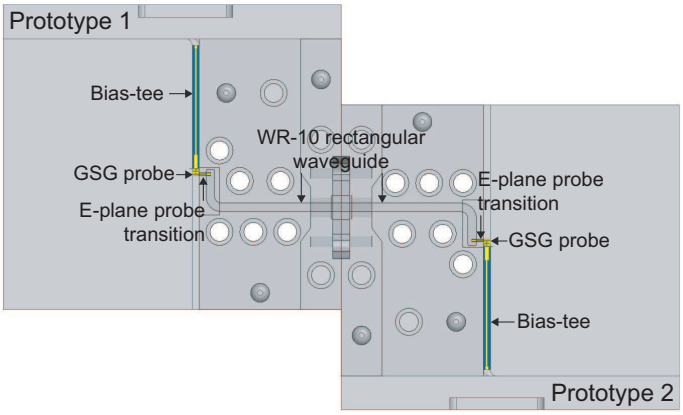

Figure 4.16: DUT in a back-to-back configuration for on-wafer measurement.

difference is around 4 dB for both the return loss and the insertion loss which is mainly caused by the integration process especially the gaps filled with silver conductive glue and the wire bonding connections between the bias-tee and the E-plane probe transition.

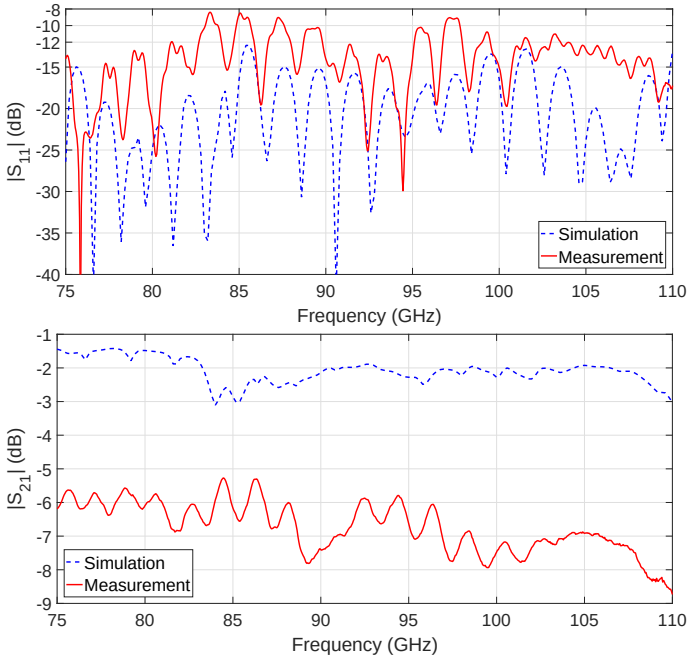

Figure 4.17: Measurement results of the packaged bias-tee and E-plane probe transition.

After the on-wafer measurement, the packaged prototypes were sent back to TU Darmstadt where the CPW feed with the photoconductor was integrated and tested by implementing a THz heterodyne communication system demonstrated in Fig. 4.18. At telecom wavelengths, the photoconductor is challenged by finding suitable photoconductive materials with a short carrier lifetime. Due to the low dark resistance, the DC bias that can be applied to the photoconductor is normally limited which makes it difficult to achieve a sufficient output power. According to [90], by combining erbium arsenide (ErAs), indium gallium arsenide (InGaAs), and indium aluminium

arsenide (InAlAs) layers, the fabricated photoconductor exhibits excellent THz performances with a high dark resistance under continuous wave (CW) operations. As a result, the ErAs:In(Al)GaAs photoconductor is packaged into a THz photodetector which is used as a part of the transmitter in the communication system.

On the Tx side, a CW laser operating at 1550 nm is used as the light source and a polarization controller (PC) is added before the optical signal reaches the MZM where a RF signal at local oscillator frequency (f_{LO}) is modulated to the optical signal achieving two optical tones with the expected distance ($2f_{LO}$) in the spectrum. Then an erbium-doped fiber amplifier (EDFA) is employed to enlarge the power of the optical signal and followed by an arrayed waveguide grating (AWG) which demultiplexes the two optical tones. The data is modulated to one of the tones by using another MZM and a variable optical attenuator (VOA) is applied on the other tone which adjusts the power of the optical signal. After that, the two optical tones are coupled together and the spectrum of the optical signal is also presented. Another EDFA pushes up the power of the optical signal to 30 mW before being transmitted to the photodetector. The RF signal with the modulated data has a frequency component of $2f_{LO}$ which is generated by the photodetector and then guided to the a low noise amplifier (LNA) followed by a medium power amplifier (MPA). The W-band LNA and MPA from Radiometer Physics GmbH can provide gains of 40 dB and 10 dB, respectively. For radiating the RF signal into free space, a W-band standard horn antenna is used which has a gain of 21 dBi.

On the receiver (Rx) side, a comb fiber laser operating at 1550 nm is used as the light source and the repetition rate (f_{comb}) is 40 GHz. The generated optical frequency comb goes through a wavelength selective switch (WSS) which reserves the two optical tones with a distance of 80 GHz ($2f_{comb}$) in the spectrum and the rest of the tones are suppressed. The power of the filtered optical signal is increased to 30 mW by using an EDFA and the spectrum is shown. The photodetector is based on an ErAs:InGaAs photoconductor which is attached to a log-periodic antenna and packaged using a hemispherical silicon lens. Since the DC bias is not required by the photoconductor in this case, the InAlAs layer is excluded, which according to [90] provides a higher mobility and a better sensitivity compared with the photoconductor used on the Tx side. When the IF signal is extracted by the photodetector, it has a frequency component of $|2f_{comb} - 2f_{LO}|$ which can be tuned by sweeping the f_{LO} on the Tx side. Besides, a transimpedance amplifier (TIA) and two electrical amplifiers (EAs) are employed which provide gains of 20 dB, 20 dB, and 17 dB, respectively. Then the power of the IF signal is measured by using a Rohde & Schwarz FSQ40 electrical spectrum analyzer (ESA).

Since the bandwidth of the communication system is limited to 2 GHz due to the TIA on the Rx side, the IF signal is set to operate at 1.3 GHz, 1.4 GHz, and 1.5 GHz which correspond to the transmitted RF signals at 78.7 GHz, 78.6 GHz, and 78.5 GHz, respectively. The measurement results at different operating frequencies are compared in Fig. 4.19. Instead of a single frequency component, the measured IF signal exhibits several tones in the spectrum which might due to a beating interference on the Tx side. In addition, the total powers of the IF signal at different operating frequencies are -2.75 dBm, -2.78 dBm, and -5.43 dBm, respectively, which are calculated by integrating the power over the corresponding frequency ranges read out from the ESA. Though

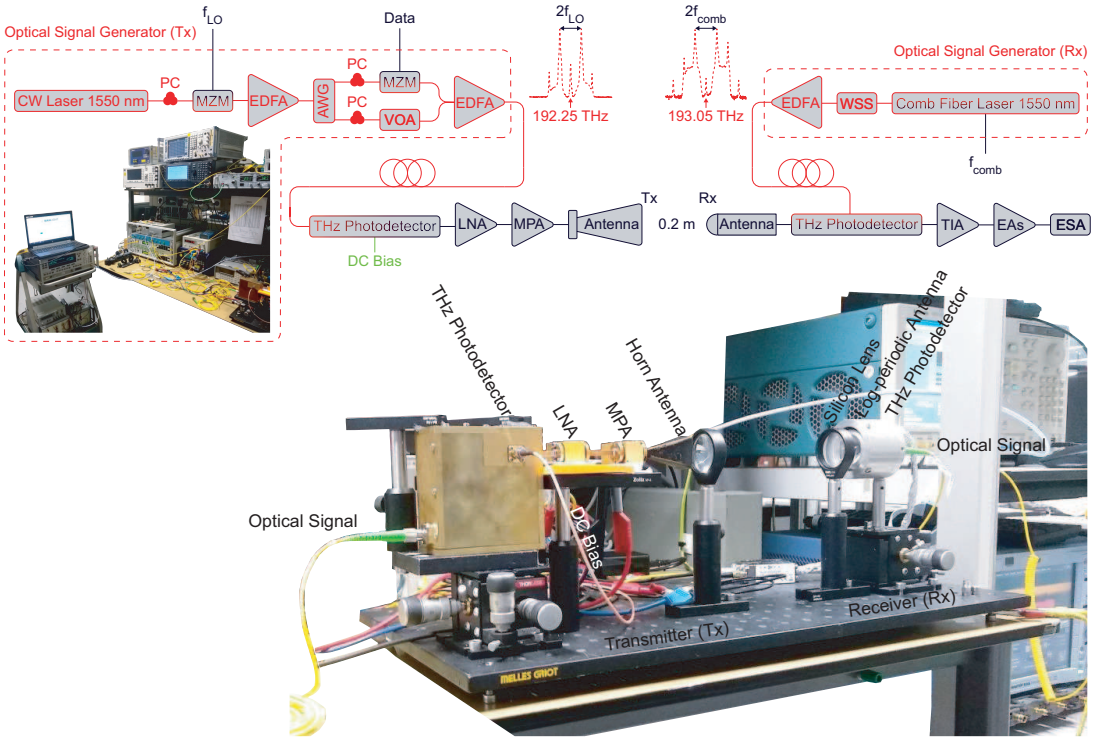

Figure 4.18: Experimental setup of the THz heterodyne communication system.

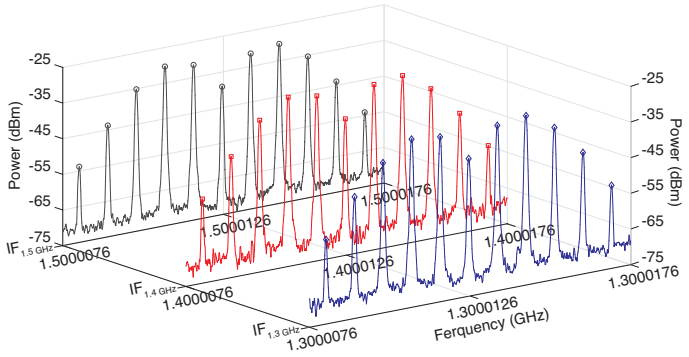

Figure 4.19: Measurement results of the THz heterodyne communication system.

the IF signal spreads slightly in the spectrum, the recovered tones achieve sufficient stability as well as power for supporting data transmissions with different modulation schemes. As a consequence, it validates the proposed system integration and packaging method of the THz photodetector.

4.6 Summary

The system integration and packaging of the THz photodetector at W-band has been presented in this chapter. The structures, designs, simulation methods, and parasitic modes of the principle components involved in the system integration have been introduced at the beginning. The feeding network used for the photoconductor has been described. A 50 Ω CPW based on InP substrate

has been designed as the transmission line for the feeding network which also contains a tapered structure for aligning the photoconductor. In order to restrict parasitic modes, the width of the ground traces has been optimized and wire bonding bridges have been added on the top of the InP substrate. In the simulation, the photoconductor was represented by a lumped port located in the gap between the signal and ground traces. From 75 GHz to 110 GHz, the simulated return loss remains better than 17 dB and the insertion loss is less than 0.5 dB.

After that the proposed bias-tee at W-band has been demonstrated. Due to the rectangular waveguide in the system, the DC block can be omitted from the bias-tee. The bias-tee has been realized by using CPWs based on high-resistivity Si substrate and two open-circuited CPW stubs with a length of quarter wavelength were implemented in parallel for preventing the RF signal from the DC/IF path. The equivalent schematics of the proposed bias-tee and the corresponding Smith charts have been illustrated. According to the simulation results at W-band, the return loss is better than 16.6 dB with an associated insertion loss of 0.9 dB and the isolation is more than 18.6 dB. However, the performances of both transmission and isolation degraded seriously when the wire bonding bridges were removed.

In addition, a rectangular waveguide-to-CPW transition at W-band using E-plane probe has been designed. A 50 Ω CPW based on the same Si substrate and packaged inside a metal cover has been included as a part of the proposed transition at W-band. For connecting to the bias-tee, a tapered structure has been implemented at the beginning of the packaged CPW. A rectangular patch has been inserted into a WR-10 rectangular waveguide and works as the E-plane probe. The rounded corners at the end of the rectangular waveguide were also included in the simulation. The proposed transition at W-band using E-plane probe achieves a simulated return loss of 18.8 dB and a simulated insertion loss of 0.6 dB.

The integration method and packaging structure among the CPW feed, bias-tee, and E-plane probe transition have been figured out. Apart from being used for restricting parasitic modes, wire bondings are also used as chip-level connections between different components and providing ground connections at different positions. The bias-tee has been optimized from the original design. The width of the ground trace on the RF path has been reduced to fit the bias-tee while the feed line on the DC/IF path has been extended by using MSLs in order to reach the SMA connector at the far end. Besides, a quadrant structure has been added to the WR-10 rectangular waveguide which changes the direction of the RF output in 90°. The size and location of the quadrant structure have been optimized for minimizing the reflection. For compensating the thickness difference between the InP and Si substrate, the components have been put on different platforms where the CPW feed locates 70 μm lower than the bias-tee and the E-plane probe transition. The CPW feed, bias-tee, E-plane probe transition, WR-10 rectangular waveguide, and wire bonding connections have been integrated and simulated. From 75 GHz to 110 GHz, the return loss remains better than 15 dB with an associated insertion loss of 2.3 dB and the isolation is more than 16 dB. Based on the designed components and the accessories included in the system integration, the assembly of the packaged photodetector has been addressed. The waveguide package has been divided into two parts and outer metal covers have been added providing both physical and electrical protections.

At the end of this chapter, the fabrication and integration of the proposed bias-tee, E-plane

probe transition, and WR-10 reactangular waveguide have been presented. The fabricated samples were integrated and packaged into two identical prototypes which were combined in a back-to-back configuration. The on-wafer measurement at W-band was carried out by applying the GSG probes to the bias-tee at both sides. The measured return loss is better than 10 dB at most frequencies from 75 GHz to 110 GHz while it degrades to 8.4 dB at 83.3 GHz. The measured insertion loss is less than 7 dB from 75 GHz to 88.7 GHz while it increases to 8.6 dB at 110 GHz. Each fabricated prototype contributes to an insertion loss of 4.3 dB at the maximum. In order to validate the proposed system integration and packaging method, a THz heterodyne communication system has been implemented in which the photodetector is involved on the Tx side as a packaged device which can be used for other communication systems as well. The measured IF signals at different operating frequencies were spread in the spectrum. However, the stability as well as power of the recovered tones are sufficient for supporting data transmissions with different modulation schemes. Though the packaged THz photodetector is based on an ErAs:In(Al)GaAs photoconductor, the proposed system integration and packaging method should also be compatible with other photoconductors as well as photodiodes.

CHAPTER 5

Conclusions

In this thesis work, the strategies for hybrid integration and packaging at millimeter-wave and THz frequencies have been investigated. As a part of the preliminary research, different types of planar transmission lines have been introduced and their properties as well as characteristics have been compared. Coplanar transitions between different planar transmission lines have been designed with the purposes of providing large bandwidths and supporting data transmissions starting from DC. The system integration and packaging of the terabit transmitter as a part of the European project PANTHER has been addressed. In addition, transitions between rectangular waveguides and planar transmission lines have been realized by using different methods. The corresponding system integration and packaging approaches based on the proposed transitions have been demonstrated and their possibilities have been discussed. A Thz photoconductor was integrated with other components and packaged into a photodetector operating at W-band. The packaged photodetector works as an individual device and was implemented on the Tx side of a THz heterodyne communication system.

Being an critical part for the system integration and packaging of PANTHER terabit transmitter, the interposer based on AlN substrate has been designed and optimized for guiding four single-ended signals from the DRVs to the MZM. The proposed transmission lines, CPW-to-CPS transitions, and via connections have been introduced. When designing wideband transmission lines as well as coplanar transitions, except for the mismatches of characteristic impedance and propagation mode, the parasitic effects are the main concern which result in unexpected resonances and higher-order modes. In the research work, two possible ways to restrict it have been addressed. Besides, an equivalent circuit model of via connections can be found in [46]. A CPW-to-CPS transition using wire bonding bridges together with an alumina absorber layer and a CPW-to-ACPS transition using hollow plated vias have been designed, fabricated, and measured. The fabricated CPW-to-CPS transition can provide a bandwidth of 80 GHz [77] while the fabricated CPW-to-ACPS transition achieves a bandwidth of 165 GHz ranging from DC [100]. Both coplanar transitions were based on AlN substrate due to the requirement of the project. However, there is still a potential to achieve larger bandwidths by replacing the substrate material to quartz, reducing the height of the wire bonding bridges, or increasing the diameter of the hollow plated vias.

The 3D hybrid integration scheme of PANTHER terabit transmitter has been demonstrated. As

a supplement, the DRVs, MZM, and via connections involved in the system integration were also introduced. Wire bonding bridges on the top of the interposer together with an absorber layer under the MZM were implemented for restricting parasitic modes. The proposed interposer achieves a simulated bandwidth of 47.5 GHz and the crosstalk effects between different signal traces can be neglected. By including the measurement results of the MZM, the co-simulation of the integrated system was carried out and the results have been presented. The packaging structure of the terabit transmitter has been shown in which the proposed interposer was divided into three pieces for easier fabrication and alignment. Since the architecture of system integration is becoming more compact and complex, it will require more advanced technologies in the future for wideband connections, accurate alignments, restricting parasitic modes, and heat dissipations.

The rectangular waveguide-to-CPW transitions realized by different methods have been presented. Prior to that, a CPW was fabricated on both glass and quartz substrates in order to achieve information of substrate properties at high frequencies. Since the CPW patterned on quartz substrate shows stable performances up to 170 GHz, it was used for fabricating the proposed transitions. As a novel method for realizing rectangular waveguide-to-CPW transitions, a wire bonding was implemented as a probe guiding electromagnetic waves from the rectangular waveguide to the CPW [101]. For the designed transitions, the E-plane probe was replaced by the wire bonding probe while the other components are kept unchanged. The fabricated transition prototype using wire bonding probe achieves a bandwidth of 11 GHz at U-band with an associated insertion loss of 3 dB. For the designed rectangular waveguide-to-CPW transitions at D-band, E-plane probe and wire bonding probe were adjusted to higher operating frequencies by reducing their dimensions [102]. The experimental setup has been introduced and a rectangular waveguide calibration kit has been fabricated. The fabricated transition prototype using E-plane probe can provide a bandwidth of 57.3 GHz at D-band with an associated insertion loss of 1.6 dB. By contrast, the fabricated transition prototype using wire bonding probe achieves a bandwidth of 56.3 GHz at D-band with an associated insertion loss of 2 dB.

In addition, a wideband patch antenna has been designed for direct wireless communications and implemented into a rectangular waveguide-to-CPW transition at D-band [103]. Compared with conventional designs, the proposed patch antenna with rectangular ring structure enlarges the bandwidth without affecting the gain and occupation area. The simulated gain is 7.4 dBi in the direction perpendicular to the patch geometry at 140 GHz with a bandwidth of 50.3 GHz ranging from 115.3 GHz to 165.6 GHz. When the wideband patch antenna is implemented as a transition guiding electromagnetic waves from the rectangular waveguide to the CPW, the measured bandwidth is 42.2 GHz at D-band with an associated insertion loss of 4 dB. Except for being compatible with conventional CPWs, the proposed wideband patch antenna can also be integrated on-chip for example based on a multi-layer InP substrate where the antenna is realized by using elevated CPWs [104].

The system integration and packaging of a photodetector at W-band for THz communications have been addressed [105]. As the principle components involved in the system integration, the feeding network, bias-tee, and E-plane probe transition have been designed. The feeding network is based on InP substrate while the bias-tee and E-plane probe transition are based on high-resistivity

Si substrate. By implementing wire bonding bridges on the top of the substrates, the parasitic modes were restricted. The feeding network consists of a CPW and a tapered structure for aligning the photoconductor. The simulated return loss is better than 17 dB with an associated insertion loss of 0.5 dB. The bias-tee is a three-port components which connects to the feeding network on one side and the E-plane probe transition on the other side. Two open-circuited CPW stubs were implemented in parallel for preventing the RF signal from the DC/IF path. The simulated return loss is better than 16.6 dB with an associated insertion loss of 0.9 dB and the simulated isolation is more than 18.6 dB. The E-plane probe transition consists of a packaged CPW, a rectangular patch, and a WR-10 rectangular waveguide. The simulated return loss is better than 18.8 dB with an associated insertion loss of 0.6 dB. For system integration, silver conductive glue was used for fixing the components, filling the gaps, and providing ground connections. Besides, wire bondings were implemented for restricting parasitic modes, chip-level connections, and providing ground connections. The optical signal was feed to the photodetector by an APC connector and a PVC fiber holder was employed for aligning the optical fiber. The assembly of the packaged photodetector has been demonstrated.

The fabricated bias-tee and E-plane probe transition samples were integrated into two identical prototypes which were combined into a back-to-back structure for the measurement at W-band. The return loss is better than 10 dB at most of the frequencies while it goes to 8.4 dB in the worst case. The insertion loss is less than 7 dB from 75 GHz to 88.7 GHz and it increases to 8.6 dB at 110 GHz which means each fabricated prototype contributes to an insertion loss of 4.3 dB at the maximum. A THz heterodyne communication system was implemented by applying the packaged photodetector on the Tx side. The experiments were carried out by setting the RF signals to operate at 78.5 GHz, 78.6 GHz, and 78.7 GHz, respectively, and measuring the corresponding received power on the Rx side. The stability and power intensity of the recovered tones have proved the possibility of supporting data transmissions with different modulation schemes through the implemented communication system. Thus the proposed system integration and packaging method have been validated. Though an ErAs:In(Al)GaAs photoconductor was used for the photodetector, with the same method, it can be replaced by other photoconductors as well as photodiodes.

Bibliography

[1] G. Carpintero, E. Garcia-Munoz, H. Hartnagel, S. Preu, and A. Raisanen. Semiconductor terahertz technology: devices and systems at room temperature operation. *Wiley*, 2015.

[2] L. Samoska, A. Fung, P. Kangaslahti, R. Gawande, M. Soria, C. Lawrence, T. Gaier, D. Cuadrado-Calle, D. George, G. Fuller, M. Varonen, R. Lai, S. Sarkozy, and K. Cleary. Cryogenic low noise MMIC amplifiers for U-Band (40-60 GHz). In *2016 11th European Microwave Integrated Circuits Conference (EuMIC)*, pages 81–84, Oct 2016.

[3] D. Cuadrado-Calle, D. George, G. A. Fuller, K. Cleary, L. Samoska, P. Kangaslahti, J. W. Kooi, M. Soria, M. Varonen, R. Lai, and X. Mei. Broadband MMIC LNAs for ALMA band 2+3 with noise temperature below 28 K. *IEEE Transactions on Microwave Theory and Techniques*, 65(5):1589–1597, May 2017.

[4] M. Urteaga, Z. Griffith, M. Seo, J. Hacker, and M. J. W. Rodwell. InP HBT technologies for THz integrated circuits. *Proceedings of the IEEE*, 105(6):1051–1067, June 2017.

[5] V. Radisic, D. W. Scott, K. K. Loi, C. Monier, R. Lai, A. Gutierrez-Aitken. Heterogeneously integrated W-Band downconverter. *IEEE Microwave and Wireless Components Letters*, 27(8):739–741, Aug 2017.

[6] V. Radisic, C. Monier, K. K. Loi, and A. Gutierrez-Aitken. W-Band InP HBT power amplifiers. *IEEE Microwave and Wireless Components Letters*, 27(9):824–826, Sept 2017.

[7] S. Giannakopoulos, K. Eriksson, I. Darwazeh, Z. S. He, and H. Zirath. Ultra-broadband common collector-cascode 4-cell distributed amplifier in 250nm InP HBT technology with over 200 GHz bandwidth. In *2017 12th European Microwave Integrated Circuits Conference (EuMIC)*, pages 142–145, Oct 2017.

[8] M. Urteaga, Z. Griffith, R. Pierson, P. Rowell, A. Young, J. Hacker, B. Brar, S. K. Kim, R. Maurer, and M. J. W. Rodwell. THz InP bipolar transistors-circuit integration and applications. In *2017 IEEE Compound Semiconductor Integrated Circuit Symposium (CSICS)*, pages 1–4, Oct 2017.

[9] H. K. Chiou, C. Y. Chang, and H. H. Lin. Balun design for uniplanar broad band double balanced mixer. *Electronics Letters*, 31(24):2113–2114, Nov 1995.

[10] S. Akiyama, H. Itoh, T. Takeuchi, A. Kuramata, and T. Yamamoto. Wide-wavelength-band (30 nm) 10-Gb/s operation of InP-based Mach-Zehnder modulator with constant driving voltage of 2 Vpp. *IEEE Photonics Technology Letters*, 17(7):1408–1410, July 2005.

[11] H. G. Mao and Y. Z. Chueh. Broadband composite right/left-handed coplanar waveguide power splitters with arbitrary phase responses and balun and antenna applications. *IEEE Transactions on Antennas and Propagation*, 54(1):243–250, Jan 2006.

[12] Y. Ding, Y. C. Jiao, P. Fei, B. Li, and Q. T. Zhang. Design of a multiband quasi-Yagi-type antenna with CPW-to-CPS transition. *IEEE Antennas and Wireless Propagation Letters*, 10:1120–1123, Oct 2011.

[13] S. Lin, J. Wang, G. Zhang, and J. Hong. Coplanar stripline-fed compact UWB antenna. *Electronics Letters*, 50(17):1181–1182, Aug 2014.

[14] S. Lin, J. Wang, G. Zhang, and J. Hong. Design of microstrip tri-mode balun bandpass filter with high selectivity. *Electronics Letters*, 51(13):998–999, June 2015.

[15] S. Lange, M. Gruner, C. Meuer, R. Kaiser, M. Hamacher, K. O. Velthaus, and M. Schell. Low switching voltage Mach-Zehnder modulator monolithically integrated with DFB laser for data transmission up to 107.4 Gb/s. *Journal of Lightwave Technology*, 34(2):401–406, Jan 2016.

[16] Y. Ogiso, J. Ozaki, Y. Ueda, N. Kashio, N. Kikuchi, E. Yamada, H. Tanobe, S. Kanazawa, H. Yamazaki, Y. Ohiso, T. Fujii, and M. Kohtoku. Over 67 GHz bandwidth and 1.5 V Vπ InP-based optical IQ modulator with n-i-p-n heterostructure. *Journal of Lightwave Technology*, 35(8):1450–1455, Apr 2017.

[17] T. K. Johansen, J. Vidkjaer, V. Krozer, A. Konczykowska, M. Riet, F. Jorge, and T. Djurhuus. A high conversion-gain Q-Band InP DHBT subharmonic mixer using LO frequency doubler. *IEEE Transactions on Microwave Theory and Techniques*, 56(3):613–619, Mar 2008.

[18] W. R. Deal, X. B. Mei, V. Radisic, K. Leong, S. Sarkozy, B. Gorospe, J. Lee, P. H. Liu, W. Yoshida, J. Zhou, M. Lange, J. Uyeda, and R. Lai. Demonstration of a 0.48 THz amplifier module using InP HEMT transistors. *IEEE Microwave and Wireless Components Letters*, 20(5):289–291, May 2010.

[19] A. H. Gnauck, P. J. Winzer, A. Konczykowska, F. Jorge, J. Y. Dupuy, M. Riet, G. Charlet, B. Zhu, and D. W. Peckham. Generation and transmission of 21.4-Gbaud PDM 64-QAM using a novel high-power DAC driving a single I/Q modulator. *Journal of Lightwave Technology*, 30(4):532–536, Feb 2012.

[20] V. Radisic, K. M. K. H. Leong, X. Mei, S. Sarkozy, W. Yoshida, and W. R. Deal. Power amplification at 0.65 THz using InP HEMTs. *IEEE Transactions on Microwave Theory and Techniques*, 60(3):724–729, Mar 2012.

[21] C. Jiang, V. Krozer, H. G. Bach, G. G. Mekonnen, and T. K. Johansen. Broadband packaging of photodetectors for 100 Gb/s Ethernet applications. *IEEE Transactions on Components, Packaging and Manufacturing Technology*, 3(3):422–429, Mar 2013.

[22] L. Yan and T. K. Johansen. Design of InP DHBT power amplifiers at millimeter-wave frequencies using interstage matched cascode technique. *Microelectronics Journal*, 44(12):1231–1237, Dec 2013.

[23] K. M. K. H. Leong, X. Mei, W. Yoshida, P. H. Liu, Z. Zhou, M. Lange, L. S. Lee, J. G. Padilla, A. Zamora, B. S. Gorospe, K. Nguyen, and W. R. Deal. A 0.85 THz low noise amplifier using InP HEMT transistors. *IEEE Microwave and Wireless Components Letters*, 25(6):397–399, June 2015.

[24] T. Reck, A. Zemora, E. Schlecht, R. Dengler, W. Deal, and G. Chattopadhyay. A 230 GHz MMIC-based sideband separating receiver. *IEEE Transactions on Terahertz Science and Technology*, 6(1):141–147, Jan 2016.

[25] H. Mardoyan, M. A. Mestre, R. Rios-Müller, A. Konczykowska, J. Renaudier, F. Jorge, B. Duval, J. Y. Dupuy, A. Ghazisaeidi, P. Jennevé, M. Achouche, and S. Bigo. Single carrier 168-Gb/s line-rate PAM direct detection transmission using high-speed selector power DAC for optical interconnects. *Journal of Lightwave Technology*, 34(7):1593–1598, Apr 2016.

[26] V. Zhurbenko, T. K. Johansen, M. Squartecchia, V. Midili, O. Rybalko, M. Riet, J. Y. Dupuy, V. Nodjiadjim, and A. Konczykowska. Low conversion loss 94 GHz and 188 GHz doublers in InP DHBT technology. In *2017 Integrated Nonlinear Microwave and Millimetre-wave Circuits Workshop (INMMiC)*, pages 1–3, Apr 2017.

[27] A. Tessmann, A. Leuther, S. Wagner, H. Massler, M. Kuri, H. P. Stulz, M. Zink, M. Riessle, and T. Merkle. A 300 GHz low-noise amplifier S-MMIC for use in next-generation imaging and communication applications. In *2017 IEEE MTT-S International Microwave Symposium (IMS)*, pages 760–763, June 2017.

[28] A. Zamora, K. M. K. H. Leong, G. Mei, M. Lange, W. Yoshida, K. T. Nguyen, B. S. Gorospe, and W. R. Deal. A high efficiency 670 GHz $\times$36 InP HEMT multiplier chain. In *2017 IEEE MTT-S International Microwave Symposium (IMS)*, pages 977–979, June 2017.

[29] R. Weber, H. Massler, and A. Leuther. D-band low-noise amplifier MMIC with 50% bandwidth and 3.0 dB noise figure in 100 nm and 50 nm mHEMT technology. In *2017 IEEE MTT-S International Microwave Symposium (IMS)*, pages 756–759, June 2017.

[30] M. Squartecchia, V. Midili, T. K. Johansen, J. Y. Dupuy, V. Nodjiadjim, M. Riet, and A. Konczykowska. 75 GHz InP DHBT power amplifier based on two-stacked transistors. In *2017 IEEE Asia Pacific Microwave Conference (APMC)*, pages 314–317, Nov 2017.

[31] R. N. Simons. Coplanar waveguide circuits, components, and systems. *John Wiley & Sons*, 2001.

[32] D. E. Anagnostou, M. Morton, J. Papapolymerou, and C. G. Christodoulou. A 0-55-GHz coplanar waveguide to coplanar strip transition. *IEEE Transactions on Microwave Theory and Techniques*, 56(1):1–6, Jan 2008.

[33] P. Wu, Z. Wang, and Y. Zhang. Wideband planar balun using microstrip to CPW and microstrip to CPS transitions. *Electronics Letters*, 46(24):1611–1613, Nov 2010.

[34] Z. Zhou and K. L. Melde. Development of a broadband coplanar waveguide-to-microstrip transition with vias. *IEEE Transactions on Advanced Packaging*, 31(4):861–872, Nov 2008.

[35] R. Valois, D. Baillargeat, S. Verdeyme, M. Lahti, and T. Jaakola. High performances of shielded LTCC vertical transitions from DC up to 50 GHz. *IEEE Transactions on Microwave Theory and Techniques*, 53(6):2026–2032, June 2005.

[36] A. Bhutani, B. Goettel, T. Thelemann, and T. Zwick. CPW-to-SL transition in LTCC technology. *Electronics Letters*, 53(9):609–611, May 2017.

[37] S. Monayakul, S. Sinha, C. T. Wang, N. Weimann, F. J. Schmückle, M. Hrobak, V. Krozer, W. John, L. Weixelbaum, P. Wolter, O. Krüger, and W. Heinrich. Flip-chip interconnects for 250 GHz modules. *IEEE Microwave and Wireless Components Letters*, 25(6):358–360, June 2015.

[38] S. Sinha, R. Doerner, F. J. Schmückle, S. Monayakul, M. Hrobak, N. G. Weimann, V. Krozer, and W. Heinrich. Flip-chip approach for 500 GHz broadband interconnects. *IEEE Transactions on Microwave Theory and Techniques*, 65(4):1215–1225, Apr 2017.

[39] S. Bulja and D. Mirshekar-Syahkal. Novel wideband transition between coplanar waveguide and microstrip line. *IEEE Transactions on Microwave Theory and Techniques*, 58(7):1851–1857, July 2010.

[40] C. C. Tsai, Y. S. Cheng, T. Y. Huang, Y. A. Hsu, and R. B. Wu. Design of microstrip-to-microstrip via transition in multilayered LTCC for frequencies up to 67 GHz. *IEEE Transactions on Components, Packaging and Manufacturing Technology*, 1(4):595–601, Apr 2011.

[41] F. Cai, Y. H. Chang, K. Wang, C. Zhang, B. Wang, and J. Papapolymerou. Low-loss 3-D multilayer transmission lines and interconnects fabricated by additive manufacturing technologies. *IEEE Transactions on Microwave Theory and Techniques*, 64(10):3208–3216, Oct 2016.

[42] T. P. Budka. Wide-bandwidth millimeter-wave bond-wire interconnects. *IEEE Transactions on Microwave Theory and Techniques*, 49(4):715–718, Apr 2001.

[43] S. Beer, B. Ripka, S. Diebold, H. Gulan, C. Rusch, P. Pahl, and T. Zwick. Design and measurement of matched wire bond and flip chip interconnects for D-band system-in-package applications. In *2011 IEEE MTT-S International Microwave Symposium (IMS)*, pages 1–4, June 2011.

[44] S. Beer, H. Gulan, M. Pauli, C. Rusch, G. Kunkel, and T. Zwick. 122-GHz chip-to-antenna wire bond interconnect with high repeatability. In *2012 IEEE/MTT-S International Microwave Symposium Digest*, pages 1–3, June 2012.

[45] S. G. Mao, C. T. Hwang, R. B. Wu, and C. H. Chen. Analysis of coplanar waveguide-to-coplanar stripline transitions. *IEEE Transactions on Microwave Theory and Techniques*, 48(1):23–29, Jan 2000.

[46] Y. Dong, T. K. Johansen, V. Zhurbenko, A. Beretta, A. Vannucci, and G. Locatelli. A 3D hybrid integration methodology for terabit transceivers. In *2015 SBMO/IEEE MTT-S International Microwave and Optoelectronics Conference (IMOC)*, pages 1–5, Nov 2015.

[47] K. Eriksson, P. J. Sobis, S. E. Gunnarsson, J. Hanning, and H. Zirath. InP DHBT amplifier modules operating between 150-300 GHz using membrane technology. *IEEE Transactions on Microwave Theory and Techniques*, 63(2):433–440, Feb 2015.

[48] M. Moallem and K. Sarabandi. 2.5D micromachined 240 GHz cavity-backed coplanar waveguide to rectangular waveguide transition. *IEEE Transactions on Terahertz Science and Technology*, 2(3):315–322, May 2012.

[49] M. Moallem, J. East, and K. Sarabandi. A broadband, micromachined rectangular waveguide to cavity-backed coplanar waveguide transition using impedance-taper technique. *IEEE Transactions on Terahertz Science and Technology*, 4(1):49–55, Jan 2014.

[50] N. Vahabisani and M. Daneshmand. Monolithic wafer-level rectangular waveguide and its transition to coplanar waveguide line using a simplified 3-D fabrication process. *IEEE Transactions on Components, Packaging and Manufacturing Technology*, 4(1):168–176, Jan 2014.

[51] T. Merkle, R. Götzen, J. Y. Choi, and S. Koch. Polymer multichip module process using 3-D printing technologies for D-band applications. *IEEE Transactions on Microwave Theory and Techniques*, 63(2):481–493, Feb 2015.

[52] H. J. Song, H. Matsuzaki, and M. Yaita. Sub-millimeter and terahertz-wave packaging for large chip-width MMICs. *IEEE Microwave and Wireless Components Letters*, 26(6):422–424, June 2016.

[53] T. Tajima, H. J. Song, H. Matsuzaki, and M. Yaita. LTCC-integrated H-plane bends for THz antenna-in-package solution. *IEEE Microwave and Wireless Components Letters*, 27(5):440–442, May 2017.

[54] D. Hou, Y. Z. Xiong, W. L. Goh, S. Hu, W. Hong, and M. Madihian. 130-GHz on-chip meander slot antennas with stacked dielectric resonators in standard CMOS technology. *IEEE Transactions on Antennas and Propagation*, 60(9):4102–4109, Sept 2012.

[55] M. Neshat, D. M. Hailu, M. R. Nezhad-Ahmadi, G. Z. Rafi, and S. Safavi-Naeini. Gain measurement of embedded on-chip antennas in mmW/THz range. *IEEE Transactions on Antennas and Propagation*, 60(5):2544–2549, May 2012.

[56] S. Beer, C. Rusch, B. Göttel, H. Gulan, and T. Zwick. D-band grid-array antenna integrated in the lid of a surface-mountable chip-package. In *2013 7th European Conference on Antennas and Propagation (EuCAP)*, pages 1318–1322, Apr 2013.

[57] Z. J. Hou, Y. Yang, X. Zhu, S. Liao, S. K. Man, and Q. Xue. A 320 GHz on-chip slot antenna array using CBCPW feeding network in 0.13-μm SiGe technology. In *2017 IEEE MTT-S International Microwave Symposium (IMS)*, pages 843–846, June 2017.

[58] Y. Lee, J. P. Becker, J. R. East, and L. P. B. Katehi. Fully micromachined finite-ground coplanar line-to-waveguide transitions for W-band applications. *IEEE Transactions on Microwave Theory and Techniques*, 52(3):1001–1007, Mar 2004.

[59] O. Donadio, K. Elgaid, and R. Appleby. Waveguide-to-microstrip transition at G-band using elevated E-plane probe. *Electronics Letters*, 47(2):115–116, Jan 2011.

[60] L. A. Samoska. An overview of solid-state integrated circuit amplifiers in the submillimeter-wave and THz regime. *IEEE Transactions on Terahertz Science and Technology*, 1(1):9–24, Sept 2011.

[61] E. S. Li, G. X. Tong, and D. C. Niu. Full W-band waveguide-to-microstrip transition with new E-plane probe. *IEEE Microwave and Wireless Components Letters*, 23(1):4–6, Jan 2013.

[62] J. Stenarson, T. N. T. Do, H. Zhao, P. J. Sobis, A. Y. Tang, K. Yhland, and J. Stake. Sensitivity analysis of TRL calibration in waveguide integrated membrane circuits. *IEEE Transactions on Terahertz Science and Technology*, 3(5):558–565, Sept 2013.

[63] V. Hurm, R. Weber, A. Tessmann, H. Massler, A. Leuther, M. Kuri, M. Riessle, H. P. Stulz, M. Zink, M. Schlechtweg, O. Ambacher, and T. Närhi. A 243 GHz LNA module based on mHEMT MMICs with integrated waveguide transitions. *IEEE Microwave and Wireless Components Letters*, 23(9):486–488, Sept 2013.

[64] M. Kärkkäinen, M. Kantanen, S. Caujolle-Bert, M. Varonen, R. Weber, A. Leuther, M. Seelmann-Eggebert, A. Alanne, P. Jukkala, T. Närhi, and K. A. I. Halonen. MHEMT G-band low-noise amplifiers. *IEEE Transactions on Terahertz Science and Technology*, 4(4):459–486, July 2014.

[65] Q. X. Chu, Q. S. Wu, and D. Y. Mo. A Ka-band E-plane waveguide magic-T with coplanar arms. *IEEE Transactions on Microwave Theory and Techniques*, 62(11):2673–2679, Nov 2014.

[66] M. Varonen, L. Samoska, A. Fung, S. Padmanabhan, P. Kangaslahti, R. Lai, S. Sarkozy, M. Soria, H. Owen, T. Reck, G. Chattopadhyay, P. V. Larkoski, and T. Gaier. A WR4 amplifier module chain with an 87 K noise temperature at 228 GHz. *IEEE Microwave and Wireless Components Letters*, 25(1):58–60, Jan 2015.

[67] S. Jameson and E. Socher. A wide-band CMOS to waveguide transition at mm-wave frequencies with wire-bonds. *IEEE Transactions on Microwave Theory and Techniques*, 63(9):2741–2750, Sept 2015.

[68] J. Hanning, V. Drakinskiy, P. Sobis, T. Bryllert, and J. Stake. A broadband THz waveguide-to-suspended stripline loop-probe transition. In *2017 IEEE MTT-S International Microwave Symposium (IMS)*, pages 1091–1094, June 2017.

[69] J. M. Oliver, J. M. Rollin, K. Vanhille, and S. Raman. A W-band micromachined 3-D cavity-backed patch antenna array with integrated diode detector. *IEEE Transactions on Microwave Theory and Techniques*, 60(2):284–292, Feb 2012.

[70] T. Tajima, H. J. Song, and M. Yaita. Design and analysis of LTCC-integrated planar microstrip-to-waveguide transition at 300 GHz. *IEEE Transactions on Microwave Theory and Techniques*, 61(4):106–114, Jan 2016.

[71] B. Zhang and H. Zirath. Metallic 3-D printed rectangular waveguides for millimeter-wave applications. *IEEE Transactions on Components, Packaging and Manufacturing Technology*, 6(5):796–804, May 2016.

[72] X. Shang, P. Penchev, C. Guo, M. J. Lancaster, S. Dimov, Y. Dong, M. Favre, M. Billod, and E. Rijk. W-band waveguide filters fabricated by laser micromachining and 3-D printing. *IEEE Transactions on Microwave Theory and Techniques*, 64(8):2572–2580, Aug 2016.

[73] A. Zapata, M. Düser, J. Spencer, P. Bayvel, I. Miguel, D. Breuer, N. Hanik, and A. Gladisch. Next-generation 100-gigabit metro ethernet (100 GbME) using multiwavelength optical rings. *Journal of Lightwave Technology*, 22(11):2420–2434, Nov 2004.

[74] H. Avramopoulos, V. Katopodis, P. Groumas, L. Gounaridis, A. Konczykowska, Z. Zhang, G. Valicourt, R. Dinu, A. Vannucci, T. K. Johansen, A. Pagano, and C. Kouloumentas. Passive and electro-optic polymer photonics and InP electronics integration for multi-flow terabit transceivers at edge SDN switches and data-center gateways. In *2014 16th International Conference on Transparent Optical Networks (ICTON)*, pages 1–4, July 2014.

[75] W. C. Wu, L. H. Hsu, E. Y. Chang, C. Karnfelt, H. Zirath, J. P. Starski, and Y. C. Wu. 60 GHz broadband MS-to-CPW hot-via flip chip interconnects. *IEEE Microwave and Wireless Components Letters*, 17(11):784–786, Nov 2007.

[76] S. Kim, S. Jeong, Y. T. Lee, D. H. Kim, J. S. Lim, K. S. Seo, and S. Nam. Ultra-wideband (from DC to 110 GHz) CPW to CPS transition. *Electronics Letters*, 38(13):622–623, Jun 2002.

[77] Y. Dong, T. K. Johansen, V. Zhurbenko, and P. J. Hanberg. Coplanar transitions based on aluminum nitride interposer substrate for terabit transceivers. In *2017 47th European Microwave Conference (EuMC)*, pages 620–623, Oct 2017.

[78] D. M. Pozar. Microwave engineering. *John Wiley*, 2012.

[79] F. E. Terman. Radio engineers' handbook. *McGraw-Hill*, 1943.

[80] C. R. Paul. Inductance. loop and partial. *John Wiley & Sons*, 2009.

[81] T. K. Johansen, C. Jiang, D. Hadziabdic, and V. Krozer. EM simulation accuracy enhancement for broadband modeling of on-wafer passive components. In *2007 2nd European Microwave Integrated Circuits Conference (EuMIC)*, pages 447–450, Oct 2007.

[82] A. Konczykowska, F. Jorge, J. Y. Dupuy, M. Riet, V. Nodjiadjim, H. Aubry, and A. Adamiecki. 84 GBd (168 Gbit/s) PAM-4 3.7 Vpp power DAC in InP DHBT for short reach and long haul optical networks. *Electronics Letters*, 51(20):1591–1593, Oct 2015.

[83] T. Umezawa, A. Kanno, K. Kashima, A. Matsumoto, K. Akahane, N. Yamamoto, and T. Kawanishi. Bias-free operational UTC-PD above 110 GHz and its application to high baud rate fixed-fiber communication and W-band photonic wireless communication. *IEEE Journal of Lightwave Technology*, 34(13):3138–3147, July 2016.

[84] L. C. P. Cavalcante, S. Rommel, R. Dinis, L. G. Q. S. Junior, L. F. Q. Silveira, and I. T. Monroy. Performance evaluation of wavelet-coded OFDM on a 4.9 Gb/s W-band radio-over-fiber link. *IEEE Journal of Lightwave Technology*, 35(14):2803–2809, Jan 2017.

[85] A. Bekkali, T. Kobayashi, K. Nishimura, N. Shibagaki, K. Kashima, and Y. Sato. Real-time 10GbE data transmission over a converged RoF links and 96-GHz wireless bridge. *IEEE Photonics Technology Letters*, 29(1):15–18, Jan 2017.

[86] M. Alvaro, R. Puerta, S. Rommel, and I. T. Monroy. 1 Gb/s chaotic encoded W-band wireless transmission for physical layer data confidentiality in radio-over-fiber systems. *Optics Express*, 26(17):22296–22306, Aug 2018.

[87] A. Beling and J. C. Campbell. High-speed photodiodes. *IEEE Journal of Selected Topics in Quantum Electronics*, 20(6):57–63, Nov 2014.

[88] S. Jones, J. Kim, Y. Doi, T. Yamada, N. Koshobu, and H. Togo. Ultra-wideband tunable dual-mode laser for continuous wave terahertz generation. *IEEE Journal of Lightwave Technology*, 32(20):3461–3467, Oct 2014.

[89] S. Preu, M. Mittendorff, H. Lu, H. B. Weber, S. Winnerl, and A. C. Gossard 1550 nm ErAs:In(Al)GaAs large area photoconductive emitters. *Applied Physics Letters*, 101(10):11051–11054, Sept 2012.

[90] A. D. J. Fernandez Olvera, H. Lu, A. C. Gossard, and S. Preu. Continuous-wave 1550 nm operated terahertz system using ErAs:In(Al)GaAs photoconductors with 52 dB dynamic range at 1 THz. *Optics Express*, 25(23):29492–29500, Nov 2017.

[91] U. Nandi, J. C. Norman, A. C. Gossard, H. Lu, and S. Preu. 550-nm driven ErAs:In(Al)GaAs photoconductor-based terahertz time domain system with 6.5 THz bandwidth. *Journal of Infrared Millimeter and Terahertz Waves*, 39(4):340–348, Apr 2018.

[92] H. G. Bach, A. Beling, G. G. Mekonnen, R. Kunkel, D. Schmidt, W. Ebert, A. Seeger, M. Stollberg, and W. Schlaak. InP-based waveguide-integrated photodetector with 100-GHz bandwidth. *IEEE Journal of Selected Topics in Quantum Electronics*, 10(4):668–672, July 2004.

[93] G. G. Mekonnen, B. Hüttl, H. G. Bach, D. Pech, T. Rosin, C. Schubert, A. Konczykowska, F. Jorge, and M. Riet. InP waveguide-integrated pin-photodiode hybrid packaged with an HBT-DEMUX-chip for receiver modules of 80-100 Gb/s data rates. In *2008 34th European Conference on Optical Communication*, pages 1–2, Sept 2008.

[94] C. Jiang, V. Krozer, H. G. Bach, G. G. Mekonnen, and T. K. Johansen. Packaging of photodetector modules for 100 Gbit/s applications using electromagnetic simulations. In *2009 39th European Microwave Conference (EuMC)*, pages 1369–1372, Sept 2009.

[95] H. G. Bach, R. Kunkel, G. G. Mekonnen, R. Zhang, A. Sigmund, D. Schmidt, C. Sakkas, D. Pech, and C. Schubert. Novel 107 Gb/s bias-feeding photodetector OEIC for efficient low-cost photoreceiver co-packaging. In *2009 35th European Conference on Optical Communication*, pages 1–2, Sept 2009.

[96] A. Stöhr, S. Babiel, P. J. Cannard, B. Charbonnier, F. Dijk, S. Fedderwitz, D. Moodie, L. Pavlovic, L. Ponnampalam, C. C. Renaud, D. Rogers, V. Rymanov, A. Seeds, A. G. Steffan, A. Umbach, and M. Weiß. Millimeter-wave photonic components for broadband wireless systems. *IEEE Transactions on Microwave Theory and Techniques*, 58(11):3071–3082, Nov 2010.

[97] M. Jarrahi. Advanced photoconductive terahertz optoelectronics based on nano-antennas and nano-plasmonic light concentrators. *IEEE Transactions on Terahertz Science and Technology*, 5(3):391–397, May 2014.

[98] I. Flammia, T. Kleinfeld, M. Frei, A. U. Rivera, and A. Stöhr. 71-76 GHz grounded-coplanar-waveguide-to-rectangular-waveguide transition with integrated planar bias tee for quasi-hermetic radio-over-fiber wireless transmitter. In *2012 7th European Microwave Integrated Circuits Conference (EuMIC)*, pages 512–515, Oct 2012.

[99] B. Khani, V. Rymanov, I. Flammia, and A. Stöhr. Planar 71-76 GHz laminate integration platform for connecting millimeter wave photodiodes to WR-12 waveguides. In *2015 17th International Conference on Transparent Optical Networks (ICTON)*, pages 1–4, July 2015.

[100] Y. Dong, T. K. Johansen, and V. Zhurbenko. Ultra-wideband coplanar waveguide to asymmetric coplanar stripline transition from DC to 165 GHz. *International Journal of Microwave and Wireless Technologies*, 10(8):870–876, June 2018.

[101] Y. Dong, T. K. Johansen, V. Zhurbenko, and P. J. Hanberg. Rectangular waveguide-to-coplanar waveguide transitions at U-band using E-plane probe and wire bonding. In *2016 46th European Microwave Conference (EuMC)*, pages 5–8, Oct 2016.

[102] Y. Dong, V. Zhurbenko, P. J. Hanberg, and T. K. Johansen. A D-band rectangular waveguide-to-coplanar waveguide transition using wire bonding probe. *Journal of Infrared, Millimeter, and Terahertz Waves*, pages 1–17, Nov 2018.

[103] Y. Dong, T. K. Johansen, V. Zhurbenko, and P. J. Hanberg. A rectangular waveguide-to-coplanar waveguide transition at D-band using wideband patch antenna. In *2018 48th European Microwave Conference (EuMC)*, pages 1–4, Sept 2018.

[104] Y. Dong, T. K. Johansen, and V. Zhurbenko. On-chip patch antenna on InP substrate for short-range wireless communication at 140 GHz. In *2017 SBMO/IEEE MTT-S International Microwave and Optoelectronics Conference (IMOC)*, pages 1–5, Aug 2017.

[105] Y. Dong, A. F. Olvera, A. Morales, M. M. Aller, S. Preu, V. Zhurbenko, P. J. Hanberg, C. Okonkwo, I. T. Monroy, and T. K. Johansen. System integration and packaging of a terahertz photodetector at W-band. Submitted to *IEEE Transactions on Components, Packaging and Manufacturing Technology*.

Appendices

APPENDIX A

Planar Transmission Lines and Coplanar Transitions for Differential Signal Pair

A.1 Coupled Coplanar Waveguide

When two complementary signals need to be transmitted 180 ° out of phase, coupled coplanar waveguide (CCPW) can be used as the planar transmission line where the information is carried by the difference between the two signals and the common-mode interference during the transmission is canceled which normally results in a large bandwidth and becomes a competitive candidate for high-speed data transmissions.

As is shown in Fig. A.1, a CCPW is designed on an aluminum nitride (AlN) substrate with a ground plane on the bottom. The CCPW has a ground-signal-ground-signal-ground (GSGSG) structure which can be used for supporting two single-ended signals in parallel or a differential signal pair. The dimensions of the signal and ground traces are the same as those shown in Fig. 2.2 which are used for designing the coplanar waveguide (CPW). The thickness of the AlN substrate is 127 μm and its width increases to 2 mm since more traces need to be placed on the top. In the simulation, an air cavity with radiation boundary conditions is added around the substrate in order to prevent the reflections caused by the surroundings. Besides, lumped ports with vertical perfect electric conductor (PEC) bridges are used as the excitation scheme and the differential signal pair is assigned to the input and output ports. The parasitic sheet inductance is also calibrated out from the simulation results by post processing.

Fig. A.2 shows the simulated S-parameters of the CCPW based on AlN substrate when it is driven by a differential signal pair. The blue solid lines represent the simulation results of the CCPW with a length of 1.2 mm while the red solid lines are the simulation results when the length increases to 5 mm. Due to the thin AlN substrate and the bottom ground plane, in both cases, the notches appear on the S-parameters due to the parasitic modes on the CCPW which limits the bandwidth and degrades its performances. For the CCPW with a length of 5 mm, the notches appear periodically from lower frequencies and the first notch pops up at 10.5 GHz. Under this

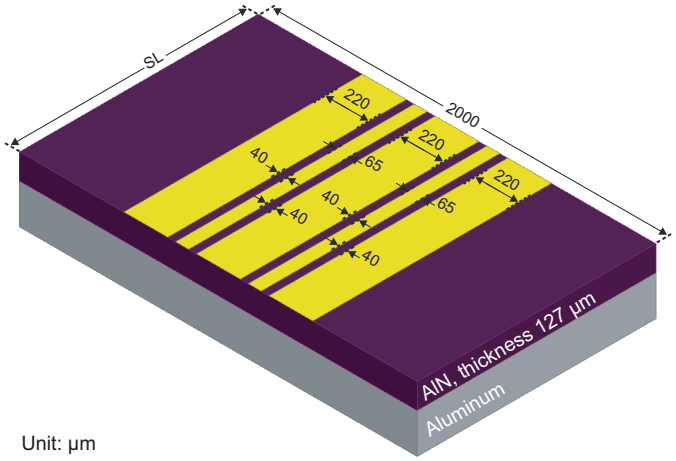

Figure A.1: CCPW based on AlN substrate with a bottom ground plane.

circumstance, it becomes necessary to restrict parasitic modes when the bottom ground plane of the CCPW cannot be avoided.

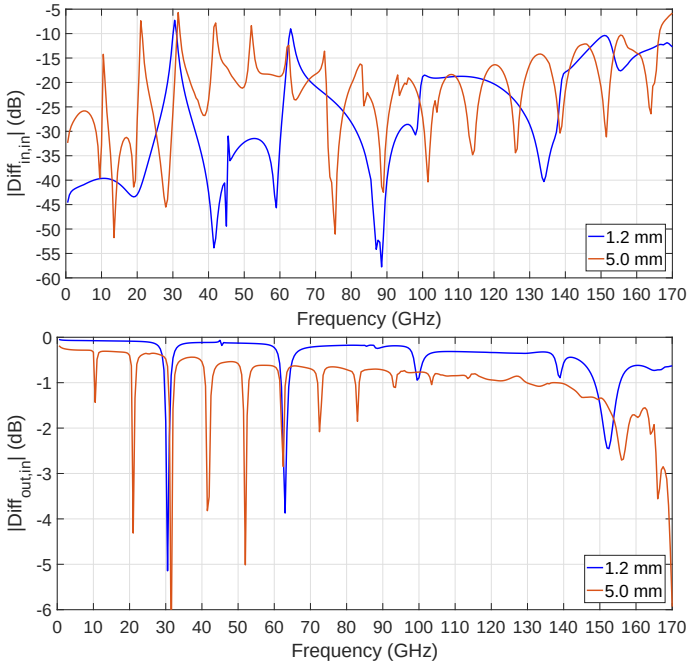

Figure A.2: Simulation results of the CCPW based on AlN substrate with different SL values.

According to the preliminary research of the CPW in Section 2.1.1, a polyoxymethylene (POM) absorber layer together with wire bonding bridges are implemented to restrict the parasitic modes on the CCPW. Fig. A.3 demonstrates the structures of the CCPW based on different methods. The CCPW with an absorber layer or wire bonding bridges solely are shown as the references. In the designs, the POM absorber layer with a thickness of 3.5 mm is used for increasing the distance between the bottom ground plane and the CCPW on the top while it can be replaced by other materials as well. The wire bonding bridges are added all the way along the CCPW so that the

electrical fields are more likely to be concentrated between the signal traces and the wire bonding bridges instead of the bottom ground plane. The terminals of each wire bonding bridge are located as close to the edge of the ground trace as possible which makes it realistic for the central ground trace to have two horizontal wire bonding bridges at the same time.

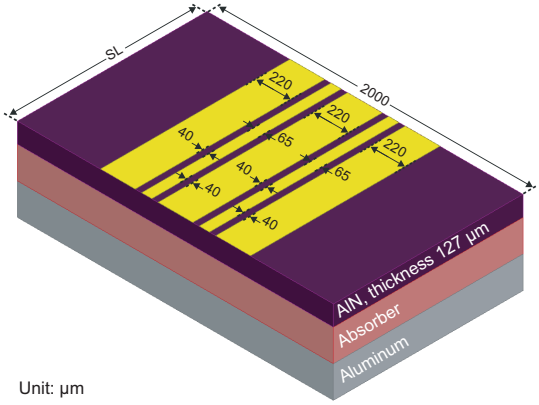

(a) CCPW with an absorber layer.

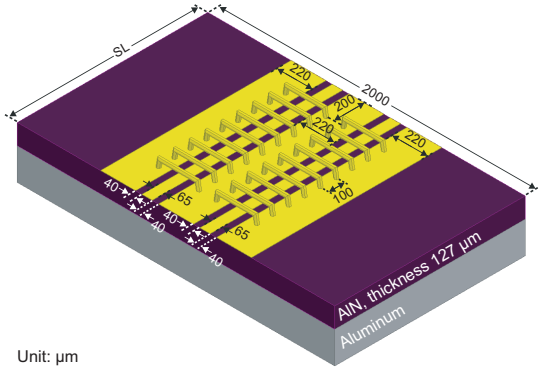

(b) CCPW with wire bonding bridges.

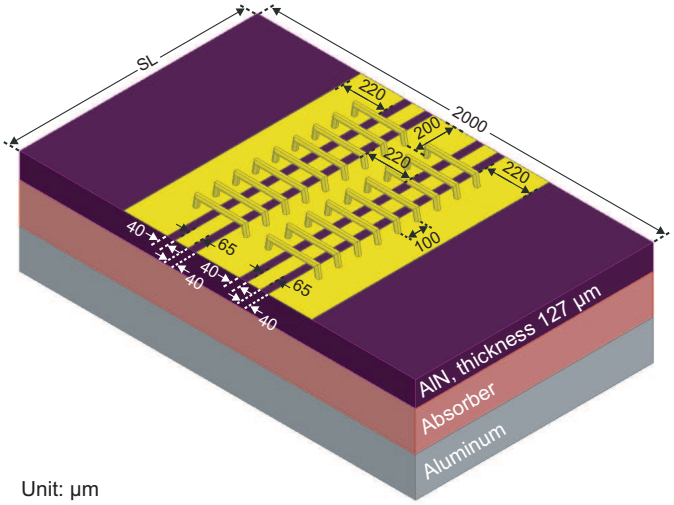

(c) CCPW with an absorber layer and wire bonding bridges.

Figure A.3: CCPW based on AlN substrate with different methods for restricting parasitic modes.

The simulated S-parameters of the CCPW based on different methods for restricting parasitic modes are shown in Fig. A.4. The CCPW has a length of 5 mm and is driven by a differential signal pair. The red dashed lines are the simulation results of the CCPW using wire bonding bridges. Compared with the simulation results in Fig. A.2 when there is no wire bonding bridge and the length is 5 mm, the parasitic modes are restricted to some extend but not sufficient. It shows an improvement by adding wire bonding bridges where the first notch appears at 44 GHz instead of 10.5 GHz. The blue dashed lines and green solid lines are the simulation results when the POM absorber layer is added underneath. In both cases, the CCPW shows a smooth transmission up to 170 GHz where the insertion loss is less than 1.5 dB and the return loss is better than 17.5 dB. However, when the POM absorber layer and wire bonding bridges are used simultaneously, a more

uniform matching among the whole frequency range is achieved.

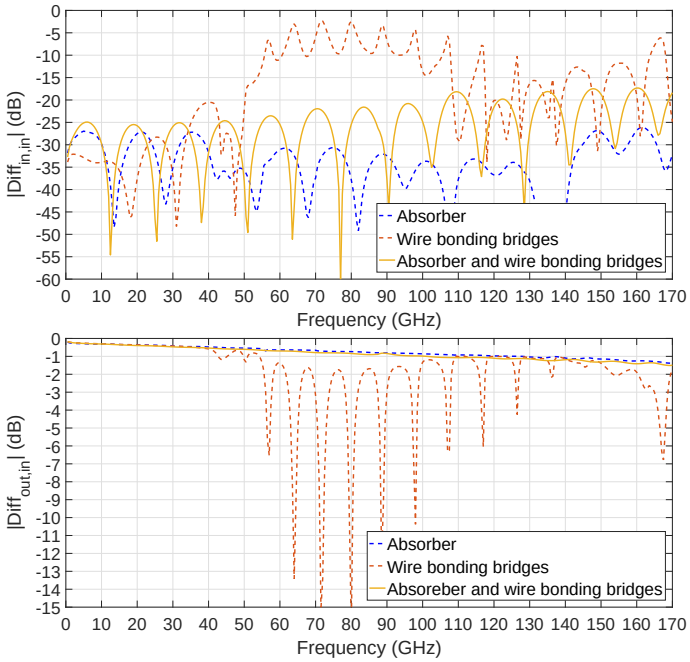

Figure A.4: Simulation results of the CCPW with a length of 5 mm based on different methods for restricting parasitic modes.

As is shown in Fig. A.5, apart from using an absorber layer together with wire bonding bridges, hollow plated vias going through the AlN substrate are added along the ground traces on the CCPW in order to restrict the parasitic modes. The dimensions of the vias, traces, and gaps are the same as those used for designing the CPW which have been illustrated in Fig. 2.14. Besides, another gold conductor layer is added on the backside of the AlN substrate in order to support the fabrication of the hollow plated vias.

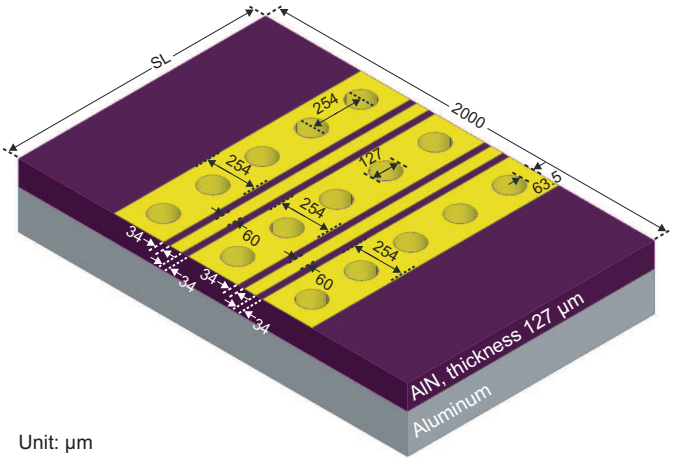

Figure A.5: CCPW with hollow plated vias.

The simulation results of the CCPW with hollow plated vias are shown by the red solid lines

in Fig. A.6. The CCPW has a length of 5.08 mm and it is driven by a differential signal pair. In the whole frequency range, the simulated insertion loss is less than 2.1 dB and the return loss is better than 10 dB. In comparison, a better transmission performance is achieved by the CCPW with hollow plated vias from DC to 139 GHz while the CCPW with the POM absorber layer and wire bonding bridges exhibits a better uniformity from 139 GHz to 170 GHz.

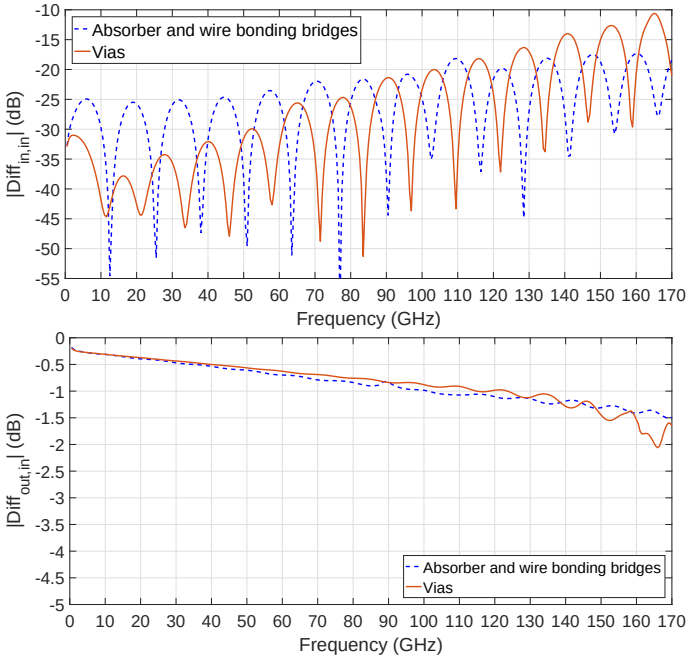

Figure A.6: Simulation results of the CCPW with hollow plated vias (red solid lines) and the CCPW with an absorber layer and wire bonding bridges (blue dashed lines).

A.2 Coupled Line

Coupled line is a type of planar transmission line that has two identical signal traces on the top of the substrate forming a signal-signal (SS) structure. As is shown in Fig. A.7, the width of the signal traces is 65 μm and they are separated by a 80 μm gap in the middle. The coupled line is designed on the same AlN substrate whose thickness is 127 μm and there is a bottom ground plane. Though both coupled line and CCPW can support a differential signal pair, the lacking of ground trace makes the coupled line not applicable for supporting single-ended signals. For the CCPW shown in Fig. A.1, the information is transmitted by two complementary signals guided through two independent signal traces while for the coupled line, the two complementary signals are coupled directly with each other so that the interference during the transmission as well as the parasitic modes are restricted due to the intrinsic property of the coupled line. In addition, the port excitation scheme for simulating coupled lines in ANSYS are also shown in Fig. A.7. The port field indicates that the coupling exists not only in the gap between the signal traces but also between the signal traces and the bottom ground plane.

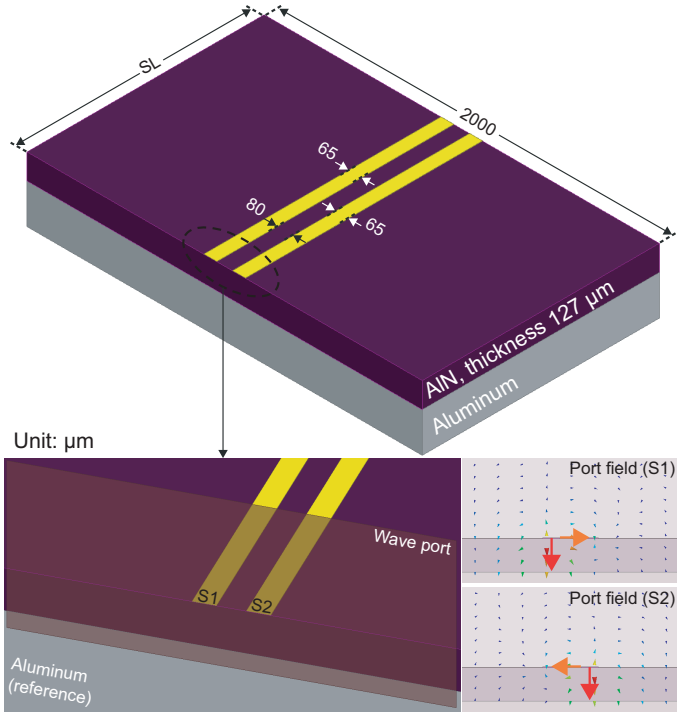

Figure A.7: Coupled line based on AlN substrate with a bottom ground plane and the port excitation scheme used for simulations.

For simulating the designed coupled line, wave ports are used as the excitation scheme and an air cavity with radiation boundary conditions is added on the top of the substrate for accuracy improvement. Wave ports are assigned to the sheets located on the edge of the simulation space. Besides, the bottom ground plane is touched by the edges of the wave ports which is selected to be the reference. Since there is no ground trace on the top, the wave port should be large enough so that the electric fields would not couple to the edges of the wave ports accidentally. Differential signal pair is assigned to the input and output ports with an even and odd mode characteristic impedances of 100 Ω and 25 Ω, respectively. Fig. A.8 shows the coupled line with an absorber layer underneath for restricting parasitic modes which is also the only applicable method since the wire bonding bridges and hollow plated vias cannot be implemented. The absorber layer has a thickness of 3.5 mm and POM is used as the material.

The blue solid lines in Fig. A.9 are the simulated S-parameters of the coupled line with a bottom ground plane while the red solid lines are the simulation results when the POM absorber layer is added underneath. In both cases, the coupled line has a length of 5 mm and it is driven by a differential signal pair. In the whole frequency range, the insertion loss is less than 1.1 dB and the return loss is better than 20.5 dB whether the POM absorber layer is added or not. This is due to the intrinsic property of the couple line where the two complementary signals are coupled directly with each other. In Table. A.1, the performances of the couple line are compared with other planar transmission lines based on the same AlN substrate with a length of 5 mm.

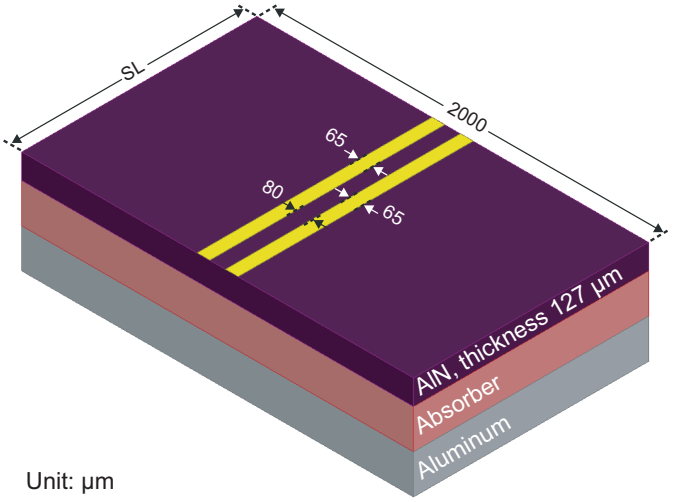

Figure A.8: Coupled line with an absorber layer.

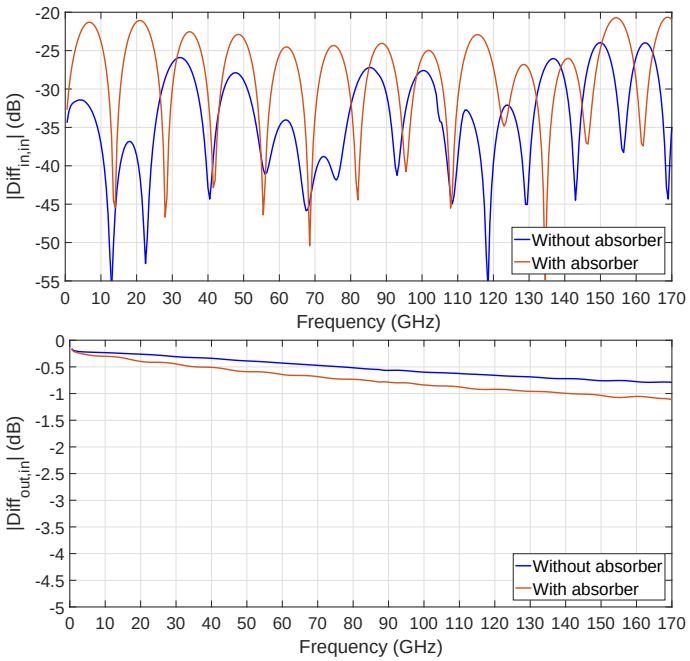

Figure A.9: Simulation results of the coupled line with (red solid lines) and without (blue solid lines) the POM absorber layer.

Table A.1: Planar transmission lines based on AlN substrate with a length of 5 mm

Signal type	Transmission line	Configuration	Method	Insertion loss	Return loss	Bandwidth*
Single-ended	CPW	GSG	POM absorber layer and wire bonding bridges	1.55 dB	16.3 dB	170 GHz
Single-ended	CPW	GSG	Hollow plated vias	3 dB	16.5 dB	166.5 GHz
Single-ended	CPS	GS	Absorber layer	3 dB	14.3 dB	50 GHz
Single-ended	CPS	GS	Hollow plated vias	1 dB	16.3 dB	170 GHz
Differential	CCPW	GSGSG	POM absorber layer and wire bonding bridges	1.5 dB	17.5 dB	170 GHz
Differential	CCPW	GSGSG	Hollow plated vias	2.1 dB	10 dB	170 GHz
Differential	Coupled line	SS	Absorber layer	1.1 dB	20.5 dB	170 GHz

*The bandwidth is defined as the frequency band where the insertion loss is less than 3 dB and the return loss is better than 10 dB.

A.3 Coupled Coplanar Waveguide-to-Coupled Line Transitions

By using the CCPW and coupled line introduced in Section A.1 and Section A.2, respectively, two CCPW-to-coupled line transitions using either wire bonding bridges together with an absorber layer or hollow plated vias going through the substrate are designed for supporting a differential signal pair.

Fig. A.10 shows the proposed CCPW-to-coupled line transition in a back-to-back configuration using wire bonding bridges together with an absorber layer. The AlN substrate is 3000 μm in length and 2000 μm in width with a thickness of 127 μm. The back-to-back structure consists of two CCPWs with a length of 775 μm, a coupled line in the middle with a length of 500 μm, and two transitions with a length of 475 μm. The details of the proposed transition structure are also demonstrated in Fig. A.10. At the beginning of the transition, the central ground trace of the CCPW terminates smoothly forming a semicircle which has a diameter of 220 μm and the two signal traces move towards each other forming a ground-signal-signal-ground (GSSG) structure. At the end of the GSSG structure, the two ground traces on the sides are faded out gradually and it becomes a SS structure which is also the starting point of the coupled line. All the turns as well as corners are rounded to overcome the mismatch effects caused by the structural discontinuities. In order to restrict parasitic modes, the POM absorber layer with a thickness of 3.5 mm is added under the AlN substrate and the wire bonding bridges are implemented all the way along the transition. The diameter of the wire bonding bridges is 25 μm and the height is 50 μm.

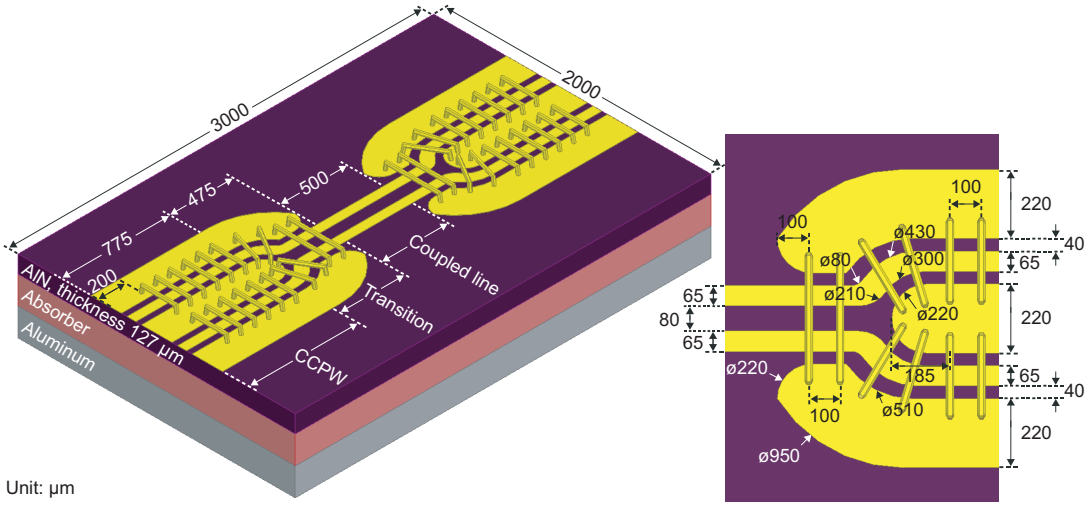

Figure A.10: CCPW-to-coupled line transition in a back-to-back configuration using wire bonding bridges together with an absorber layer.

Fig. A.11 shows the simulated S-parameters of the CCPW-to-coupled line transitions in a back-to-back configuration when it is driven by a differential signal pair. The red solid lines are the simulation results of the proposed transition when wire bonding bridges are implemented which exhibits a bandwidth of 117 GHz ranging from DC. The return loss is better than 10 dB and the insertion loss is less than 3 dB. Compared with the blue dashed lines which represent the simulation results when there is no wire bonding bridge, the parasitic modes are successfully restricted and an

improvement of 101.5 GHz is achieved for the bandwidth.

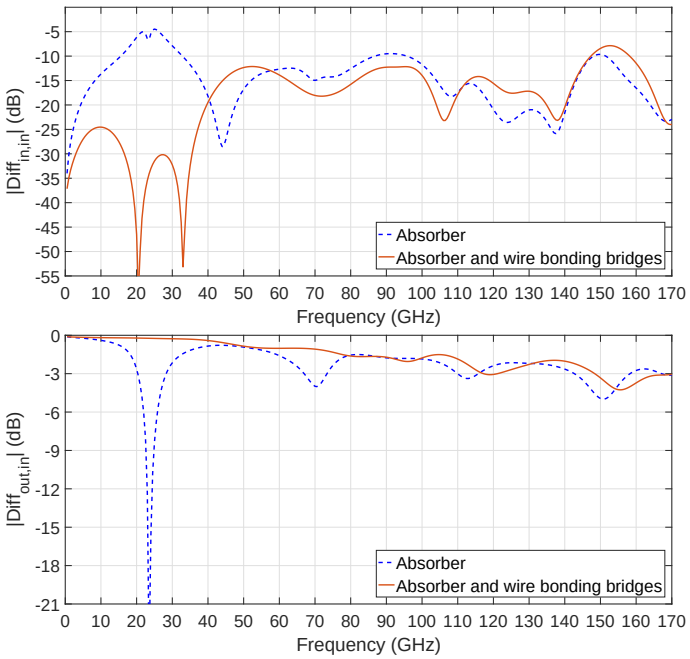

Figure A.11: Simulation results of the CCPW-to-coupled line transition using an absorber layer solely (blue dashed lines) and the CCPW-to-coupled line transition using wire bonding bridges together with an absorber layer (red solid lines).

The proposed CCPW-to-coupled line transition in a back-to-back configuration using hollow plated vias is shown in Fig. A.12. The dimensions of the CCPW are optimized due to the vias going through the AlN substrate while the coupled line are the same as before. The width of the ground traces increases to 254 μm and another conductor layer is added on the backside of the AlN substrate in order to support the fabrication of the hollow plated vias. Besides, the widths of the signal traces and the gaps are optimized to 60 μm and 34 μm, respectively. The length of the AlN substrate increases to 3060 μm. The back-to-back structure consists of two CCPWs with a length of 771 μm, a coupled line in the middle with a length of 500 μm, and two transitions with a length of 509 μm. Fig. A.12 also shows the details of the proposed transition structure. At the beginning of the transition, the center ground trace of the CCPW is terminated and the two signal traces move towards each other forming a GSSG structure. Due to the vias on the central ground trace, the termination follows the shape of a semicircle with a diameter of 254 μm. In addition, the two ground traces on the sides together with the vias also turn towards each other so that the width of the gaps between the signal and ground traces are kept. At the end of the GSSG structure, the two ground traces on the sides are faded out gradually and it becomes a SS structure which is applicable for connecting to the coupled line in the middle. The corners and turns in the transition structure are rounded in order to overcome the mismatch effects caused by the structural discontinuities.

The simulation results of the CCPW-to-coupled line transitions in a back-to-back configuration when it is driven by a differential signal pair are shown in Fig. A.13. The red solid lines are the simulation results of the proposed transition using hollow plated vias which exhibits a bandwidth

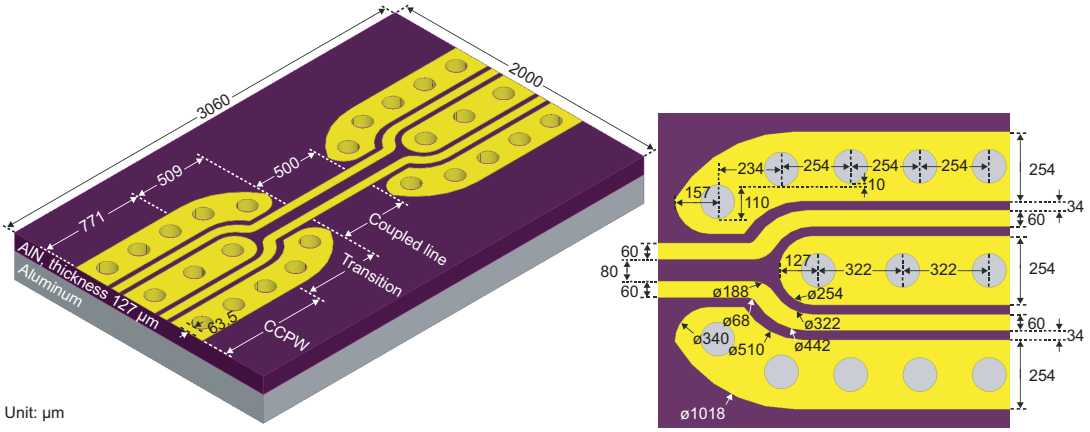

Figure A.12: CCPW-to-coupled line transition in a back-to-back configuration using hollow plated vias.

of 136 GHz. In comparison with the blue dashed lines which represent the simulation results of the proposed transition using wire bonding bridges together with an absorber layer, a better transmission performance is achieved when hollow plated vias are used for restricting parasitic modes and the bandwidth increases 19 GHz.

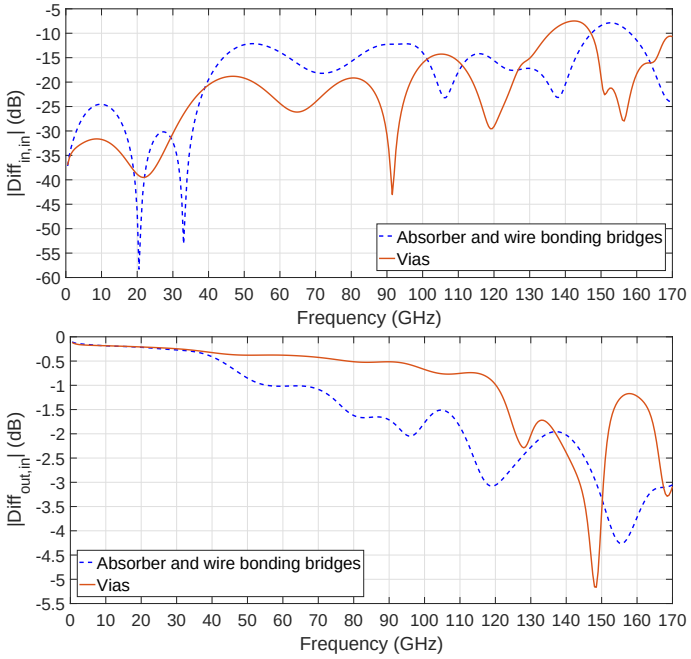

Figure A.13: Simulation results of the CCPW-to-coupled line transition using hollow plated vias (red solid lines) and the CCPW-to-coupled line transition using wire bonding bridges together with an absorber layer (blue dashed lines).

APPENDIX **B**

List of Acronyms

3D:	three-dimensional
ACPS:	asymmetric coplanar stripline
ADS:	advanced design system
AlN:	aluminum nitride
Al_2O_3:	aluminum oxide
APC:	angled physical contact
AWG:	arrayed waveguide grating
CB-CPW:	conductor-backed coplanar waveguide
CCPW:	coupled coplanar waveguide
CNC:	computer numerical control
CPS:	coplanar stripline
CPW:	coplanar waveguide
CW:	continuous wave
DC:	direct current
DHBT:	double heterojunction bipolar transistor
DP:	dual-polarization
DPI:	dots per inch
DP-QPSK:	dual-polarization quadrature phase-shift keying
DRV:	driver
DUT:	device under test
EA:	electrical amplifier
ECPW:	elevated coplanar waveguide
EDFA:	erbium-doped fiber amplifier
EM:	electromagnetic
EO:	electro-optic

ErAs: erbium arsenide
ESA: electrical spectrum analyzer

GaAs: gallium arsenide
GS: ground-signal
GSG: ground-signal-ground
GSGSG: ground-signal-ground-signal-ground
GSSG: ground-signal-signal-ground

HEMT: high electron mobility transistor
HFSS: high frequency structural simulator

IF: intermediate frequency
InAlAs: indium aluminium arsenide
InGaAs: indium gallium arsenide
InP: indium phosphide

LBM: laser beam machining
LNA: low noise amplifier
LTCC: low-temperature co-fired ceramic

MIC: microwave integrated circuit
MPA: medium power amplifier
MSL: microstrip line
MMIC: monolithic microwave integrated circuit
MZM: Mach-Zehnder modulator

PC: polarization controller
PEC: perfect electric conductor
POM: polyoxymethylene
PVC: polyvinyl chloride

QAM: quadrature amplitude modulation

RF: radio frequency
Rx: receiver

SDN: software-defined networking
Si: silicon
SiO_2: silicon dioxide
SLA: stereolithography

SOP: system-on-package
SS: signal-signal

THz: terahertz
TRL: through-reflect-line
Tx: transmitter

UV: ultraviolet

VNA: vector network analyzer
VOA: variable optical attenuator